U.S. Department
of Transportation
Federal Railroad
Administration

Office of Research,
Development and Technology
Washington, DC 20590

Advanced Modeling of Wheel-Rail Friction Phenomena

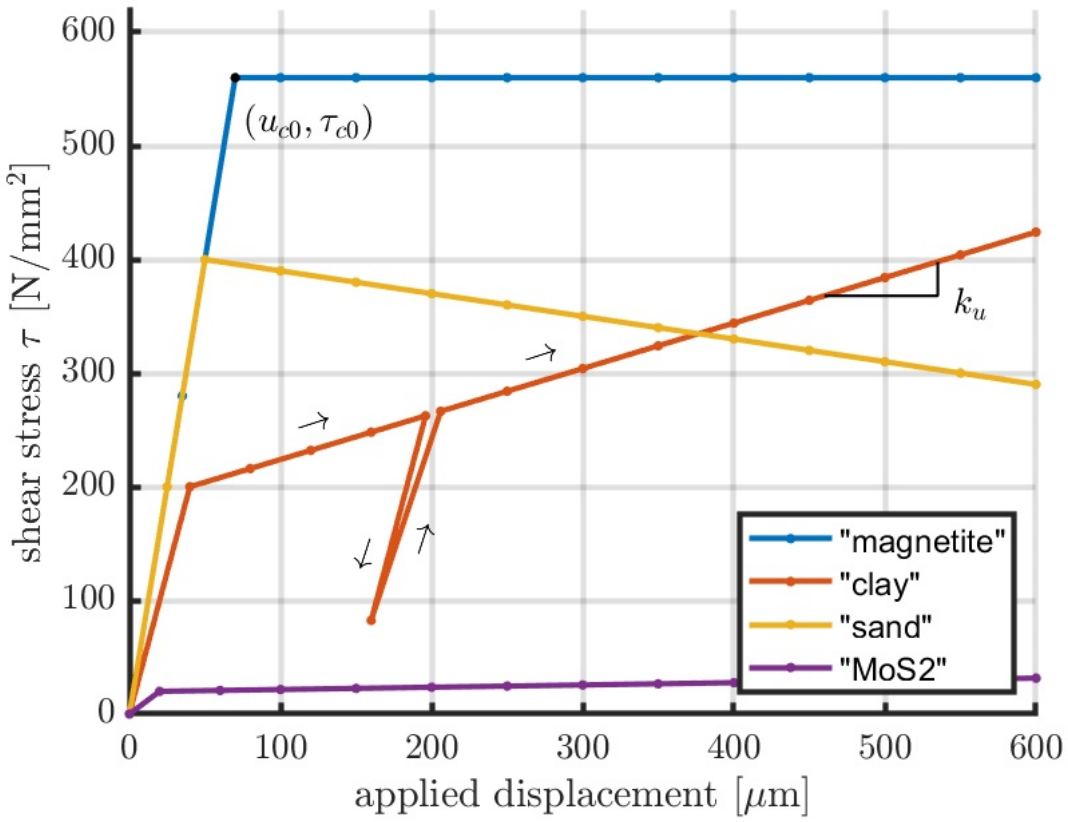

NOTICE

This document is disseminated under the sponsorship of the Department of Transportation in the interest of information exchange. The United States Government assumes no liability for its contents or use thereof. Any opinions, findings and conclusions, or recommendations expressed in this material do not necessarily reflect the views or policies of the United States Government, nor does mention of trade names, commercial products, or organizations imply endorsement by the United States Government. The United States Government assumes no liability for the content or use of the material contained in this document.

NOTICE

The United States Government does not endorse products or manufacturers. Trade or manufacturers' names appear herein solely because they are considered essential to the objective of this report.

REPORT DOCUMENTATION PAGE

Form Approved
OMB No. 0704-0188

1. REPORT DATE *(DD-MM-YYYY)*	**2. REPORT TYPE**	**3. DATES COVERED** *(From - To)*
13/05/2024	Technical Report	April 2017 – November 2019

4. TITLE AND SUBTITLE

Advanced Modeling of Wheel-Rail Friction Phenomena

5a. CONTRACT NUMBER

DTFR5317C00012

5b. GRANT NUMBER

5c. PROGRAM ELEMENT NUMBER

6. AUTHOR(S)

Author Name: E.A.H. Vollebregt, ORCID #0000-0003-2752-1589

Author Name: C.D. van der Wekken, ORCID #0000-0003-3762-2498

5d. PROJECT NUMBER

5e. TASK NUMBER

5f. WORK UNIT NUMBER

7. PERFORMING ORGANIZATION NAME(S) AND ADDRESS(ES)
VORtech BV
Westlandseweg 40d
2624 AD Delft, The Netherlands

8. PERFORMING ORGANIZATION REPORT NUMBER

TR19-11

9. SPONSORING/MONITORING AGENCY NAME(S) AND ADDRESS(ES)
U.S. Department of Transportation
Federal Railroad Administration
Office of Railroad Policy and Development
Office of Research, Development, and Technology
Washington, DC 20590

10. SPONSOR/MONITOR'S ACRONYM(S)

11. SPONSOR/MONITOR'S REPORT NUMBER(S)
DOT/FRA/ORD-24/18

12. DISTRIBUTION/AVAILABILITY STATEMENT
This document is available to the public through the FRA website.

13. SUPPLEMENTARY NOTES
COR: Ali Tajaddini

14. ABSTRACT

From 2017–2019, the Federal Railroad Administration sponsored VORtech and its project partners to develop advanced physics-based modeling of wheel-rail friction. Sub-models were established for the elastic and plastic shearing of third body layers, heating of the contacting surfaces, and effects of these phenomena on the coefficient of friction. The effects of surface roughness and fluids were also considered but were not implemented in the resulting model. The new sub-models were implemented in the 2019 version of the Extended CONTACT software. Measurements from the full-size wheel, bearing and brake test facility from the National Research Council of Canada were evaluated but could not be applied for the evaluation of detailed creep force models. Finally, the resulting version of CONTACT was implemented in four leading simulation codes for vehicle-track interaction, as a prototype (NUCARS, SIMPACK) and in a complete implementation (GENSYS, Universal Mechanism).

15. SUBJECT TERMS
wheel-rail contact, creep force, friction, interfacial layer, simulation

16. SECURITY CLASSIFICATION OF:			**17. LIMITATION OF ABSTRACT**	**18. NUMBER OF PAGES**	**19a. NAME OF RESPONSIBLE PERSON**
a. REPORT	**b. ABSTRACT**	**c. THIS PAGE**		110	**19b. TELEPHONE NUMBER** *(Include area code)*

METRIC/ENGLISH CONVERSION FACTORS

ENGLISH TO METRIC

LENGTH (APPROXIMATE)

1 inch (in)	=	2.5 centimeters (cm)
1 foot (ft)	=	30 centimeters (cm)
1 yard (yd)	=	0.9 meter (m)
1 mile (mi)	=	1.6 kilometers (km)

AREA (APPROXIMATE)

1 square inch (sq in, in^2)	=	6.5 square centimeters (cm^2)
1 square foot (sq ft, ft^2)	=	0.09 square meter (m^2)
1 square yard (sq yd, yd^2)	=	0.8 square meter (m^2)
1 square mile (sq mi, mi^2)	=	2.6 square kilometers (km^2)
1 acre = 0.4 hectare (he)	=	4,000 square meters (m^2)

MASS - WEIGHT (APPROXIMATE)

1 ounce (oz)	=	28 grams (gm)
1 pound (lb)	=	0.45 kilogram (kg)
1 short ton = 2,000 pounds (lb)	=	0.9 tonne (t)

VOLUME (APPROXIMATE)

1 teaspoon (tsp)	=	5 milliliters (ml)
1 tablespoon (tbsp)	=	15 milliliters (ml)
1 fluid ounce (fl oz)	=	30 milliliters (ml)
1 cup (c)	=	0.24 liter (l)
1 pint (pt)	=	0.47 liter (l)
1 quart (qt)	=	0.96 liter (l)
1 gallon (gal)	=	3.8 liters (l)
1 cubic foot (cu ft, ft^3)	=	0.03 cubic meter (m^3)
1 cubic yard (cu yd, yd^3)	=	0.76 cubic meter (m^3)

TEMPERATURE (EXACT)

[(x-32)(5/9)] °F = y °C

METRIC TO ENGLISH

LENGTH (APPROXIMATE)

1 millimeter (mm)	=	0.04 inch (in)
1 centimeter (cm)	=	0.4 inch (in)
1 meter (m)	=	3.3 feet (ft)
1 meter (m)	=	1.1 yards (yd)
1 kilometer (km)	=	0.6 mile (mi)

AREA (APPROXIMATE)

1 square centimeter (cm^2)	=	0.16 square inch (sq in, in^2)
1 square meter (m^2)	=	1.2 square yards (sq yd, yd^2)
1 square kilometer (km^2)	=	0.4 square mile (sq mi, mi^2)
10,000 square meters (m^2)	=	1 hectare (ha) = 2.5 acres

MASS - WEIGHT (APPROXIMATE)

1 gram (gm)	=	0.036 ounce (oz)
1 kilogram (kg)	=	2.2 pounds (lb)
1 tonne (t)	=	1,000 kilograms (kg)
	=	1.1 short tons

VOLUME (APPROXIMATE)

1 milliliter (ml)	=	0.03 fluid ounce (fl oz)
1 liter (l)	=	2.1 pints (pt)
1 liter (l)	=	1.06 quarts (qt)
1 liter (l)	=	0.26 gallon (gal)
1 cubic meter (m^3)	=	36 cubic feet (cu ft, ft^3)
1 cubic meter (m^3)	=	1.3 cubic yards (cu yd, yd^3)

TEMPERATURE (EXACT)

[(9/5) y + 32] °C = x °F

QUICK INCH - CENTIMETER LENGTH CONVERSION

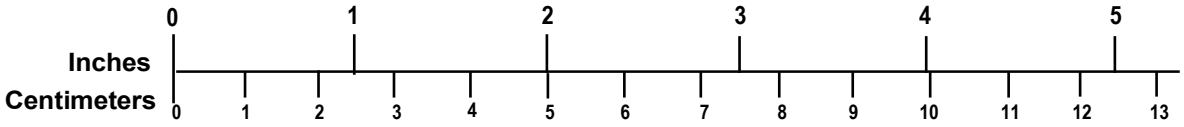

QUICK FAHRENHEIT - CELSIUS TEMPERATURE CONVERSIO

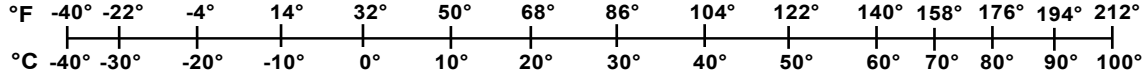

For more exact and or other conversion factors, see NIST Miscellaneous Publication 286, Units of Weights and Measures. Price $2.50 SD Catalog No. C13 10286

Updated 6/17/98

Acknowledgments

The authors wish to express their gratitude to the participants of the friction modeling working group of the International Collaborative Research Initiative on Rolling Contact Fatigue for their valuable discussions and contributions. Special thanks go to (alphabetically) Eric Magel, Kevin Oldknow, Oldrich Polach, and Klaus Six for their reviews of this report and the feedback provided.

Contents

Illustrations

Tables

Executive Summary

Friction plays a key role in many aspects of vehicle-track interaction, such as traction and braking, hunting, lateral/vertical (L/V) forces, wear, and rolling contact fatigue (RCF). Friction varies widely between different circumstances, like sunny or rainy weather, or the presence of sand, clay, rust, leaves, and oil or grease. Furthermore, wheel-rail dynamics do not only depend on the (maximum) level of friction, but on the creepage versus creep-force characteristic (i.e., the change of the creep forces with changing creepage).

While the overall tendencies of friction and creep forces are well understood, the physical mechanisms that lead to them are not. Kalker's wheel-rail contact theories (1990) are restricted to clean surfaces, ignoring the effects of third body layers. In practice, measurements often show deviations from his theoretical curves: a lower initial slope of the traction curve and a reduction of traction forces with increasing creepage after a maximum has been attained. These effects are currently included in modeling efforts only provisionally, capturing the desired characteristics but without a satisfactory explanation.

This hinders the effective engineering and operation of railway systems:

- Research has not identified a common theory by which new information or anecdotes can be understood.
- Experts cannot easily advise users of simulation tools which creep force model is appropriate in which circumstances.
- The parameters obtained from one measurement cannot be accurately applied to other situations.
- The field lacks integrated models for the investigation of higher frequency effects like crack initiation and growth, corrugations, and squeal noise.

This report presents the results of a project undertaken to advance modeling of wheel-rail friction. The research team established sub-models for the elastic and plastic shearing of third body layers, heating of the contacting surfaces, and the effects of these phenomena on the coefficient of friction. They also considered the effects of surface roughness and fluids but did not implement them in the resulting model.

The researchers implemented new sub-models in the well-known CONTACT software. They evaluated measurements from the National Research Council (NRC) Canada’s wheel, bearing and brake test facility but the measurements could not be applied to the evaluation of detailed creep force models. Finally, the team implemented the resulting software in four leading vehicle-track interaction (VTI) simulation codes, as prototypes (NUCARS, SIMPACK) or complete implementations (GENSYS, Universal Mechanism).

The authors recommend the following actions for future work:

- Extend the sub-model for contact temperatures to transient contacts, and the sub-model for local plasticity to non-linear work-hardening characteristics.
- Get detailed measurements to validate the main tendencies predicted by the sub-models and to establish ranges for the input parameters.

- Get detailed measurements to identify the rheology of fluids arising in wheel/rail contacts as a function of pressure and temperature.
- Develop a full model for situations with fluids, using an elasto-hydrodynamic lubrication approach.

1. Introduction

This report presents the results of a project on advanced modeling of wheel-rail friction phenomena. The goals were to better understand the physical processes involved, develop computational models for their simulation, to validate these models using available measurements, and to provide the resulting model to railway engineers, via packages for simulation of vehicle-track interaction (VTI).

The project was organized in three work packages (Vollebregt, 2016):

1. Improve the CONTACT model by incorporating five physics-based sub-models.
2. Validate the resulting model with existing measurements.
3. Provide CONTACT as an extension module to the leading VTI software packages.

This section provides a quick introduction to wheel-rail friction, surveying the variety of circumstances to be modelled, with different demands on the level of detail of the predictions. Relevant phenomena consist of third body layers (both natural and applied), fluids, roughness, heat generation, and the elasticity of the primary bodies.

Sections 2 to 5 present reviews and new modeling work on surface roughness, contact temperature, third body layers, and interfacial fluids. The measurements obtained from the National Research Council (NRC) Canada's full-scale test-rig are analyzed in Section 6. Section 7 discusses the integration of CONTACT in GENSYS, NUCARS, SIMPACK, and Universal Mechanism. The overall conclusions and discussion are finally provided in Section 8.

1.1 Classical Theories for Rolling Contact

Friction plays a key role in many aspects of VTI, such as traction and braking, hunting, lateral/vertical (L/V) forces, wear, rolling contact fatigue (RCF), and more (Figure 1). Conditions such as sunny or rainy weather, and the presence of sand, clay, rust, leaves, oil, or grease, affect friction. Furthermore, wheel-rail dynamics do not only depend on the (maximum) level of friction, but on the creepage versus creep-force characteristic.

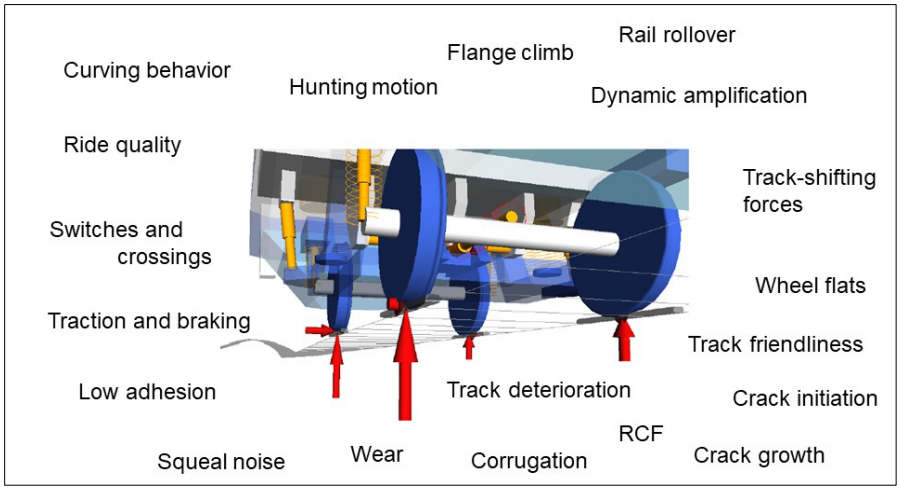

Figure 1. Wheel-rail contact forces play an important role in many aspects of VTI (Vollebregt/Simpack).

Osborne Reynolds recognized the creep phenomenon in the 1870s (Reynolds, 1876). He observed that the distance traversed by a cylinder rolling on a plane could be larger or smaller than the values expected based on the radius and the number of revolutions. The different materials used for the plane and the roller (India rubber, wood, and iron) offered an explanation: larger elastic deformations occur in the softer of the two bodies, altering the velocity of particles in and around the contact. As a result, the roller surface was found to *creep* over the supporting surface: it seemed to be sliding though it did not.

Carter and Fromm mathematically analyzed creepage in the 1920s for the two-dimensional (2D) case (Carter, 1926; Fromm, 1927). Equal materials are used in their analyses. In this case, creepage arises from compression in one body versus elongation in the other. This work was continued in 1950 by Poritsky (1950). These analyses revolve around two key assumptions:

1. Creepage is due to elastic deformation of the materials in/around the contact.
2. Coulomb's law may be applied locally, at every point in contact.

Situations of partial slip arise because of the latter assumption. The contact area is then divided into sticking and slipping zones. A typical pattern of shear stresses arises as shown in Figure 2. These shear stresses may be integrated to find the total force at a given level of creepage. Repeating this for different creepages then produces the creep force curve as shown in Figure 3.

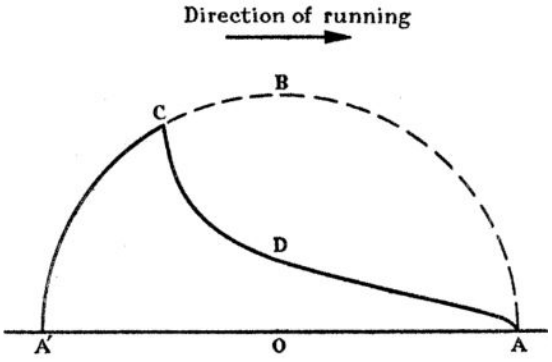

Figure 2. Pattern of tangential shear stresses in 2D steady rolling, slip zone $A' - C$, adhesion/stick: $C - A$ (Carter, 1926)

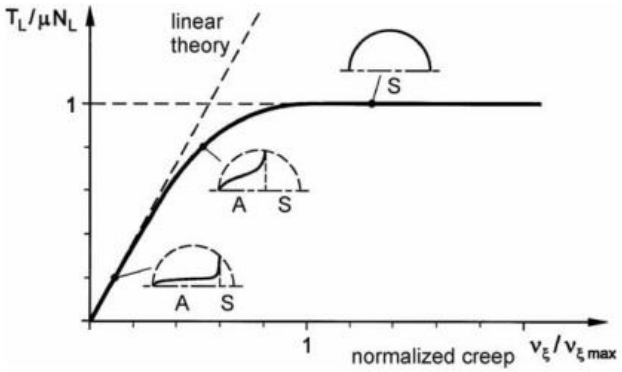

Figure 3. Creep versus creep force characteristic for 2D steady rolling (from Knothe, 2008)

In the 1950s, Johnson presented measurements and modeling work on three-dimensional (3D) configurations (1958b; 1958a), distinguishing longitudinal, lateral, and spin creepage, and

demonstrating their main interactions. Research that followed aimed to understand and predict the nonlinear behavior of the creep forces. Significant contributions were made by Kalker, presenting his linear theory (1967), simplified theory (FASTSIM; 1973, 1982), and full (variational) theory for rolling contact with friction (CONTACT; 1979, 1990).

1.2 Deviating Creep Forces in Railways

The theoretical view of stick and slip zones was confirmed in experimental observations:

> Surface tractions and associated internal stresses have been investigated by photo-elasticity using large epoxy-resin models in very slow rolling (Haines & Ollerton, 1963, 1964). The stick and slip zones were clearly visible. In the slip zone the traction closely follows Amonton's Law of friction as assumed in the theory (Johnson, 1985, p. 265).

Measurements on railway creep forces were conducted by different researchers, as surveyed by Hobbs (1967; Figure 4 and Figure 5).

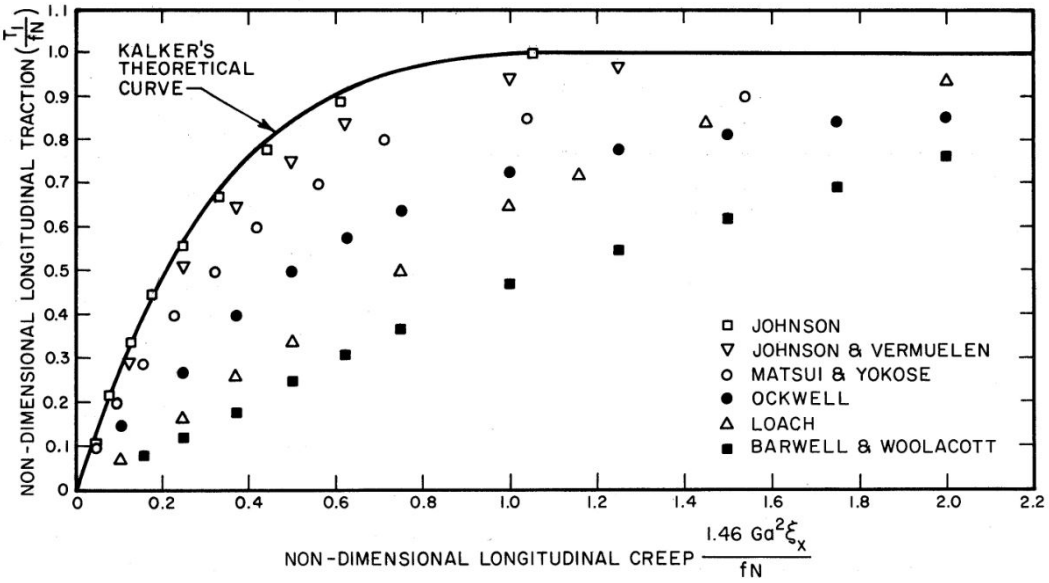

Figure 4. Comparison of longitudinal creep measurements with Kalker's theoretical curve (Hobbs, 1967; Reproduced in Nayak, et al., 1970)

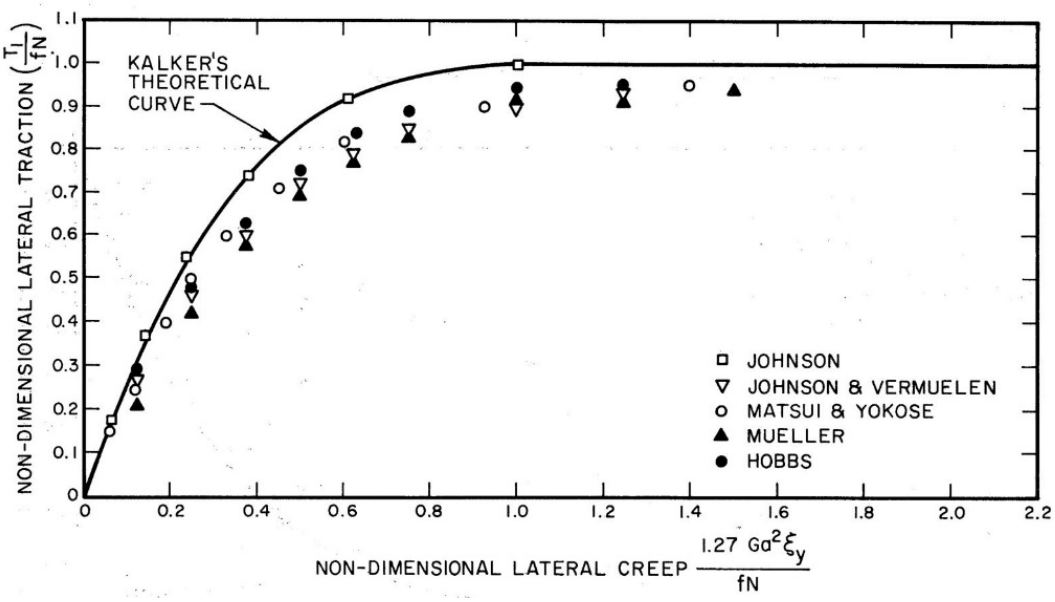

Figure 5. Lateral creep measurements (Hobbs, 1967; Reproduced in Nayak, et al., 1970)

Hobbs concluded:

> It is clear that under carefully controlled laboratory conditions Kalker's complete theory of creep can be verified experimentally, including, in particular, the relationships between tangential tractions, lateral and longitudinal creep and spin.

However,

> A further problem in practice is the effect on creep of surface contamination or boundary lubrication. [...] Some longitudinal creep tests (notably those of Loach, Woolacott, and Barwell) show up to 100% more creep than theory predicts, it is suggested that this is due to surface contamination or lubrication (Hobbs, 1967).

Similar conclusions were drawn from experiments by Brickle (1973) on a twin disk machine and by Illingworth (1973) in a roller rig test.

1.3 Additional Factors Affecting Creep Forces in Railways

Further investigations have been undertaken to identify factors affecting the creep forces. British Rail Research reported on elaborate testing, exploring the influence of oil, wear debris, and water on adhesion (Beagley & Pritchard, 1975; Beagley, et al., 1975a; Beagley, et al., 1975b; Broster, et al., 1974). Friction levels of over 0.6 were obtained on clean, dry rails, while the coefficient of friction (COF) was reduced to 0.3 on wet rails if no oil was present, and to 0.2 if the oil coverage was increased. Lower values could be found in the presence of solid debris.

In 1980, Logston and Itami presented extensive creep-force measurements on locomotive EMD SD45X (Logston & Itami, 1980). They studied dry, wet, and oiled rail conditions, with and without sanding. The results show considerable differences in the shape of the curves for dry and wet conditions, as illustrated in Figure 6. The level of friction reduced in the presence of water. Further, the marked peak found in dry and dry-sanded conditions was also greatly reduced in wet conditions.

Polach (2005) collected measurement data from different locomotives for dry and wet tracks running at different speeds (16–60 km/h). The data generally exhibit the pattern as shown in Figure 6. They could be fitted well by tuning the parameters in Polach's fast computation approach. Further references are given in surveys and in later sections of this report (Meymand, et al., 2016; Magel, 2017).

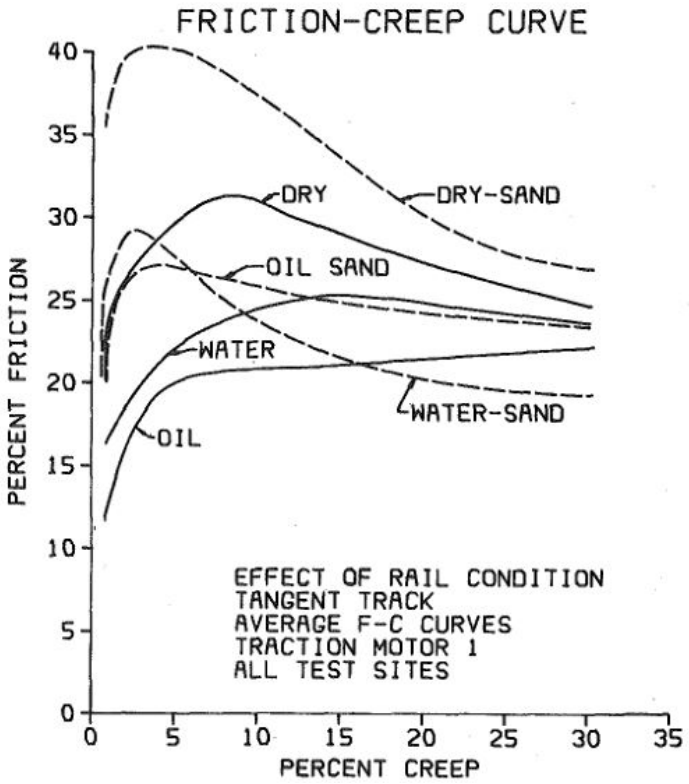

Figure 6. Average friction-creep curves measured on the EMD locomotive SD45X (Logston & Itami, 1980)

1.4 Advanced Modeling of Railway Creep Forces

Multiple extensions of the basic models were studied for different application purposes. Within the context of multi-body simulation (i.e., curving, stability), the focus remained on the classical theory. One extension used to assess the effects of contamination is called the PERCENT_KALKER approach, attributed to Hobbs (Polach, et al., 2006). This consists of reducing the Kalker coefficients that describe the initial slope of creep force curves to 10–100 percent of the theoretical value (for instance, Fries, et al., 2011).

There have been discussions and studies on surface roughness, specifically if or how this affects the shape of the creep force curve (Kalker, et al., 1997; Bucher, et al., 2002). No definitive answer has been obtained, as discussed in Section 2.

The declining region of the creep force characteristic has been used to study squeal noise (Périard, 1998; Monk-Steel, et al., 2006) and locomotive traction power (Polach, 2005; Spiryagin, et al., 2013). Falling friction is obtained from models by postulating a COF decreasing with increasing slip (Giménez, et al., 2005; Polach, 2005; Piotrowski, 2010; Vollebregt & Schuttelaars, 2012), according to a measured or hypothesized dependence. The effect itself is

often attributed to the effects of temperature (Tomberger, et al., 2011; Vollebregt, 2014; Voltr & Lata, 2015), as surface temperatures on locomotive wheels rise easily to $400°C$ or more at large creepage (Hou, et al., 2000). This has been witnessed in martensite formation, which occurs at temperatures over $720°C$. Other effects could contribute to falling friction at the same time or may be the main cause in other circumstances. The effects of wheel-rail contact temperatures are the subject of Section 3.

Godet, Berthier, and others followed an independent line of research (Godet, 1984; Berthier, 1990; Descartes, et al., 2005; Niccolini & Berthier, 2005), introducing the concept of a third body between the wheel and the rail as an alternative means for velocity accommodation.

> A contact is made out of two "first bodies" (i.e., the machine elements) and an intermediate film or third body. Third bodies can be defined either in a general or "material sense" as a zone with a different composition from that of the bulk first bodies or in a "kinematic" sense as a thickness across which the velocity difference between first bodies is accommodated (Godet, et al., 1984).

Kalousek et al. advocated for friction management by changing the third body composition (Kalousek, et al., 1996). Hou et al. (1997) measured the properties of interfacial layers, which are considered a main cause for the reduced initial slope of creep-force curves (Figure 5). Further, Kalousek hypothesized that falling friction may also be attributed to the third body layer, considering the detailed failure mechanisms occurring and the subsequent compacting (Oldknow, personal communication, 2020). Section 4 describes how such interfacial layers are modelled in CONTACT.

The influence of fluids (i.e., water, oil) on railway creep forces have mainly been studied experimentally or modelled in provisional ways. Current physics-based modeling of fluids in railways focuses on the effects of water in high-speed railways (Ohyama, 1991; Chen, et al., 2008; Chen, et al., 2016). Additional works concern the loss of adhesion (Trummer, et al., 2017; Six, et al., 2017). Current restrictions and prospects are discussed in Section 5.

1.5 Scope of Work

This review shows that wheel-rail contact is affected by many factors. A layer of varying composition is formed in the wheel-rail interface, resulting in large variation of the (effective) COF (Figure 7). Many factors contribute to the dynamics of the layer, including thickness and composition, as schematized in the Kalousek bathtub model in Figure 8. The measurements show what kind of behavior may be expected in different circumstances (i.e., the shape of the curves), but quantitative predictions are currently out of reach.

Creep force modeling is complicated by the lack of information on aspects like the maintenance state of vehicles and tracks, and the presence and composition of interfacial layers. Moreover, these circumstances exhibit large variation over time and location. Even if these conditions were known (by careful data acquisition in field experiments or in a laboratory), the physical processes involved are still not well understood. This report focuses on this latter aspect: exploring the effects of surface roughness, temperature, solid interfacial layers, and fluids, contributing to their computational modeling and model validation, and bringing these models to practitioners via simulation packages for VTI.

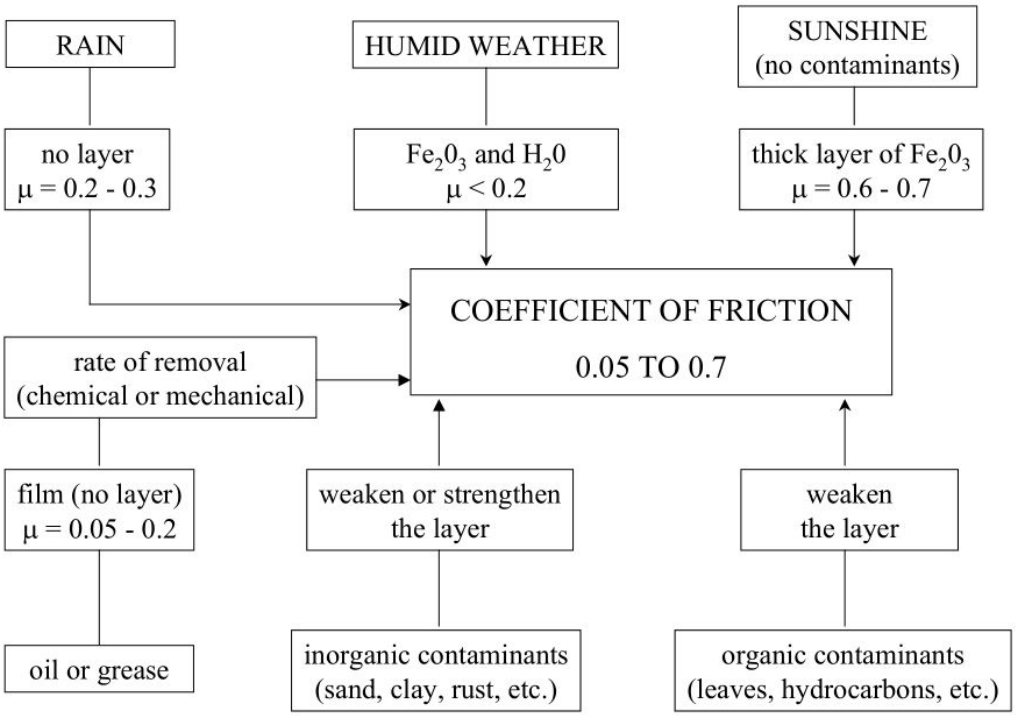

Figure 7. By its open nature, the wheel/rail interface exhibits highly variable levels of friction (Kalousek, reproduced in Magel, 2017).

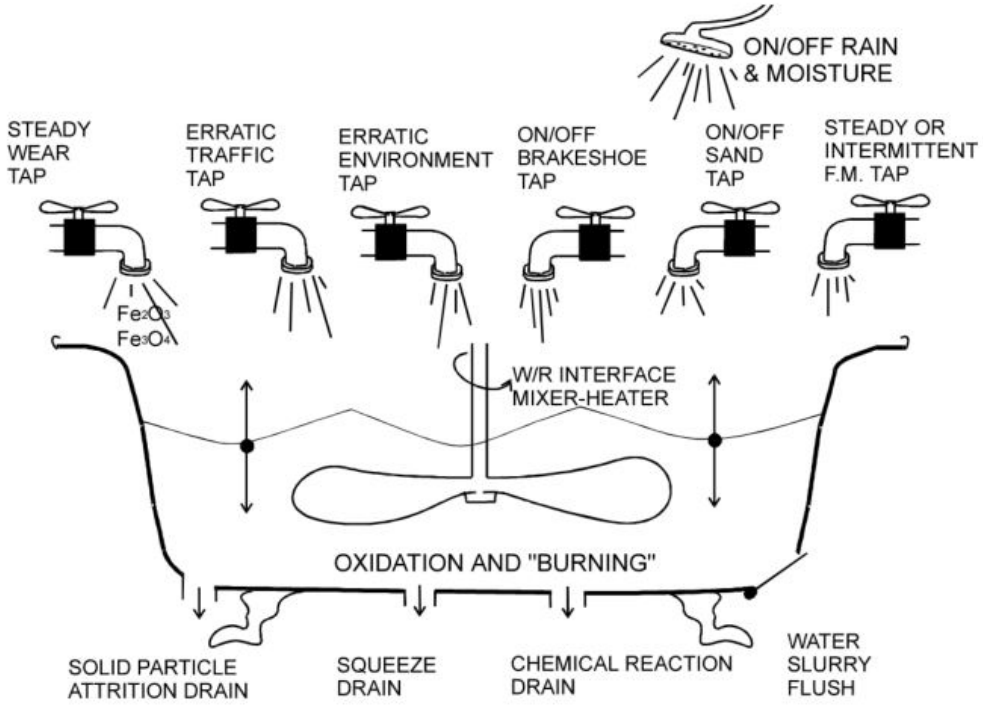

Figure 8. The Kalousek bathtub model, illustrating the various processes contributing to the third body layer (Kalousek, reproduced in Magel, 2017)

2. Effects of Surface Roughness

Engineering surfaces are rough at the microscopical scale (e.g., Figure 9), which affects their contact interactions. This section assesses and reviews these effects along three different directions:

1. The effects of roughness on the real contact area and the pressure distribution
2. The effects of roughness on friction in dry, unlubricated circumstances
3. The effects of roughness on friction in wet or lubricated contacts

In the current project, the main interest lies with the second and third aspects, related to friction. The review concludes that there is *little* influence of roughness on dry friction, and *strong* influence in lubricated conditions.

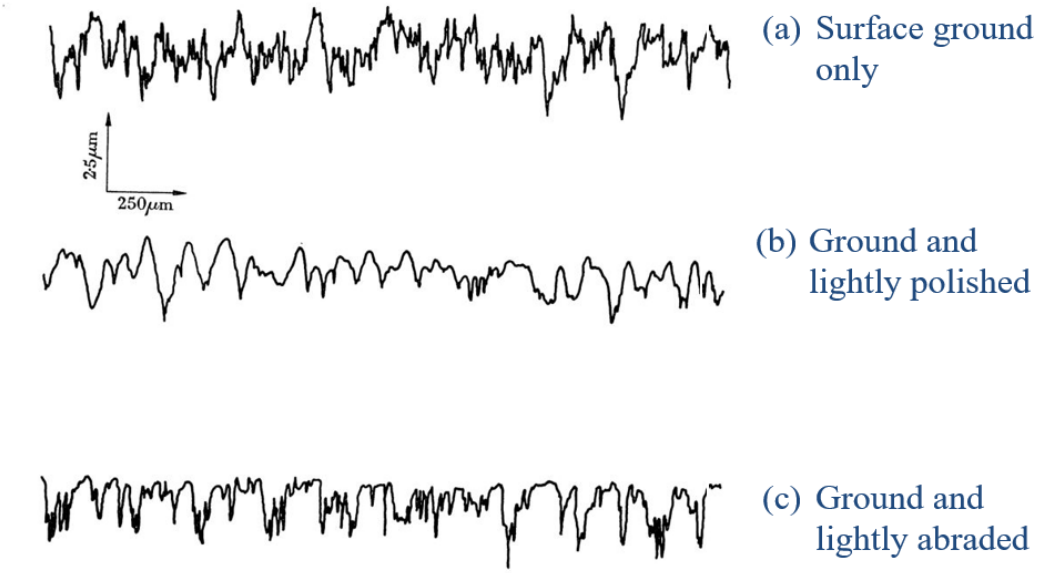

Figure 9. Profiles of mild steel after three surface treatments (Greenwood & Williamson, 1966)

2.1 Real Contact Area

The real area of contact plays an important role in the performance of seals, in thermal and electrical conductivity between contacting surfaces, and in understanding the mechanisms at play. This allows for more targeted investigation of subsequent topics, like friction and wear.

The Greenwood-Williamson (GW) model (Greenwood & Williamson, 1966) is one of the seminal works on rough contacts. It starts from a statistical view on the contacting surfaces, composed of asperities with different heights. As the surfaces are pressed together, more asperities come into contact and the existing contacts grow. The authors analyze the consequences using some simplifications: assuming round asperities of the same size, deforming independently of each other. The analysis resulted in clear conclusions, regarding the contact area, pressures, number of contact spots, etc., as functions of the separation of the surfaces' mean planes.

A main finding from the GW model is that the load and real area of contact are practically proportional to each other, even when only considering elastic contacts.

> This leads us to suggest that the origin of the laws of friction, […] lies not in the ideal plastic flow of individual contact spots but simply in the statistics of rough surfaces (Greenwood & Williamson, 1966).

A plasticity index ψ was defined to characterize the proportion of asperities where plasticity occurs. This parameter appears to be insensitive to the total load borne by the contact. Instead, it depends on material and topographic parameters, like the standard deviation σ of the asperity height distribution and asperity radius β. The plasticity index appears to vary widely between different surfaces; many surfaces already exhibit plastic asperity deformation at the lightest loads, whereas other engineering surfaces predominantly deform in the elastic range.

B. N. Persson (2001) presented a different theory, which begins with a full contact situation. This allows the derivation of a relationship from the statistics of the asperity heights to the statistics of the pressure distribution. The theory seems to depend primarily on the root-mean-squared roughness gradient, another parameter for rough surface topography characterization.

The GW and Persson models are the basis for many other works on rough contacts, including several generalizations. For instance, Ciavarella et al. (2008) consider the interaction between different contacts, Majumdar and Bhushan (1991) use a fractal surface description, and Persson and Scaraggi (2014) include adhesive forces. These works add further understanding and detail to the findings but deviate little from the main trends concerning present interests in friction. See Müser, et al., 2017 and Vakis, et al., 2018 for extensive reviews and further discussions.

Vollebregt (2014) presented extensions of CONTACT to incorporate effects found in measured creep versus creep-force curves that are missing in Kalker's original model. The author considered the real area of contact as a possible mechanism to explain the reduced slope effect observed in experimental creep-force curves. This used a simple idealization of a true surface as flat with equal, evenly spaced pimples (Figure 10). The pimples are shown to deflect tangentially with the formula $u_i = h_i \tau_i / G$, with shear modulus G. The effective stiffness of the layer is then found as $\tilde{G} = A_r/A_n \cdot \tilde{h}/G$. Here A_r, A_n are the real and apparent (nominal) areas of contact, and $\tilde{h}$ is an effective (average) height of the roughness. This suggests that the effective stiffness could be affected considerably by the real area of contact.

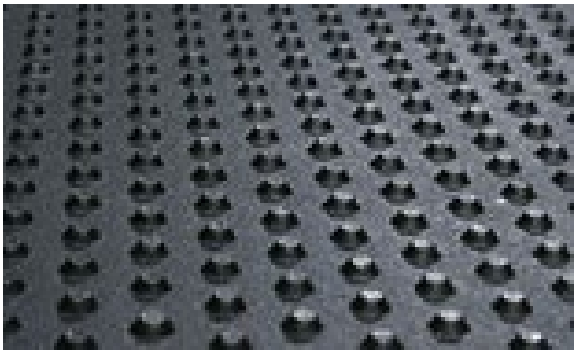

Figure 10. Idealized flat surface with evenly spaced cylindrical pimples (Agromatic, Inc.)

Through their experiences working with Extended CONTACT, the authors changed their perspectives on this mechanism using pimples. For high loads as found in railways, a percentage

of real contact is expected of $\frac{A_r}{A_n} \approx$ 5–30 percent. Unrealistically large heights $\tilde{h}$, (e.g., 1 mm), are needed then to get to the initial slope of the creep curve observed in practice. That is, the distances by which wheel and rail surfaces are found to creep with respect to each other, cannot be explained by the asperities' tangential deflection alone.

Consequently, the authors see no direct relationship from the real area of contact to the local COF in wheel-rail contact situations.

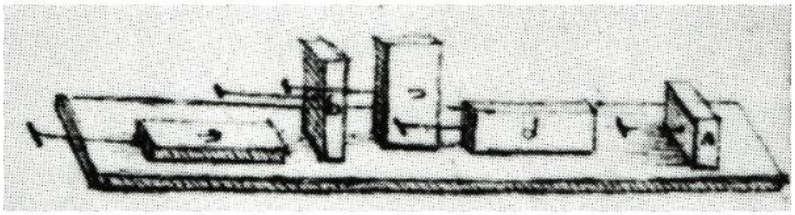

Figure 11. Drawing from the notebooks of Leonardo da Vinci illustrating the independence of friction from the apparent contact area (i.e., footprint; Popov, 2010)

2.2 Friction in Dry Contacts

The effects of surface roughness on the (maximum) level of friction have not been fully resolved. Many different statements can be found in the literature, sometimes contradicting each other. This is attributed to the different scales (microscopic versus macroscopic friction) and physical processes involved (dry versus lubricated, metals versus rubber, heating, wear, plastic deformation, etc.). Here, the authors restrict attention to dry friction at the macroscopic scale, as found in wheel-rail interaction.

Popov (2010) presents an elegant discussion of dry, Coulomb friction. The main aspects of this are well-known:

- Static friction: the force needed to set a body in (sliding) motion is roughly proportional to the normal force $F_s = \mu_s F_n$.
- Kinetic friction: a resisting force $F_k = \mu_k F_n$ acts on the body at continued sliding.
- F_s and F_k show no considerable dependence on the apparent contact area (Figure 11).
- The coefficient of kinetic friction is approximately equal to the coefficient of static friction $\mu_k \approx \mu_s$.

Coulomb found that "F_s and F_k show no considerable dependence on the surface roughness." Popov (2010), discusses this further, using Rabinowicz's experiment:

> Experimentation dealing with the transfer of radioactive elements between two contact partners offers an impressive verification for the weak dependence of friction (and wear) on the surface roughness. In [Figure 13], the results of the experiment are presented, in which a radioactive copper block is drug over a copper plate which has a roughness of 25 nm on one part and a roughness 20 times larger on the other (500 nm). The large difference in roughness has almost no influence on the frictional force and the material transfer from one of the bodies to the other (which one can see by the subsequent radioactivity measurement). The roughness does not even have an impact on the size of the contact areas (Rabinowicz, 1995)

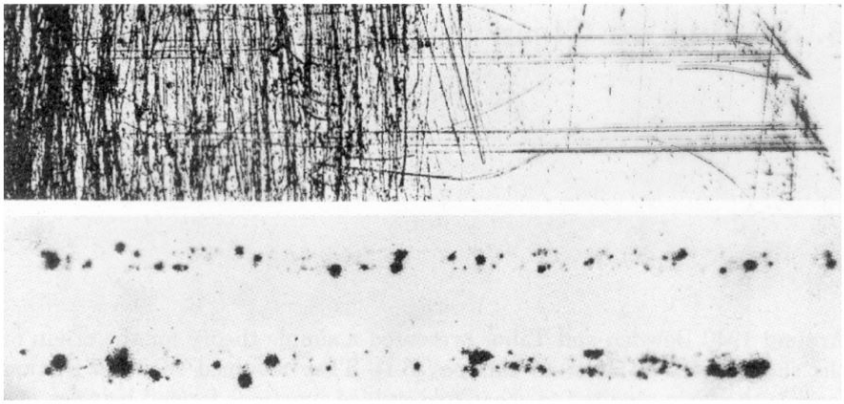

Figure 12. Top: Copper surface with roughness 500 nm on the left and 25 nm on the right, bottom: radioactive material transfer found in two friction experiments (Rabinowicz, (1995)

Lim and colleagues (1989) present an alternate view:

> Our data add to the accepted view: at slow sliding speeds, the coefficient of friction depends on surface roughness, but not on sliding conditions – meaning normal load F and sliding velocity v. At higher speeds […], the surface condition is modified by local heating (which can cause oxidation or even melting); then μ depends in a reproducible way on the sliding velocity [Figure 13] and the bearing pressure F/A_n.

The view of Popov and Rabinowicz is corroborated by numerical modeling of railway creep forces (Zhu, et al., 2013). Little influence of surface roughness is found on adhesion coefficients at small creep values in dry condition. The same is reported by Fulford (2004) on research done by British Rail Research: "No correlation was found between rail roughness and adhesion," and by Magel (2017) for laboratory testing performed in Japan (Ban, 2004), considering the anisotropy introduced by wheel truing: "...the increased surface roughness did not give rise to higher friction levels, and in fact friction tended to be lower for the higher surface roughness."

An observation by Wu and Wilson (2006) points again in the opposite direction:

> Flange climb derailments have been reported to occur at curves or switches in maintenance yards when the cars were just out of the wheel truing machines. This type of derailment is probably caused by the wheel surface roughness after wheel truing.

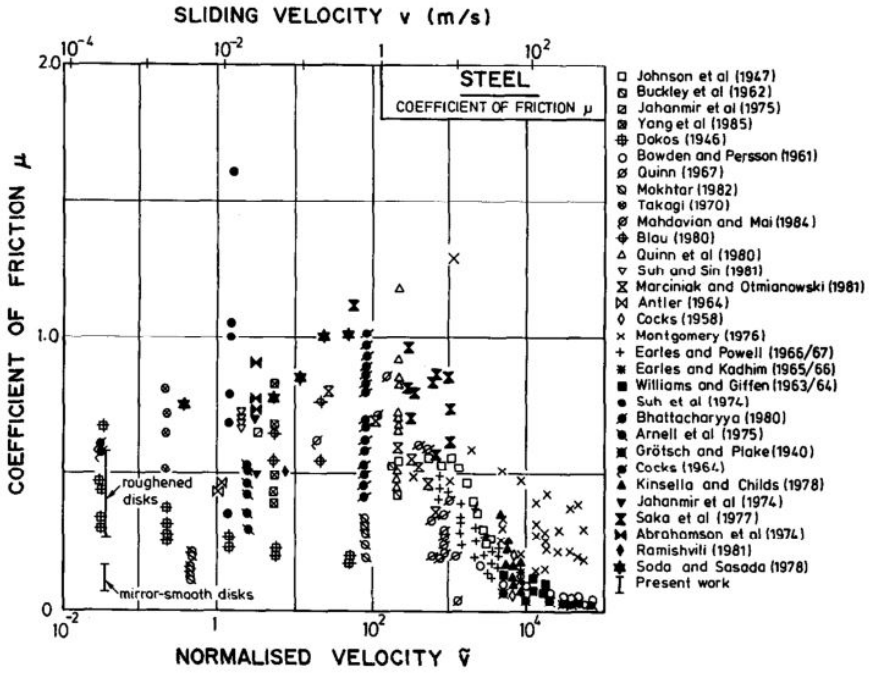

Figure 13. The variations in COF μ with normalised sliding velocity $\tilde{v}$ for unlubricated steel on steel contacts (Lim, Ashby, and Brunton, 1989)

A possible explanation is that friction is higher after wheel truing, due to a cause other than increased surface roughness. According to Magel (2017), this could be the relatively uncontaminated wheel surface. A similar conclusion is presented by Nayak and colleagues (1970):

> Surface roughness influences the rolling [coefficient of friction], rough surfaces generally having a higher coefficient than smooth surfaces. This is particularly true either when the surfaces are very clean (as with a plasma torch) or highly contaminated. Surface roughness has a smaller influence on boundary-lubricated surfaces.

These discussions concern the effect of roughness on the COF. Researchers are also considering the effect that surface roughness could have on the initial slope of the creep versus creep-force characteristic. Nayak, et al. (1970): "Surface roughness has no effect on creep coefficients [i.e., the initial slope] for dry contact at usual operating loads, if surface vibrations are not present."

Halling and Brothers (1966) found the same to be true for the creep of rolling balls at high contact pressures. However, Johnson (1985, p. 268) states:

> Under engineering conditions, such as are encountered on railway tracks for example, the creep coefficients [the initial slope] are observed to be much less than their theoretical values (Hobbs, 1967). A serious cause of this discrepancy lies in the lubricating effect of contaminant films, particularly oil or grease, on the rolling surfaces (Halling & Al-Qishtaini, 1967). Surface roughness and vibration are also likely causes of reduced creep coefficients in practice.

Note that surface roughness is used here to explain a reduction of the initial slope of the curve presenting the creep force, as opposed to an increase of the COF.

Opposite positions are taken by different scholars with regards to modeling. Kalker et al. state:

> Not long after the publication of Kalker in 1967, it was observed that the measured creep [force] in the wheel-rail system was considerably smaller than that of *(Kalker, 1967)*. It seemed that asperities were at the bottom of this, since, by them, the material near the surface would seem weakened. To verify this, it was of minor importance how the asperities were formed, as long as this weakening would seem to be present.
>
> A sinusoidal, two-dimensional surface provided a good model. As a result, it was found, however, that the asperities had ABSOLUTELY NO effect on the creep. It turned later out that contamination was the cause of the effect (Kalker, et al., 1997).

However, Bucher et al. state:

> Our results, as first presented in (Knothe & Theiler, 1996), are in contrast to the ones of Kalker et al. (1997), who claim that the smaller gradients in the experimental curves are only due to interfacial fluid layers. We will show that even in dry contact the gradient is influenced by what may be called the boundary roughness layer (Bucher, et al., 2002).

The authors of the current report believe the discrepancy comes from different computing methods used by the groups. Bucher et al. used the steady rolling approach, in which each asperity goes in and out of contact many times, slipping at the trailing edge of each contact spot individually (Bucher, et al., 2002). Kalker, on the other hand, used the transient rolling approach, where each asperity stays in contact much longer. This allows for stresses to build up longer, hence the larger creep force at a fixed creepage. Whereas the transient approach seems better suited to simulate the effects of roughness, simulations alone are insufficient for conclusions on this issue. Experimental investigations could provide more detailed, useful insights.

2.3 Friction in Lubricated Contacts

Contrary to the situation for dry contacts, there's abundant evidence for the importance of surface roughness in the presence of lubrication. For results pertaining to railways see Ohyama, 1991, Chen, et al., 2008, and Chen, et al., 2016.

The different operating regimes are illustrated in Figure 14 and Figure 15. Patir and Cheng (1978) state:

> The ratio h/σ is an important parameter showing the effects of surface roughness. For $h/\sigma \gg 3$, the roughness effects are not important, and smooth film theory is sufficiently accurate. The roughness effects become important as $h/\sigma \to 3$. As h/σ is decreased further, asperities start interacting with each other and contacts form.

Here, h is the nominal fluid film thickness, defined as the distance between the mean levels of the two surfaces, and σ^2 is the variance of the combined surface roughness.

The objective of bearing design is usually to minimize frictional losses. This is achieved with a continuous fluid film of minimum thickness separating the two surfaces. Increasing the film thickness leads to increased losses in the fluid due to viscosity, whereas reduced thickness leads to direct contact of two surfaces, with asperities touching. As stated by Patir and Cheng (1978), there is a direct correspondence from the surface roughness σ to the film thickness h needed for full film lubrication.

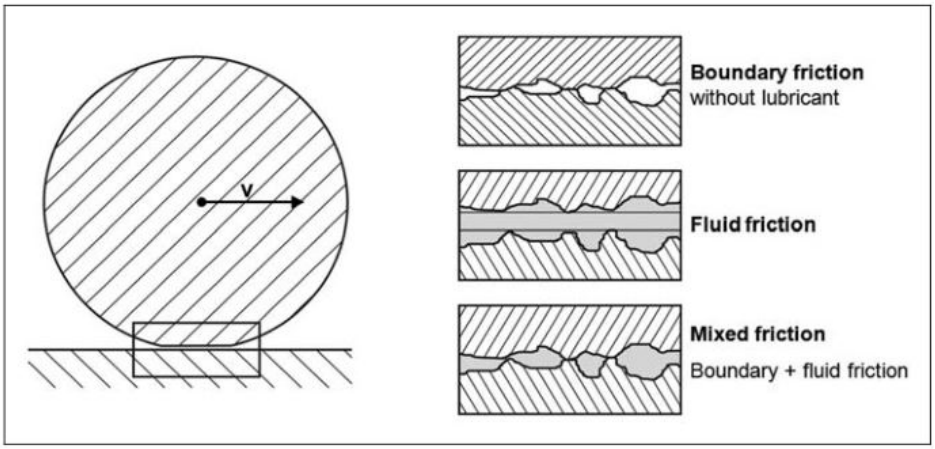

Figure 14. Illustration of different lubrication regimes (Neubert, et al., 2013)

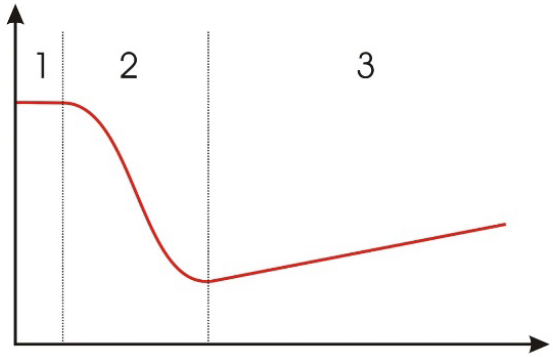

Figure 15. Schematic Stribeck curve, 1: dry/boundary lubricated regime, 2: mixed (partial) lubrication, 3: hydrodynamic (full film) lubrication. Horizontal: Hersey number (viscosity · speed / load), vertical: COF

Johnson et al. (1972) discuss the load-sharing concept, which is used frequently to understand contacts in the mixed lubrication regime. This concept says that the total load F_n is carried partly at the asperities, with the remainder carried by the fluid:

> We are concerned with how the division of the total pressure p into fluid pressure p_f and asperity pressure p_a is governed by the properties of the surfaces and the conditions of lubrication. (Johnson et al., 1972)

This idea is also used in adhesion modeling for railways (Chen et al., 2011 and 2016; Tomberger et al., 2011). These models are straightforward concerning surface roughness, and essentially use the GW-model described in Section 2.1. The more complicated parts of these modeling efforts lie in the build-up of fluid pressure and the corresponding elastic deformation.

2.4 Conclusions Regarding Surface Roughness

This section surveyed literature about the role of surface roughness in contact interactions. The conclusions are:

1. Surface roughness has a strong influence on the real area of contact. This is of interest for understanding the origins of friction but is less interesting for the formulas by which this is described.
2. In dry circumstances, there appears to be little or no influence of surface roughness on the maximum level of creep-force curves, but the issue has not been completely addressed.
3. The authors believe that surface roughness cannot explain a strong reduction of the initial slope of creep force curves, though this issue has also not been solved.
4. Surface roughness is important on wet rails or when using lubrication, affecting fluid flow in a boundary layer of a thickness $h \approx 3\sigma$ and consequent load sharing.

Elasto-hydrodynamic lubrication modeling (EHL) is used in different forms for the computation of friction in lubricated conditions. This uses a straightforward approach for the roughness characterization, basically relying on Gaussian statistics.

For the current project, the authors conclude that no further modeling is needed for dry circumstances, and the Gaussian approach is appropriate for lubricated conditions.

3. Effects of Temperature on Friction

Measured creep versus creep-force curves often show “falling friction”, i.e., traction forces decreasing at higher creepages, after attaining a maximum value around 0.5–3 percent creep (Polach, 2005; Vollebregt, 2014; Figure 16). This is often attributed to the effects of temperature, although other effects may also be involved.

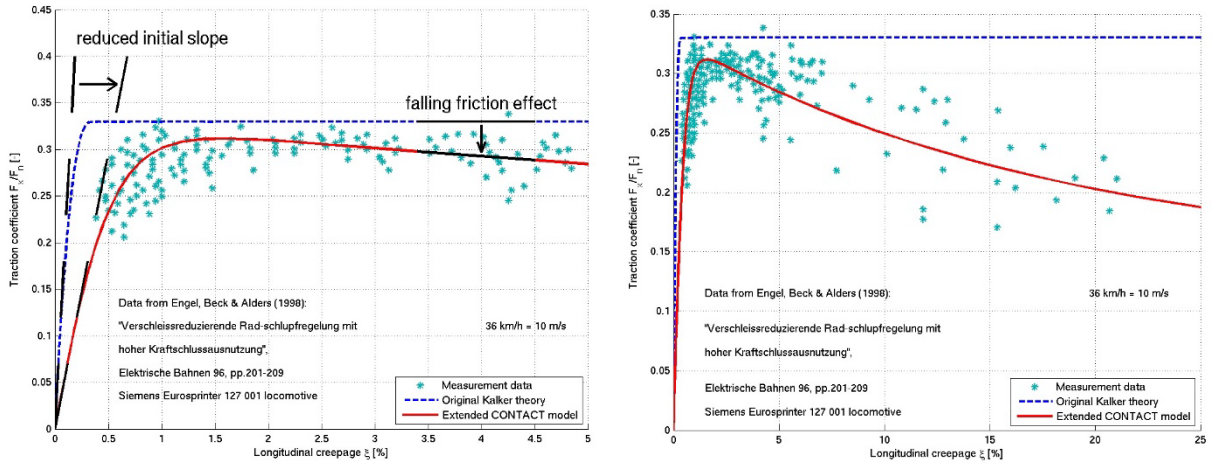

Figure 16. Measured and computed creep forces for the Siemens locomotive EuroSprinter 127001 for pure longitudinal creepage (Vollebregt, 2014)

The common approach to model falling friction is to postulate that the COF decreases as a function of slip velocity (e.g., Périard, 1998; Giménez, et al., 2005; Polach, 2005; Piotrowski, 2010; Vollebregt, 2014; Vollebregt, 2015). The drawback of this is that the coefficients used include effects of the contact geometry. Therefore, the input parameters used have little predictive value and must be fitted to measured values for each situation.

An alternative approach is to compute the surface temperatures using a physics-based model for frictional heating, and then hypothesizing that the material properties and COF decrease with increasing surface temperature (Hou & Kalousek, 2000; Tomberger, et al., 2011). This strategy is adopted in the present work and implemented in CONTACT.

Section 3.1 describes the modeling and calculation of surface temperatures. The consequent effects on friction are discussed in Section 3.2. Numerical results are presented in Section 3.3.

3.1 Computation of Wheel-Rail Surface Temperatures

3.1.1 Scope of the Current Work

The main principles of wheel-rail contact temperatures are well understood (Blok, 1937; Jaeger, 1942; Carslaw & Jaeger, 1959; Blok, 1963; Knothe & Liebelt, 1995; Ertz & Knothe, 2002). These are:

- Frictional heating may yield a substantial increase of the wheel and rail surface temperatures, by 500°C in specific circumstances.

- Due to the short contact duration, these high temperatures are confined to a thin layer, with a penetration depth of $O(100\mu m)$;
- Due to the short contact duration, heat transfer is effectively 1D, normal to the contacting surfaces. This is the case at Péclet numbers larger than 10 or 20 (Ertz & Knothe, 2002; Spiryagin, et al., 2010), while the Péclet number could rise to 2,800 for wheel-rail scenarios (Fischer, et al., 2003).
- The main heat flows are the frictional heat input and "rail chill", i.e., heat transfer from the wheel to the rail. The energy spent on wear (10 percent; Sawley, 2007) and convection to the ambient air (1 percent; Ertz & Knothe, 2002) are of smaller importance.

Ertz and Knothe (2002) provide detailed solutions and approximations for temperatures in Hertzian contacts in steady rolling. They provide solutions for the surface and the subsurface inside the contact area, and for the subsurface outside the contact. They also consider heat conduction from wheel to rail (i.e., rail chill), heat loss due to radiation, and long-term steady state solutions in which the wheel has warmed. They conclude that roughness has little effect on the increase of bulk temperature due to frictional heating.

For this research, the authors are only concerned with calculating the average surface temperatures according to the methods presented by Ertz and Knothe (2002). That is, local flash temperatures due to surface roughness (e.g., Fischer, et al., 2003) are ignored. Like Ertz and Knothe, the research team use the steady rolling assumption. This simplifies administration, because the heat inputs of all prior times t' are contained in the heat input at the current time t, at shifted positions $x - V(t - t')$. A quasi-static approach is used where the overall wheel temperature is given beforehand. The tangential surface tractions and corresponding heat input are assumed to be known in the temperature calculation. The method is extended to non-Hertzian contacts using piece-wise constant discretization.

3.1.2 Mathematical Modeling

The temperature in the wheel and rail are space and time varying functions $T(x, y, z, t)$. By the large ratio of surface speed to rate of diffusion into the solid, the transport is effectively perpendicular to the surfaces (Johnson, 1985; Ertz & Knothe, 2002). This allows computation of temperatures separately for each (material-fixed) position $[x, y]^T$. Concentrating on one such vertical column, the temperature field is $T = T(z, t)$, and evolves by conduction as

$$\frac{\partial T}{\partial t} - \kappa \frac{\partial^2 T}{\partial z^2} = \dot{q}(z, t). \tag{1}$$

Here $\kappa = \lambda/\rho c_p$ is the thermal diffusivity, combining thermal conductivity λ, density ρ and specific heat capacity c_p, and $\dot{q}$ is the source term, the volumetric heat flux. The value of κ may be different for the wheel ($z < 0: \kappa = \kappa_w$) and the rail ($z > 0: \kappa = \kappa_r$). These values are assumed constant in time.

Due to local sliding, a point $[x, y]^T$ at the wheel surface moves continuously from the matching point $[x, y]^T$ to another point $[x', y']^T$ at the rail surface. This enters the temperature problem through the dependence of T on the position $[x', y']^T$. Ertz and Knothe (2002) model this by using the heat partitioning factor, using quantities as defined in Figure 17.

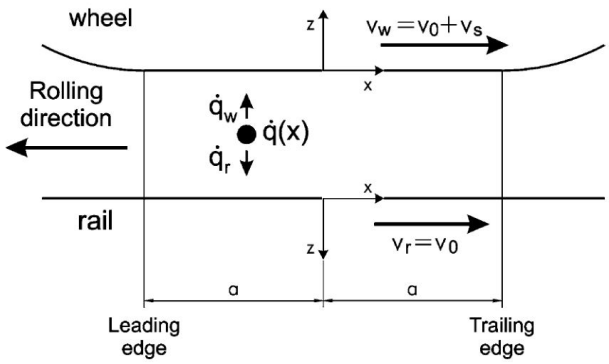

Figure 17. Coordinate system for temperature calculation in wheel/rail contact (Ertz & Knothe, 2002)

$$\varepsilon_w = \frac{\beta_w\sqrt{v_w}}{\beta_w\sqrt{v_w} + \beta_r\sqrt{v_r}}, \quad \dot{q}_w = \varepsilon_w \dot{q}_{friction}, \quad \dot{q}_r = (1-\varepsilon_w)\dot{q}_{friction}, \tag{2}$$

$$\text{with } \dot{q}_{friction} = \dot{q}(x,y) = \mu p_n s_a, \quad s_a = V\|\vec{s}\| \tag{3}$$

Here $\beta = \sqrt{\lambda\rho c_p} = \lambda/\sqrt{\kappa}$ is the thermal penetration coefficient and $\dot{q}_{friction}$ is the total frictional heat input and $\vec{s}$ the dimensionless relative slip velocity. This partitioning of Equation 2 was obtained from a mathematical argument on wheel and rail surface temperatures. For similar wheel and rail materials and about 2 percent sliding, this gives $\varepsilon_w \approx 0.505$.

The research team believes that the derivation of Equation 2 may not be appropriate. A complication is found by considering a localized heat input at the leading edge of the contact area, $x = -a$, i.e., $\dot{q}_{friction}(x) = \delta_{dirac}(x + a)$. Assuming $v_w > v_r$, the bigger fraction of $\dot{q}_{friction}$ will flow into the wheel and a smaller fraction into the rail. Next, for any position x in the contact area, the rail has been in contact longer than the corresponding wheel particle, allowing more $\dot{q}_{friction}$ to be conducted away from the surface (bigger t' in Ertz & Knothe, 2002). This predicts different temperatures at the same location x in the wheel and rail surfaces, whereas these temperatures should equal each other.

The complication of Equation 2 is that it equates wheel and rail surface temperatures that are obtained from the 1D model (Ertz & Knothe, 2002), whereas the phenomenon at stake is 2D by nature. Local sliding brings advection into the system that is ignored in the 1D solution. The research team avoids this complication by ignoring the velocity dependence of the heat partitioning factor, turning it into a simpler form:

$$\varepsilon_w = \frac{\beta_w}{\beta_w + \beta_r} \tag{4}$$

The heat input is equally distributed between the two bodies $\varepsilon_w = 0.500$ in case similar materials are used for the wheel and rail.

Time t is counted from the moment the vertical column $[x, y]^T$ enters the contact area. The temperature evolution is then computed in two stages, separately for points inside and outside the contact area.

1. Upon entering the contact area at $t = 0$, the temperature is assumed constant in the wheel and in the rail, at possibly different background or bulk temperatures.

$$T(z,0) = \begin{cases} T_{w0} & z < 0 \text{ (wheel)} \\ T_{r0} & z > 0 \text{ (rail)} \end{cases} \tag{5}$$

2. For times $0 < t < t_{end}$ where the point $[x, y]^T$ is in the contact area, Equation 1 holds for $z \in \mathbb{R}$, with temperatures held fixed at infinite depth, at T_{w0} and T_{r0}, and with non-zero heat input $\dot{q}_{friction}$ due to local sliding, using a point source (Dirac delta) at $z = 0$.

   Upon making contact, the wheel and rail temperatures jump to an intermediate value at $z = 0$: the average $(T_{w0} + T_{r0})/2$ when thermal diffusivities are equal, $\kappa_w = \kappa_r$, or a nearby value when $\kappa_w \approx \kappa_r$. This yields a step temperature profile that will become increasingly gradual over time, by heat flow from the warmer wheel to the rail.

   By the linearity of Equation 1, the effect of heat input $\dot{q}_{friction}$ may be computed separately and then be superimposed. Its effect is to elevate the temperatures at and around $z = 0$. The maximum values are not necessarily found at $z = 0$ if the heat input $\dot{q}_{friction}$ is time-varying.

3. After leaving the contact area at $t = t_{end}$, Equation 1 is solved separately for the wheel, $z \in (-\infty, 0]$, and for the rail, $z \in [0, \infty)$, without further heat input, and with Neumann condition $\partial T/\partial z = 0$ at $z = 0$ (isolated boundary).

   Without further heat input, the temperature distribution that existed at $t = t_{end}$ will be smoothed over time. All heat input or net cooling spreads into the bulk of the material, such that the temperature tends to the background value as $t \to \infty$.

Following Ertz, the solution is constructed from two different contributions.

1. Convection: The solution for heat flow from the wheel and rail $T_{w0} > T_{r0}$ due to different initial conditions (Equation 5) without heat input due to friction.
2. Heat input: The solution for the temperature raises due to friction $\dot{q}_{friction}$ with equal initial conditions for the wheel and the rail.

By linearity, the two solutions may then be added together.

3.1.3 Rail Chill: Heat Convection from the Wheel to the Rail

Ertz & Knothe (2002) provide equations for the heat flow from the wheel into the rail. Before contact, the rail has an initial temperature of $T_r(x) = T_{r0}$ (rolling to the left: $x \in (-\infty, -a)$) and the wheel has initial temperature $T_w(x) = T_{w0}$. Upon contact, the temperatures at the surface become equal instantaneously, such that $T_r(x) = T_m = T_w(x)$. The value of T_m is obtained from the condition that the heat fluxes are equal for the wheel and the rail:

$$T_m = T_{r0} + \varepsilon_w (T_{w0} - T_{r0}). \tag{6}$$

Note that Ertz's model is extended with a nonzero background temperature T_{r0} for the rail.

Without frictional heat production, T_w and T_r stay constant in the contact area (and equal to T_m). After leaving the contact ($x \in (a, \infty)$), the wheel surface temperature is found as:

$$T_w(x) = T_{w0} - (T_{w0} - T_{r0}) \cdot \left(\frac{2}{\pi}(1 - \varepsilon_w) \operatorname{asin} \sqrt{\frac{2a}{x + a}} \right). \tag{7}$$

This is derived from Ertz and Knothe's (2002) Equation 47, extended for nonzero T_{r0}, without coordinate scaling.

The denominator in the square root measures the distance from the leading edge of the contact area. For rolling to the right, this changes to $a - x$. In both cases, the argument to asin gives $+1$ at the trailing edge of the contact area, such that the equation reduces to $T_w = \varepsilon_w\, T_{w0} + (1 - \varepsilon_w) T_{r0} = T_m$.

The use of a in Equation 7 stems from the depth to which the heat exchange has penetrated: the longer that the particles were in contact, the smoother the initial step profile has become, and the longer it takes before the background temperature is restored. This is implemented in CONTACT by counting the number of elements in contact and multiplying with the element size δx. Non-elliptical contact shapes are supported this way.

3.1.4 Analytical Solution for Frictional Heat Input

The second part of the solution considers the frictional heat input. The general solution for the corresponding temperature increase is obtained from Carslaw and Jaeger (1959), presented by Ertz and Knothe (2002):

$$T(z,t) = \frac{1}{\beta\sqrt{\pi}} \int_{t^*=0}^{t} \dot{q}(t - t^*) \exp\left(-\frac{z^2}{4\kappa t^*} \right) \frac{dt^*}{\sqrt{t^*}}\,. \tag{8}$$

Here, the notation t^* is used for the time difference instead of t', because t' is used in CONTACT to denote a previous time instance. At the surface $z = 0$ this simplifies to

$$T(0,t) = \frac{1}{\beta\sqrt{\pi}} \int_{t^*=0}^{t} \frac{\dot{q}(t - t^*)}{\sqrt{t^*}}\, dt^*. \tag{9}$$

The thermal input $\dot{q}(t)$ is originally derived from a space and time dependent function $\dot{q}(x, y, t)$. Assuming a steady contact situation, there is a fixed profile $\tilde{q}(\tilde{x}, \tilde{y})$ being shifted over the wheel and rail surfaces. This allows for mapping the time function $\dot{q}(t - t^*)$ to a spatial function $\dot{q}(x')$ over the contact area. The first step is to introduce the previous time $t' = t - t^*, dt' = -dt^*$ instead of the time difference t^*:

$$T(0,t) = \frac{1}{\beta\sqrt{\pi}} \int_{t'=0}^{t} \frac{\dot{q}(t')}{\sqrt{t - t'}}\, dt'. \tag{10}$$

Next, the positions of the particle are described as $x = -a + Vt$ and $x' = -a + Vt'$, with $dx' = V\, dt'$. Equation 10 is thus transformed into an integral from the leading edge $x' = -a$ to the current point x:

$$T(0,x) = \frac{1}{\beta}\frac{1}{\sqrt{\pi}} \int_{x'=-a}^{x} \frac{\dot{q}(x')\sqrt{V}}{\sqrt{x - x'}} \frac{dx'}{V} = \frac{1}{\beta}\frac{1}{\sqrt{\pi V}} \int_{x'=-a}^{x} \frac{\dot{q}(x')}{\sqrt{x - x'}}\, dx'. \tag{11}$$

This corresponds to equations 16 and 17 in Ertz and Knothe (2002) at the surface $\zeta = z = 0$, without coordinate scaling.

3.1.5 Discretization in CONTACT

The main challenge in the implementation in CONTACT is adapting the temperature model to CONTACT's grid discretization. The natural integration points for the temperature model are at the ends of time intervals $[t, t+\delta t]$, corresponding to faces of grid discretization elements, whereas CONTACT's primary quantities are located in the element centers as shown in Figure 18. A second aspect to account for is that the sliding velocity is not constant but different per element $I = [i_x, i_y]$.

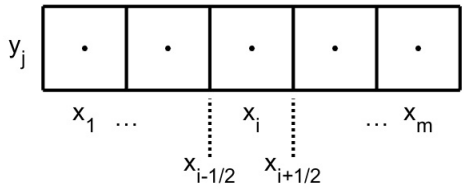

Figure 18. The contact grid consists of cells i and cell faces $i \pm 1/2$.

CONTACT's grid discretization is first order accurate (Vollebregt, 2009). The continuous tractions $\vec{p}(x,y)$ are approximated using a piece-wise constant discretization. The elemental tractions $\vec{p}_I$ represent the average value within an element I, and represent the value at the central position $\vec{x}_I = [x_I, y_I]^T$. The micro-slip velocities $\vec{s}_I$ are somewhat more cumbersome. They are used in two different ways:

1. The traction is opposite to the slip direction, which is enforced at the element centers.
2. The slip, rigid slip, and elastic deformation add up, which is a balance equation between I and the upstream point $I-1$ or $I+1$ when rolling to the left or right, respectively.

The authors chose to compute the temperatures at the element centers according to the traction calculation. Ignoring y-coordinates, considering one row of elements,

$$T_i \stackrel{\text{def}}{=} T(x_i). \tag{12}$$

Regarding the heat input, the authors chose the first interpretation for the slip, where the slip values are also approximated at the element centers. This choice avoids the awkward averaging of values of two adjacent cell faces, whereas the same order of accuracy is expected from both approximations.

$$s_{a,i} = V \cdot \|\vec{s}(x_i)\| \,. \tag{13}$$

Note that $\vec{s}$ is the relative slip (dimensionless) whereas the absolute slip is s_a (mm/s).

The input power density at element i is then calculated as

$$\dot{q}_i \stackrel{\text{def}}{=} \dot{q}_{friction}(x_i) = \|\vec{p}_{\tau i}\| \cdot s_{ai} = \mu p_{ni} \cdot s_{ai} \,, \dot{q}_{wi} = \varepsilon \dot{q}_i \,, \dot{q}_{ri} = (1-\varepsilon_w)\dot{q}_i \,. \tag{14}$$

Using CONTACT's unit convention mm-kg-N-s, the unit of $\dot{q}_i$ is milli-Watt per millimeter squared, mW/mm^2.

3.1.6 Integration of the Heat Input

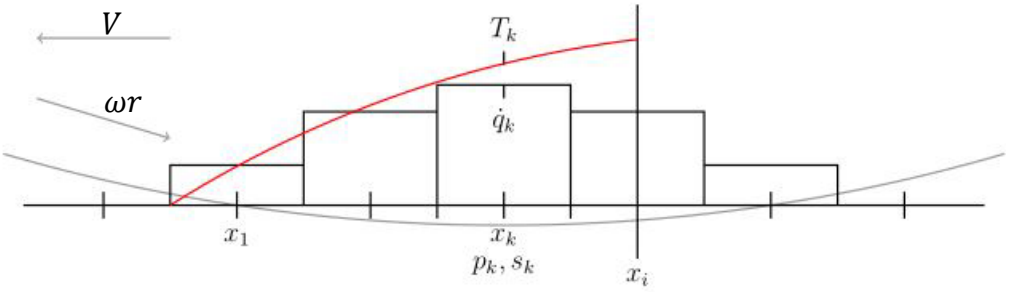

Figure 19. Calculation of temperature due to heat input when rolling to the left ("CHI= 180°") with leading edge at $x_{1/2}$. The bars represent the heat input $\dot{q}(x)$ and the red line represents the temperature increase.

The conversion from heat input to temperature follows Equation 11. The heat input is treated as a piecewise constant function with value $\dot{q}_k$ throughout element k.

$$\dot{q}_{w(x)} = \sum_k \dot{q}_k \, 1_k \, (x) \tag{15}$$

Here $1_k(x)$ is the indicator function that is 1 if x lies in element k and is zero otherwise. This permits writing the integral in Equation 11 as a sum of separate integrals per element k. Evaluating the temperature at position x_i for rolling to the left according to Figure 19:

$$T_w(0, x_i) = \frac{1}{\beta_w} \frac{1}{\sqrt{\pi V}} \left(\sum_{k<i} \left\{ \dot{q}_{wk} \int_{x_{k-1/2}}^{x_{k+1/2}} \frac{1}{\sqrt{x_i - x'}} \, dx' \right\} + \dot{q}_{wi} \int_{x_{i-1/2}}^{x_i} \frac{1}{\sqrt{x_i - x'}} \, dx' \right) \tag{16}$$

Rolling to the right is computed analogously.

The summation concerns the elements k from the leading edge up to element I. Because the temperature is calculated at the center of element I, integration continues up to x_i. The integrals over elements k yield:

$$\int_{x_{k-1/2}}^{x_{k+1/2}} \frac{1}{\sqrt{|x_i - x'|}} \, dx' = 2\sqrt{\left|x_i - x_{k-1/2}\right|} - 2\sqrt{\left|x_i - x_{k+\frac{1}{2}}\right|} \,, \tag{17}$$

The integrals over element i yield:

$$\int_{x_{i-1/2}}^{x_i} \frac{1}{\sqrt{|x_i - x'|}} \, dx' = \int_{x_i}^{x_{i+1/2}} \frac{1}{\sqrt{x' - x_i}} = 2\sqrt{\delta x/2} \,. \tag{18}$$

3.2 Friction Dependent on Temperature

A literature survey was conducted on the temperature dependence of the COF. This survey revealed a large diversity in findings, depending on the situations that are considered: low or high-speed sliding, for metallic or non-metallic materials, in a vacuum, air, or other gaseous atmospheres, at room or elevated ambient temperatures.

An important role appears to be played by the oxidation of metallic surfaces:

> If the surfaces are completely deduced of surface films by heating to evaporation in a high vacuum, the term "coefficient of friction" ceases to have any meaning, since the sliders seize together, even at room temperature (Bowden & Young, 1951).

After preliminary outgassing at high temperatures ($\geq 600°C$ or higher), the friction measured at room temperature reached indefinitely high values (≥ 4), "apparently limited only by secondary causes such as the geometry of the arrangement" (Bowden & Young, 1956).

Reporting on low-speed reciprocating sliding, Stott argues:

> …two competitive processes occur during sliding: breakdown of the layers, resulting in formation of further debris particles, and consolidation of the layers by further sintering/cold welding of the particles (Stott, 2002).

In this case, the ambient temperature affects the rate of sintering, and the rate of oxidation. At higher ambient temperatures, a hard "glaze layer" may be established on the surfaces, reducing friction and wear. Pearson and others found the same for a high strength steel in a fretting configuration, with COF decreasing continuously from $\mu = 0.78$ to 0.46 between $24°C$ and $450°C$ (Pearson, et al., 2013). Velkavrh et al. (2016), on the other hand, reported increasing friction at elevated temperatures in air (from $\mu = 1.0$ at $20°C$ to 1.4 at $200°C$) and other atmospheres. This may be attributed to the different contact parameters, such as the maximum Hertzian contact pressure, preventing the formation of a stable layer.

There are further effects present at high-speed sliding, where frictional heating may raise the surface temperature significantly above the ambient temperature.

> When two surfaces slide together, most of the work done against friction is turned into heat. The resulting rise in temperature may modify the mechanical and metallurgical properties of the sliding surfaces, and it may make them oxidize or even melt (Lim & Ashby, 1987).

At sliding velocities where this temperature rise is significant ($v > 1$ m/s; Lim, et al., 1989), the COF μ for unlubricated steel on steel contacts decreases with increasing v, as shown in Figure 13.

Frictional weakening at higher sliding velocities has been considered further by Molinari et al. (1999), and in the geophysics community (Rice, 2006), as a process active during earthquake slip. The latter cases are relevant to the current investigation because of the feedback considered between friction and slip, using the concepts of rate and state dependent friction (Putelat, et al., 2011; Singh & Singh, 2016).

Other papers report on friction increasing with increasing temperature. These situations are different from those in railways: using low melting materials as high-temperature lubricants (Rabinowicz & Imai, 1963), modeling glass molding (Mosaddegh, et al., 2011), and clutches in vehicle drive systems (Chaikittiratana, et al., 2012). A possible mechanism is the softening of the material, increasing the number of asperity contacts (Chaikittiratana, et al., 2012).

Tomberger et al. (2011) presented a model for wheel-rail contact including the effect of temperature on the COF, a "rather heuristic approach was chosen, […]: the failure stress is assumed proportional to the bulk material yield stress σ_y."

The yield stress reduces with temperature nonlinearly, as obtained from measurements from Voestalpine (Jöller, 1992).

Conclusions from this survey are as follows:

- Due to the thin layer for which temperatures are elevated, the reduced elastic modulus will not affect the contact problem directly.
- The main feedback of temperature on the contact problem is sought in (described as) a reduced COF.
- The physical mechanism responsible for the reduced COF may be the reduced elastic modulus and melting at the asperities in the true contact zone or may else come from alteration of the material structure (oxide formation) of the surface layer.

Given the large variation and uncertainty of the influence of temperature on the COF, the research team decided to approach this in a simplified way. A piece-wise linear relationship is chosen for μ as a function of T. In resemblance with the existing mechanism for velocity-dependent friction in CONTACT, this is formulated as

$$\mu(T_{srf}) = \begin{cases} \mu_{ref} & T_{srf} \le T_{ref} \\ \mu_{ref} + \Delta\mu_{heat}\dfrac{T_{srf} - T_{ref}}{\Delta T_{heat}} & T_{ref} \le T_{srf} \le T_{kin}, \quad T_{kin} = T_{ref} + \Delta T_{heat} \\ \mu_{kin} & T_{srf} \ge T_{kin} \quad \mu_{kin} = \mu_{ref} + \Delta\mu_{heat} \end{cases} \tag{19}$$

Here, T_{srf} is the average surface temperature in degrees Celsius, T_{ref} is the lower temperature at which μ starts changing, T_{kin} is the upper temperature at which μ stops changing, μ_{kin} is the ultimate value for μ at large sliding velocity, and $\Delta\mu_{heat}$ is the temperature dependent part of μ.

Equation 19 is illustrated in Figure 20. It allows for gradual transitions, for instance, using $T_{ref} = 0°C$ and $\Delta T_{heat} = 800°C$, as well as sharp transitions at any given temperature, e.g., $T_{ref} = 400°C$, $\Delta T_{heat} = 100°C$. The unit $°C$ is used for convenience but could be replaced by K. Positive values for $\Delta\mu_{heat}$ may be used, to explore the effects of friction increasing with temperature.

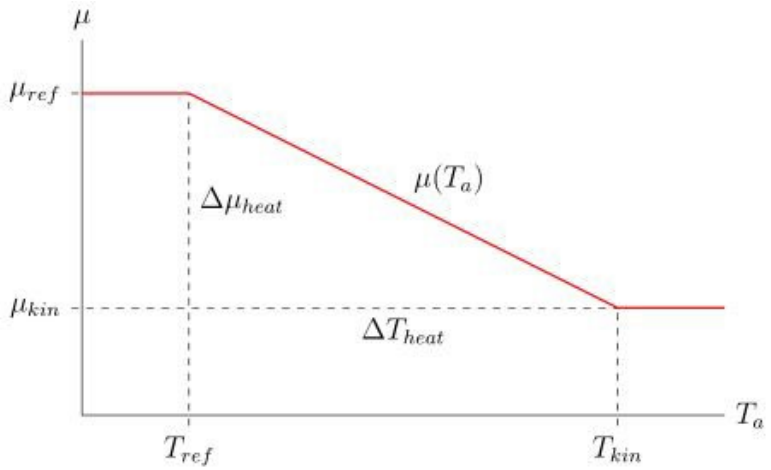

Figure 20. Visual representation of the COF μ as a function of temperature; in this case $\Delta\mu_{heat}$ is negative, resulting in a decreasing COF.

3.3 Results Regarding the Temperature Calculation

The following paragraphs present simulation results obtained with the new capabilities implemented in CONTACT: (1) surface temperatures for Ertz's test case with full sliding, (2) subsurface temperatures, (3) the effect of temperatures on the COF, and (4) the effect of temperature dependent friction on the creep force behavior.

3.3.1 Ertz's Testcase with Full Sliding

Table 1. Parameter values used in testing CONTACT's temperature calculation (the same used by Ertz & Knothe, 2002)

Parameter	Symbol	Value	Unit
Semi-axis of the contact ellipse In rolling direction In lateral direction	 a b	 5.88 10.54	 mm mm
Specific heat capacity	c_p	450	J/kg K
Normal force (wheel load)	F_n	100,000	N
Vehicle speed	V	30	m/s
Sliding percentage	ξ	0.03333	-
Thermal conductivity	λ	$50 \cdot 10^3$	W/K mm
Coefficient of friction	μ	0.3	-
Density	ρ	$7.85 \cdot 10^{-6}$	kg/mm^3

The calculation of surface temperatures is tested using the scenarios presented by Ertz and Knothe (2002), with the parameters as specified in Table 1.

Figure 21's left graph shows the results for frictional heating for a case with rolling and sliding at large creepage, with equal initial temperatures for the wheel and the rail. Particles enter the contact area at $x = -1$ and leave contact at $x = 1$. After that, heat diffuses away from the surface by which the surface temperature tends to the background temperature. Figure 21 (right) shows the results for heat conduction alone, using a case with rolling without creepage (or frictionless with $\mu = 0$) with a background temperature $T = 150°C$ for the wheel. These figures agree with Ertz and Knothe's Figures 3 and 6 (2002). The combined solution for frictional heating and heat conduction is shown in Figure 22.

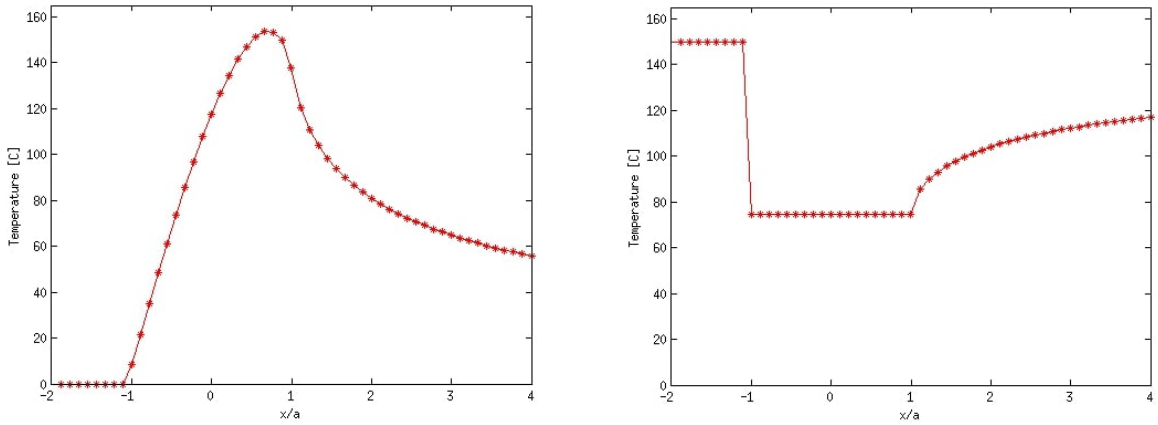

Figure 21. Left: temperature profile due to frictional heating alone (i.e., with equal wheel and rail background temperatures, full sliding, $s_a = 1$ m/s), Right: temperature profile of the wheel for a situation with heat conduction alone with $s_a = 0$ and $T_{w0} = 150°C$

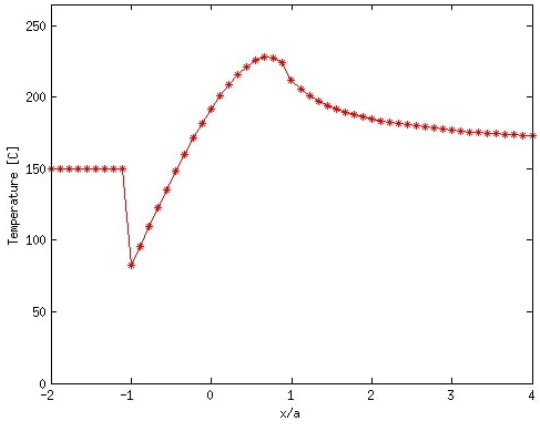

Figure 22. Temperature profile for the wheel for the combined problem with frictional heat input (full sliding, $s_a = 1$ m/s) and heat conduction/rail chill

3.3.2 Subsurface Temperatures

If the initial temperature of the wheel is increased from 150 to $240°C$, an odd fluctuation is found at the trailing end of the contact patch, as shown in Figure 23. This seemed to be an error in the discretization at first, or a mismatch of the different regimes used at the boundary. However, the peak turns into a smooth profile when using a severe grid refinement, as shown in Figure 23 (right). The finite difference method was implemented to investigate the temperature profile just after contact is broken ($t > 1, z > 0$). This solution showed the same behaviour as the code in CONTACT for the surface temperature.

The reason for the trailing edge peak is found in the temperatures in the subsurface (Figure 24). The figure shows that the maximal temperature may be found at a value $z > 0$, inside the wheel. This may happen when $\dot{q}_{friction}$ decreases towards the trailing end of the contact area before contact is broken. Contact is lost at $t = 40{,}000$ in this simulation. The local maximum is then found to move rapidly to the surface due to convection. This results in a slight rise of the surface temperature before the effect of heat moving down into the bulk of the wheel becomes dominating.

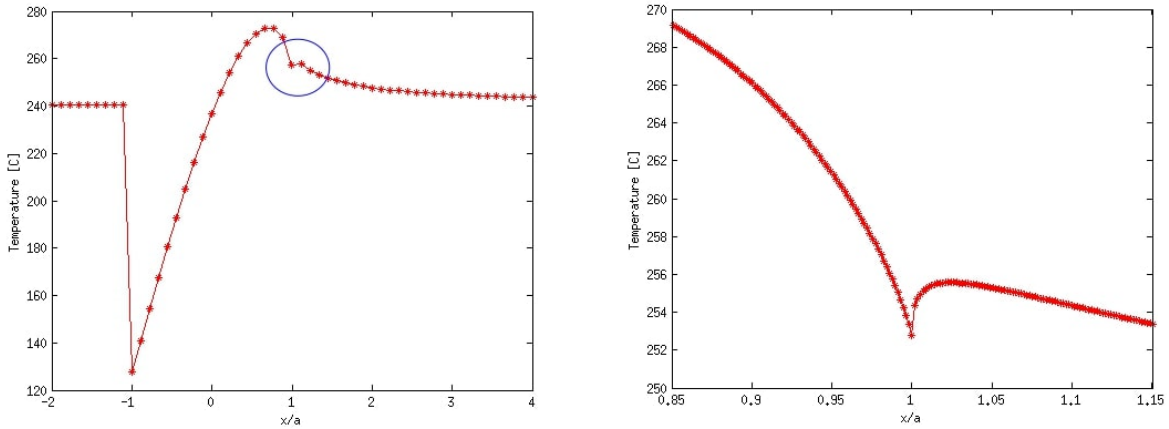

Figure 23. Temperature profile, using a higher initial wheel temperature than Figure 22; there is a seemingly odd peak at the trailing end of the contact patch, shown zoomed in on the right.

3.3.3 Friction Dependent on Surface Temperature

Without considering the influence of temperature on friction, Ertz's testcase has an increase of the surface temperatures by $167°C$. The case is computed again in two variants:

- Decreasing friction: $\mu_{ref} = 0.30,\ \Delta\mu_{heat} = -0.18,\ \Delta T_{heat} = 400°C$
- Increasing friction: $\mu_{ref} = 0.30,\ \Delta\mu_{heat} = \ 0.18,\ \Delta T_{heat} = 400°C$

The results are shown in Figure 25. With decreasing friction, the tractions p_x are reduced, decreasing the heat input into the system. The maximum temperature reduces to $137.5°C$, at which $\mu = 0.30 \ - \ 0.18 \cdot 137.5/400 \ = 0.238$. With increasing friction, there is more heat input into the system, increasing the maximum temperature to $209°C$ and $\mu = 0.394$.

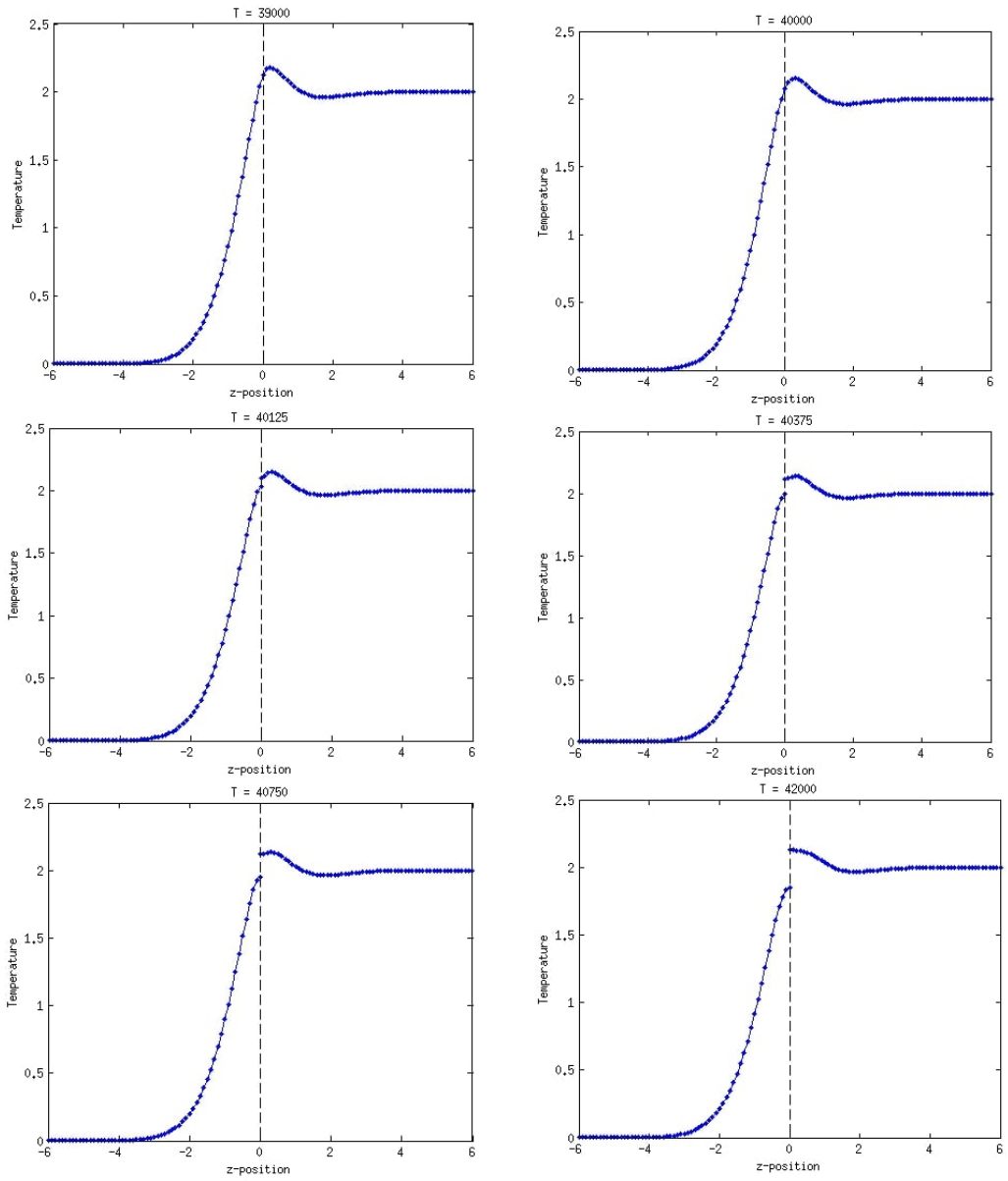

Figure 24. Successive time-instances for temperature distribution at one position $[x, y]$, left: rail ($z \leq 0$), right: wheel ($z \geq 0$). Contact is broken at time-instance $T = 40,000$.

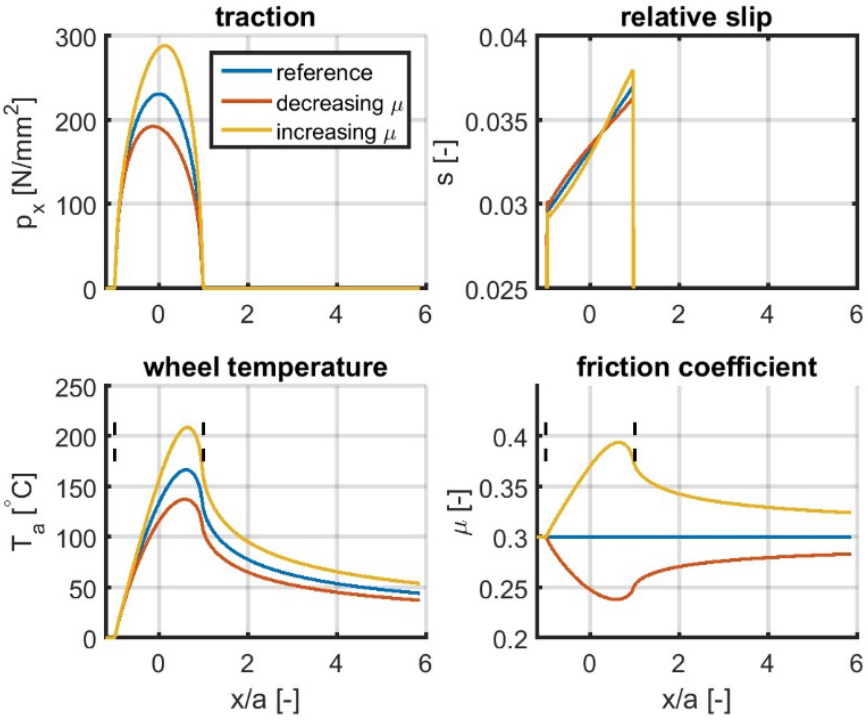

Figure 25. Simulation results for Ertz's test case, full sliding at $s = 1$ m/s, with temperature dependence $\Delta\mu_{heat} = \pm 0.18$ over $\Delta T_{heat} = 400°C$

3.3.4 Effect on the Creep Force Behavior

CONTACT's `tractcurv` example is used to explore the effects of temperature on creep-force behavior. This concerns the EuroSprinter test case (Vollebregt, 2014; 2019a), as shown in Figure 16. Thirty cases are computed with creepage increasing from 0.1 to 25 percent. Using a constant COF $\mu = 0.33$, this yields surface temperatures up to $700°C$.

The test is repeated three times with different settings for the temperature dependence. The results are shown in Figure 26. The results show only marginal effects of temperature dependence on the initial part of the creep curve. Once full sliding is reached, at a creepage of about 0.35 percent, there is continued increasing of the creep force when $\Delta\mu_{heat} > 0$ or falling friction when $\Delta\mu_{heat} < 0$. The rate at which falling friction occurs depends on the slope of the temperature dependence, $\Delta\mu/\Delta T$. The steeper slope obtained for $\Delta T_{heat} = 400°C$ corresponds roughly to the falling friction effect as observed in the experimental measurements.

The maximum temperatures obtained in each test are shown in Figure 26 (right). This shows a linear dependence for the original model, without feedback of temperature on the COF, as expected from the heat flux proportional to $\xi\, V F_x$, with $F_x = \mu F_n$. With interaction, the maximum temperatures exhibit a roughly quadratic dependence on the creepage ξ. Slight deviations from this quadratic form arise due to the shape of the traction bound μp_n changing with ξ, shifting the location of the maximum temperature slightly.

3.4 Conclusions Regarding Surface Temperature

This section discussed the calculation of surface temperatures in CONTACT. A literature review was conducted to find the relevant aspects and modeling approaches, identifying the paper by Ertz and Knothe as the starting point for the work. The mathematical model was reviewed thoroughly, improved slightly, and implemented for steady rolling scenarios. Situations of transient rolling and subsurface temperatures were also explored using the finite difference method to check the model's results. These results agree with the literature.

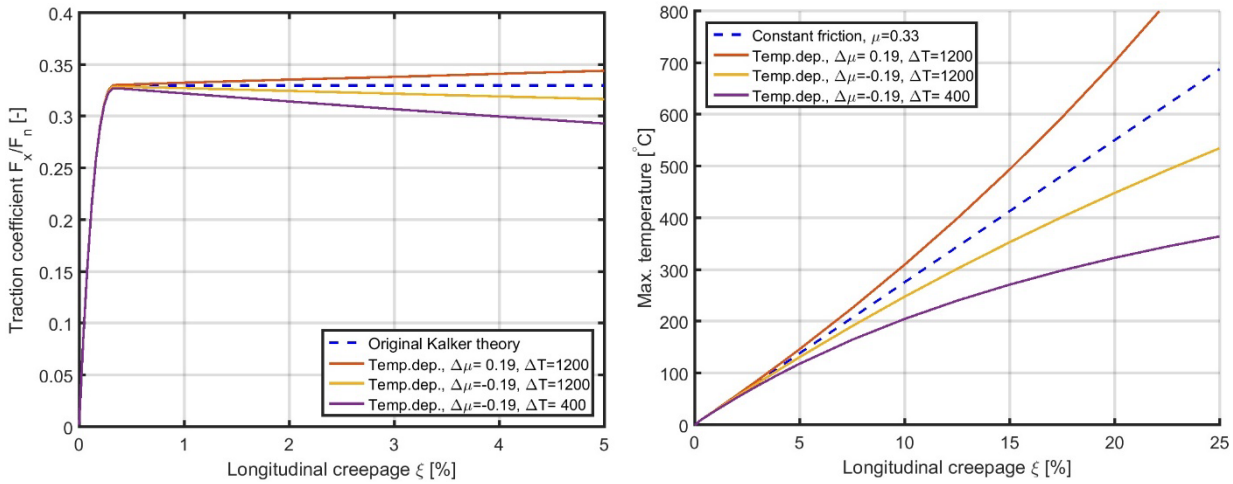

Figure 26. Left: creep force curves for the EuroSprinter test case (Vollebregt, 2014; 2019a), with COF dependent on surface temperature *T*, right: maximum surface temperature in each test

Next, the effect of surface temperature on the COF was also considered. A literature review was conducted to find how temperature affects friction, showing the importance of oxidation processes and (local) melting. No consistent data could be found on the strength of these effects. A piece-wise linear formula was chosen for the temperature dependence, that allows for exploring the significance of the input parameters. The mechanism was implemented in CONTACT, and test results illustrating the effects were discussed. In the current model, temperature dependence has little influence on the initial slope of creep force curves. The falling part of measured locomotive creep-force curves appears to be captured well at reasonable values for the input parameters.

4. Effects of Solid Third Body Layers

Much of the literature discusses the effects of solid interfacial layers in explaining the observed patterns in the creep versus creep force (e.g., Hobbs, 1967; Beagley, et al.,, 1975b; Kalker, 1978; Logston & Itami, 1980; Godet, 1984; Berthier, 1990; Kalker, 1992; Hou, et al.,, 1997; Polach, 2005). One primary effect of these layers is to reduce the Kalker coefficients, i.e., the initial response of creep forces to increasing creepage. A second observed effect in measured creep forces is slower transition between the linear and saturated regimes (Polach, 2005; Six, et al., 2015). A third effect concerns the change of creep forces at large creepage with increasing or falling characteristics.

A phenomenological, mathematical description of three body contacts was presented by Kalker (1992), focusing on the initial slope reduction. Kalker proposed a mental model of wear debris which are sometimes held together by a cementing substance, much weaker and more pliable than the primary bodies. The elements of the third body are compressed and shifted in a rolling and sliding motion, flattened by elasto-plastic deformation. However, the formulas used do not represent this mental model fully but describe a layer with elastic deformation. Mostly similar formulas were derived independently and introduced in Extended CONTACT (Vollebregt, 2014).

Hou and others (1997) measured the shear strength of different interfacial layers using high pressure torsion testing. This revealed different characteristics for different compounds, consisting of an initial rapid increase, followed by a slower increase, or settling at constant or decreasing values. A rheological model was proposed for relating shear stress and shear strain in the layer, modelling the initial increase as elastic deformation. The following parts are attributed to plastic deformation or shear failure of the layers.

In the following section, the research team presents an extension of CONTACT for plastic deformation of a solid interfacial layer or in a surface layer of the primary bodies. Secondly, the mental model addresses how interfacial layers may affect the initial slope of creep versus creep force curves.

4.1 Plasticity in Wheel-Rail Contact Situations

Plastic deformation is the permanent deformation of a body that lasts after the stresses that caused the deformation are gone. How this occurs and influences further deformation depends on the type of material. Two clear cases can be separated, concerning brittle and ductile materials. Brittle materials have a relatively short range in which plastic deformation occurs, after which the material breaks or tears. Ductile materials go through different stages, starting with elastic deformation, after which plastic deformation occurs and the material hardens, until it gets softer again, before eventually breaking. Steel exhibits this characteristic; see the typical stress-strain curve for steel in Figure 27.

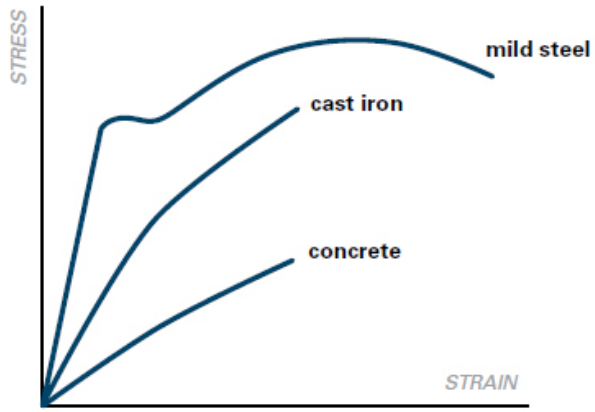

Figure 27. Stress-strain curves for concrete, cast iron (brittle), and steel (ductile). The first (linear) part of the steel curve shows the elastic part; the kink and part thereafter concern plastic deformation (NPCA, precast.org).

Stress-strain curves are typically obtained from uniaxial tensile testing. A workpiece (specimen) is placed in a testing machine and slowly extended until it fractures. During this process, the elongation of the specimen is recorded against the applied force. The "apparent strain" (engineering strain) is defined as the elongation over the initial length:

$$\varepsilon = \frac{\Delta L}{L_0} \tag{20}$$

The "apparent stress" (engineering stress) is computed similarly using the initial (nominal) cross-section A:

$$\sigma = \frac{F_n}{A} \tag{21}$$

The actual strain and actual stress are obtained by replacing the initial length and area with the actual values.

Steel has an elastic limit on stress, up to which point all force is shouldered by elastic deformation. If the stress is increased beyond this point, further stresses will plasticly deform the material. This usually results in work hardening of the material. This hardening determines the shape of the curve in the plastic regime, which depends on the type of steel being considered.

4.1.1 Global Versus Local Plasticity

Severe plastic deformation may be found within wheel-rail contacts, especially in a sub-surface layer of a few tens of microns thickness (Kapoor, et al., 2002). Two different forms of plasticity may then be distinguished (Six, et al., 2016a; 2016b):

1. Global plasticity affects the shape of wheel and rail profiles.
2. Local plasticity is confined to a microscopic layer without affecting the profiles.

Global plasticity occurs, for instance, when new rails are put into service. In the initial wheel passes, highly localized stresses may occur due to the mismatch of the wheel and rail profiles. This will push material down and sideways and shape the rail profile into a better matching form, lowering the maximum stresses. The material is work-hardened at the same time, such that this

kind of plastic deformation will reduce after a limited number of wheel passes (Six, et al., 2016a).

Global plasticity may also occur in switches and crossings, due to repeated pounding of the wheels on the rails. This kind of loading may eventually lead to fatigue damage. Lipping is another manifestation of plasticity, during which the materially is gradually sheared along the rail towards the track center, forming a lip at the bottom of the rail head. This form of plasticity occurs due to large lateral forces in curves.

4.1.2 Local, Tribological Plasticity

While plasticity at the global scale may alter the creep forces at some locations or in some time instances, it cannot be a major factor for all wheel-rail contact situations. This form of plasticity typically reduces after the materials have run in, such that a continuing effect occurs only in a limited number of scenarios where certain conditions are met.

Continued plastic deformation is possible at the local, tribological scale at the rail surface. The surface layer wears away slowly, such that fresh material is repeatedly exposed to plastic deformation. However, third body layers of various composition may occur, acting as solid lubricant layers, that can be molded repeatedly. These kinds of local plastic deformation provide compliance between the two surfaces, accommodating creepage at the expense of resisting shear tractions.

Experiments were performed at NRC Canada (Hou, et al., 1997) focused on the shearing of surface layers of various materials, as shown in Figure 28, left. Different characteristics were found for clay, magnetite, and sand: clay required more shear stress for increasing shear deformation; for magnetite, the shear stress leveled off at a certain shear deformation, and for sand, the shear stress reduced at increased shear strain. These characteristics are captured in a schematized way in Figure 28 (right).

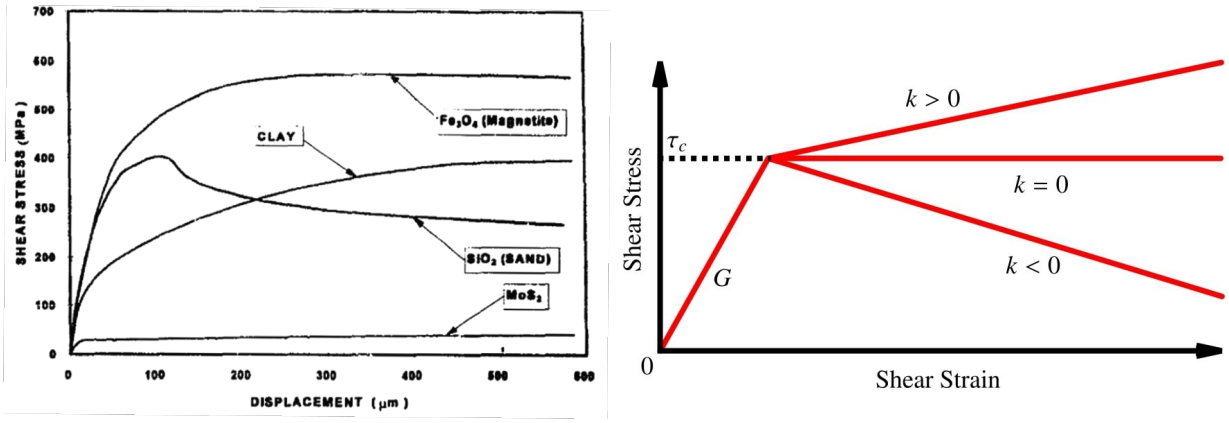

Figure 28. Left: measured shear stress curves for several compounds, right: corresponding model for an interfacial layer. The model relates shear stress τ to shear strain γ using elastic (G) and plastic (k) regimes, with strain-hardening ($k > 0$), elastic-perfectly plastic ($k = 0$) and strain-weakening characteristics ($k < 0$) (Hou, Kalousek, & Magel, 1997).

4.2 Literature Review

The literature on modeling and computation of plastic effects is robust, and includes works that focus on analytic approaches, using eigenstrains, inclusions, etc. (Chiu, 1978; Ben-Zion, 1990; Leroux, et al., 2010; Zhou, et al., 2011). While these models seem to focus on idealized forms of plasticity (i.e., perfectly plastic instead of nonlinear work hardening) and on global plasticity, the resulting algorithms are computationally demanding. Therefore, these algorithms are of lesser concern to the present work.

Some of the literature was concerned with the extension of Kalker's active set algorithms, introducing a "plastic set" for points where plasticity occurs (Willner & Hauer, 2012; Hauer, 2014; Beyer, et al., 2015). This research considers global plasticity related to the contact pressures instead of shear stresses. Sebès and colleagues (2012) presented a heuristic method with similar aims, extending the semi-Hertzian STRIPES model.

Meierhofer and others (2014) presented a model to describe the influence of plasticity on the traction characteristic. They use Hertzian theory for the normal pressures in combination with a 2D approach for the rolling contact of an infinite cylinder. The tangential shear stress is approximated using a series of polynomial terms, integrated analytically over the contact strip $x \in [-a, a]$. Plastic deformation is confined to a third-body layer as shown in Figure 29, using Hou's characteristic in Figure 28. In addition to model development, twin-disc experiments were performed to validate the results.

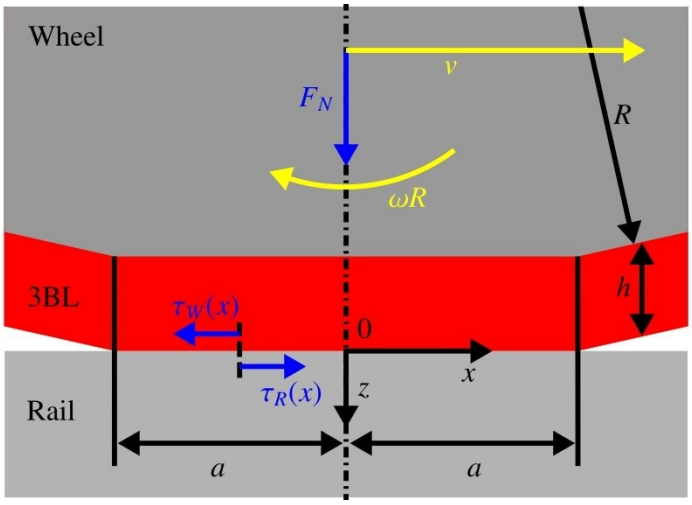

Figure 29. Sketch of the geometry of the third body layer with plasticity confined to a thin layer and computed using a series expansion approach (Meierhofer, et al., 2014)

The concepts introduced in Meierhofer's work seem promising yet may need refinement for implementation in CONTACT. First, the deformation in the third body layer is described as a spring with reduced stiffness $m(x)$ in the plastic regime:

$$\frac{\partial u_{3bl}}{\partial x} = -\frac{h}{m(x)}\frac{\partial \tau(x)}{\partial x}, \text{ with } \begin{cases} m(x) = G & \text{where } |\tau(x)| \le \tau_c \\ m(x) = k & \text{where } |\tau(x)| > \tau_c \end{cases} \tag{22}$$

This seems inappropriate because energy will be stored in the spring instead of being dissipated. Secondly, using a series of polynomial terms, the model is limited to 2D cases, whereas CONTACT requires an extension to 3D situations.

4.3 Modeling of Plastic Material Behavior

This work considers local plasticity in the wheel and rail surfaces or in a third body layer between them. The main goal is to capture the effect of this on the creep force characteristic, by extension of CONTACT's half-space approach. The model is developed for 2D (line contacts) and 3D situations (point contacts).

4.3.1 Basic Normal Model

In elasticity, the normal problem is solved by stating $e_n = h_n + u_n$. Different authors add a term to account for plastic deformation:

$$\text{Positive gap:} \quad e_n = h_n + u_n^{el} + u_n^{pl} \geq 0\,, \tag{23}$$

$$\text{Compressive pressures:} \quad p_n \geq 0\,, \tag{24}$$

$$\text{Plastic limit:} \quad p_n \leq p_{pl}\,. \tag{25}$$

The elastic displacement is then calculated through the known means from elastic theory: $u_n^{el} = \int A \cdot p_n$. The pressures must still be positive, $p_n \geq 0$. Additionally, the pressures must stay under a plastic limit $p_n \leq p_{pl}$ during the calculation of u_n. This limit may depend on the prior plastic deformation (work hardening) and may therefore be space-varying. The excess traction will be absorbed in further plastic deformation of the material according to a flow rule: $\delta u_n^{pl} = f(p_n - p_{pl})$ for $p_n > p_{pl}$ and some function f. Beyer and others state:

> Finally, for the sake of volume conservation, the volume reduced due to δu_n^{pl} is added evenly on the element patches that are not in contact based on the findings of Pullen & Williamson (Beyer, et al., 2015).

4.3.2 Tangential Plasticity in a Near-Surface Layer

A model will be constructed for tangential plastic deformation analogous to the basic normal model of Equations 23 to 25. Figure 30 through Figure 34 outline how this may work, accounting for an increasing amount of rigid displacement, $w = \int \xi\, V\, dt$.

Figure 30. Situation 1: A wheel particle is displaced with respect to the rail by creepage. Initially, this rigid shift *w* is so low that it can be accomodated easily by elastic displacement.

Figure 31. Situation 2: Creep accumulates over time, increasing the rigid shift w, until it is checked exactly by an elastic displacement, for which the required traction τ reaches the yield point τ_c.

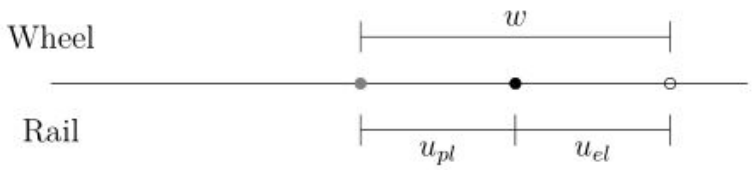

Figure 32. Situation 3: The creep is slightly larger than in Figure 31. Because there is no longer elastic deformation beyond the yield point, additional creeping is compensated for through plastic deformation.

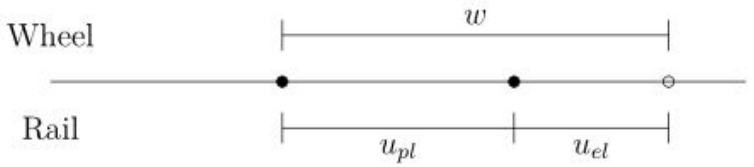

Figure 33. Situation 4: The creep is chosen such that the traction due to elastic deformation and plastic deformation adds up to exactly the traction bound: $g = \mu p_n$.

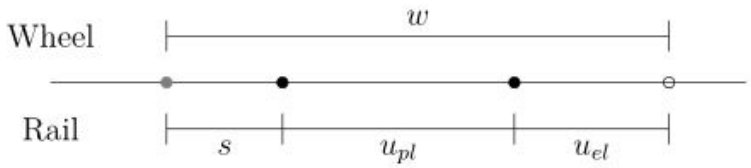

Figure 34. Situation 5: With creepage ξ requiring tractions larger than the traction bound g, there will be actual slip s next to elastic and plastic deformation.

4.3.3 Adaptation of Hou's Model

The basic model in Figure 28 (right) must be transformed before its introduction into CONTACT. This is because the figure gives the stresses τ as function of the displacements, while CONTACT requires the displacements u to be expressed as functions of the applied loads. This relationship changes form between loading and unloading, as shown in Figure 35 (left).

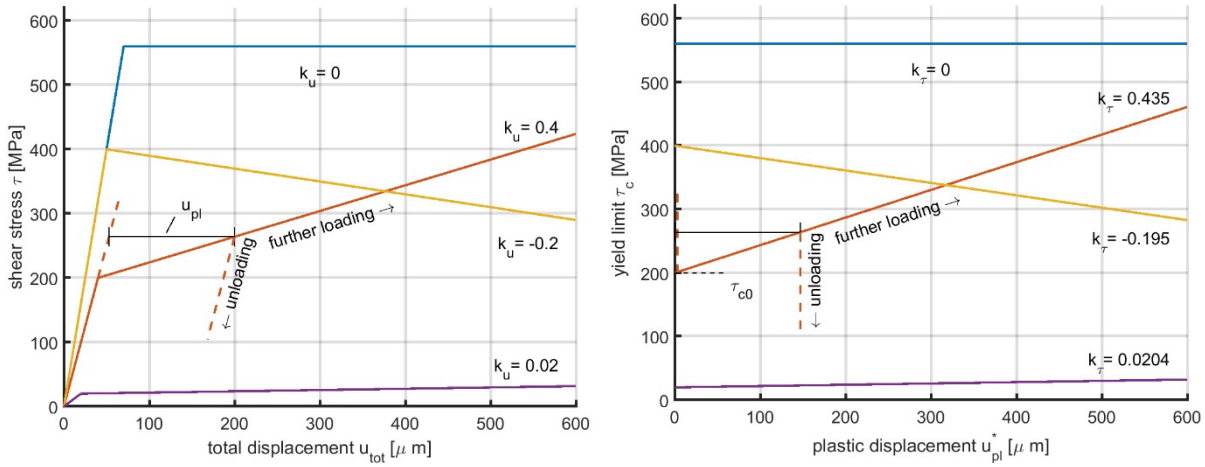

Figure 35. Left: piece-wise linear approximation of the stress-strain relations of Figure 28 (left), right: work hardening for the materials considered, relating the yield limit τ_c to the accumulated plastic deformation

The characteristics measured by Hou et al. as shown in Figure 28 (left), concern unidirectional loading. The displacement reported is the total displacement, u_{tot}, comprising elastic and plastic parts, $u_{tot} = u_{el} + u_{pl}$. In Figure 35, these curves are schematized using piece-wise linear approximation, with slope G for the initial, elastic part, with plasticity appearing when the initial yield stress is reached, $\tau = \tau_{c0}$, changing the slope to $k = k_u$.

The solid lines in Figure 35 (left), are problematic when time-varying loads are considered because they allow u_{pl} to decrease over time, undoing plastic deformation, if the applied load is taken away. This then feeds energy back into the system that should have been dissipated away. This is circumvented by deviating from the solid lines upon unloading. Once the stresses have been increased into the plastic regime, only the elastic displacement will be diminished if the load is removed. Plasticity then acts as a unilateral constraint, with different stiffnesses for further loading versus unloading.

Figure 35 (right) transforms the characteristics of Figure 35 (left) into a suitable form for CONTACT. This shows the evolution of the yield limit τ_c with increasing amounts of plastic deformation. This describes the work hardening observed for the interfacial layers considered by Hou: the stresses τ needed to get increasing plastification. The slopes of these curves are denoted k_τ:

$$\text{Increasing } u_{tot}: \ \delta\tau = k_u \cdot \delta u_{tot} = k_u \cdot (\delta u_{el} + \delta u_{pl}) \tag{26}$$

$$\delta u_{el} = \frac{\delta\tau}{G} \ \rightarrow \ \delta\tau = k_\tau \cdot \delta u_{pl}\,, k_\tau = \frac{G \cdot k_u}{G - k_u}. \tag{27}$$

It is unknown how the curves for τ_c should be generalized in 3D situations. Different kinds of material behavior can be envisaged for situations where the direction of plastic deformation changes in time:

- For some materials, plasticity may be understood as stretching grains or fibers in the direction of plastic deformation, such that the material is not work-hardened in the

perpendicular direction. This then yields anisotropic material behavior. In principle, the work hardening could be undone by plastic deformation in the opposite direction.

- For other materials, plasticity may be understood as grain refinement or breaking particles into smaller pieces, which may continue to occur if the direction of plasticity is changed or reversed.

These different types of material behavior may be captured by replacing the actual plastic displacement u_{pl} in Figure 35 (right) by an accumulated plastic displacement u_{pl}^*. For plasticity that can be undone, this can be $u_{pl}^* = \|\vec{u}_{pl}\|$, ignoring anisotropic effects. In the alternative case, with continued work hardening or degradation, a formula like $u_{pl}^* = \int_t \|\delta\vec{u}_{pl}\|$ may be used, summing up all prior plastic displacement increments without accounting for their directions.

4.3.4 Tangential Model with Plastic Deformation

After heavy prototyping in MATLAB, the following continuous model emerged:

$$\text{Total displacements:} \quad \vec{u} = \vec{u}_{tot} = \vec{u}_{el} + \vec{u}_{pl} \tag{28}$$

$$\text{Slip equation:} \quad \vec{s}_{rel} = \vec{w}_{rel} + (\dot{\vec{u}}_{el} + \dot{\vec{u}}_{pl})/V \tag{29}$$

$$\text{Elastic displacements:} \quad \vec{u}_{el} = \iint_C \boldsymbol{A}(\vec{x},\vec{y})\,\vec{p}(\vec{y})\,d\vec{y} + \frac{h^{(3)}}{G^{(3)}}\vec{p} \tag{30}$$

$$\text{In exterior } E\text{:} \quad \|\vec{p}\| = 0, \qquad \vec{s} \text{ free}, \qquad \dot{\vec{u}}_{pl} = \vec{0}, \tag{31}$$

$$\text{In adhesion } H\text{:} \quad \|\vec{p}\| \le \min(g,\tau_c)\,, \vec{s} = \vec{0}, \qquad \dot{\vec{u}}_{pl} = \vec{0}, \tag{32}$$

$$\text{In slip } S\text{:} \quad \|\vec{p}\| = g \le \tau_c, \qquad \vec{s} \parallel \vec{p}, \qquad \dot{\vec{u}}_{pl} = \vec{0}, \tag{33}$$

$$\text{In plasticity } P\text{:} \quad \|\vec{p}\| = \tau_c < g, \qquad \vec{s} = \vec{0}, \qquad \dot{\vec{u}}_{pl} \parallel \vec{p}, \tag{34}$$

$$\text{Tangential traction bound:} \quad g = \mu p_n\,, \tag{35}$$

$$\text{Actual tangential yield limit:} \quad \tau_c = \tau_{c0} + k_\tau\, u_{pl}^*\,, \tag{36}$$

$$\text{Accumulated plastic deformation:} \quad u_{pl}^* = \int_t \|\dot{\vec{u}}_{pl}\|\; dt\,, \tag{37}$$

$$\text{Or:} \quad u_{pl}^* = \|\vec{u}_{pl}\|\,. \tag{38}$$

Here $\dot{} = D/Dt$ stands for the material time derivative.

These equations extend Kalker's variational theory of rolling (Kalker, 1990), viz. Equations 29, 30, 31, 32, 33 and 35. The latter term in Equation 30 describes the elastic displacements $u_{el}^{(3)}$ in the third body layer introduced in Extended CONTACT (Vollebregt, 2014). Kalker's equations are regained with $h^{(3)} = 0$ if $\vec{u}_{pl} \equiv \vec{0}$, e.g., when $\tau_{c0} > \max(g)$. The extensions concern additional concepts for plastic deformation:

- The total deformation $\vec{u}_{tot}$ comprises a contribution $\vec{u}_{pl}$ concerning plastic deformation (Equation 28).

- Creepage introduces rigid slip $\vec{w}_{rel}$, a tendency of slipping of the contacting surfaces. This tendency is accommodated through increased elastic deformation $\vec{u}_{el}$, increased plasticity $\vec{u}_{pl}$, and actual slipping $\vec{s}_{rel}$ (Equation 29).
- The preferred mode is elastic deformation (Equation 32). Plasticity and slip occur only when/where the possible stress is exhausted. Which one occurs depends on the smaller of the traction bound g and actual yield point τ_c.
- Slip occurs when (where) the traction bound is reached (Coulomb friction), requiring that this is below the yield point (Equation 33): $\|\vec{s}\| > 0$ and $\|\vec{p}\| = \mu p_n \leq \tau_c$). The direction of slip precisely opposes the traction ($-\vec{p} \parallel \vec{s}$). This gives the smallest possible slip, satisfying a minimum principle.
- A similar reasoning applies to the plastic deformation (Equation 34). Where plastic deformation occurs, the tractions $\vec{p}$ are in the same direction as the plastic increment ($\vec{p} \parallel \delta\vec{u}_{pl}$). Note that $\vec{s}$ occurs on the left-hand side of Equation 29, whereas $\dot{\vec{u}}_{pl}$ occurs on the right side; therefore, the sign is different.
- The actual yield limit τ_c (Equation 36) describes the characteristics of Figure 28, using an initial yield stress τ_{c0} for fresh material, a material hardening parameter k_τ, and the accumulated plastic deformation u_{pl}^*.
- The accumulated plastic deformation u_{pl}^* measures the path length as shown in Equation 37.

It is possible to replace Equation 37 with 38. For Equation 37, materials become ever stronger ($k_\tau > 0$) or weaker ($k_\tau < 0$) with further plasticity, whereas the alternative implies that the strengthening or weakening can be undone by reversal of the plasticity direction. Which provides the best representation of the situation depends on the materials used.

The parameter k_τ may be obtained from measurements, using Hou's parameter $k = k_u$ (Equation 27). In principle, it is possible to use a generic function $\tau_c = f(u_{pl}^*)$ instead of a linear dependence, though this requires additional programming that has not yet been completed.

4.3.5 Discretization

Equations 28 through 34 are discretized using a rectangular potential contact area divided into $n = m_x \times m_y$ elements of size $\delta_x \times \delta_y$. The elements are numbered $I = 1 \cdots n$, with $\vec{x}_I$ representing the element center.

A time step is considered from previous time t' to current time t, with time step $\delta t = t - t'$.

The tractions $\vec{p}$ are approximated using a piecewise constant distribution, represented by the 2-vectors $\vec{p}_I = [p_{Ix}, p_{Iy}]^T$ for all elements I. The displacements, slip, traction bound, etc. are approximated at the element centers, e.g., $\vec{u}_{Iel}$ approximates $\vec{u}_{el}(\vec{x}_I)$.

This discretization leads to the following system of equations to be solved:

$$\vec{u}_{Iel} = \sum_J \boldsymbol{A}_{IJ}\, \vec{p}_J + L^{(3)}\vec{p}_I \tag{39}$$

$$g_I = \mu_I \, p_{In} \tag{40}$$

$$\delta\vec{u}_{Ipl} = \vec{u}_{Ipl} - \vec{u}'_{Ipl} \tag{41}$$

$$\delta u^*_{Ipl} = \left\| \delta\vec{u}_{Ipl} \right\| \tag{42}$$

$$\tau_{Ic} = \tau'_{Ic} + k_\tau \, \delta u^*_{Ipl} \tag{43}$$

$$\vec{s}_I = \vec{w}_I + \frac{\vec{u}_{Iel} - \vec{u}'_{Iel}}{V \, \delta t} + \frac{\delta\vec{u}_{Ipl}}{V \, \delta t} \tag{44}$$

I in exterior E: $\quad \|\vec{p}_I\| = 0, \qquad \vec{s}_I \; free, \qquad \delta\vec{u}_{Ipl} = \vec{0}, \tag{45}$

I in adhesion H: $\quad \|\vec{p}_I\| \leq \min(g_I, \tau_{Ic}) \, , \qquad \vec{s}_I = \vec{0}, \qquad \delta\vec{u}_{Ipl} = \vec{0}, \tag{46}$

I in slip S: $\quad \|\vec{p}_I\| = g_I \leq \tau_{Ic}, \qquad \vec{s}_I \parallel \vec{p}, \qquad \delta\vec{u}_{Ipl} = \vec{0}, \tag{47}$

I in plasticity P: $\quad \|\vec{p}_I\| = \tau_{Ic} < g_I, \qquad \vec{s}_I = \vec{0}, \qquad \delta\vec{u}_{Ipl} \parallel \vec{p}_I \, . \tag{48}$

Complications occur in this model due to the time evolution of g and τ_c. Note that g starts at zero, such that there may be slip in the first part of the contact. At some point, g may become larger than τ_c, upon which plastic deformation sets in ($S \rightarrow P$) if needed to accommodate $\vec{w}$. Later, g may fall below τ_c and slip may take over again ($P \rightarrow S$).

1. Transition from S to P:
   a. At the transition from S to P, the traction bound g'_I could be smaller and g_I just marginally larger than τ'_{Ic}. For sufficiently large k_τ and $\vec{w}$, plasticity would then, in a finite time step δt, increase the yield limit τ_{Ic} beyond g_I. This means that the equations have no solution: the element cannot be in S because τ_{Ic} would remain at $\tau'_{Ic} < g_I$, and cannot be in P either because $\tau_{Ic} = \tau'_{Ic} + k_\tau \delta u^*_{Ipl} > g_I$.

      In the continuous model, this situation would first have some slip, up to the point (time instance) where $g = \tau_c$, followed by slip and plastic deformation in the proper proportion such that g and τ_c remain equal.

   b. Theoretically, the equations may have multiple solutions when $k_\tau < 0$. This occurs when $\tau'_{Ic} > g_I$, whereas $\tau'_{Ic} + k_\tau \delta u^*_{Ipl} < g_I$. One solution is then with I in slip, $\delta u^*_{Ipl} = 0$ and $\tau_{Ic} > g_I$, the other has $I \in P$, $\delta u^*_{Ipl} > 0$, and $\tau_{Ic} < g_I$. In this case, the model cannot decide whether the rigid slip $\vec{w}$ should be accomodated as slip $\vec{s}$ or as plastic deformation $\delta\vec{u}_{pl}$. This complication does not exist in the continuous model, where the slip solution is selected since $g'_I < \tau'_{Ic}$.

2. Similar issues arise at the transition from P to S, at the trailing side of the contact.
   a. No solution exists if $\tau'_{Ic} < g_I$, whereas τ_{Ic} will increase above g_I if further plasticity occurs. The element then cannot be in S because this results in $\tau_{Ic} = \tau'_{Ic} < g_I$, and cannot be in P either because then $\tau_{Ic} > g_I$. This may happen if $k_\tau > 0$ and if τ'_{Ic} is marginally below g_I.
   b. Multiple solutions may exist if $k_\tau < 0$. If the element would stay in P the whole time, the yield limit could be decreased such that $\tau_{Ic} < g_I$, while $\tau'_{Ic} > g_I$ also

allows for slip instead of plasticity. In this case, the continuous model suggests that the plastic solution should be preferred.

Two extensions are made to the model of Equations 39 to 48 regarding these complications.

- First, the element is required not to change from S to P or vice versa if it is possible to stay where it was at the previous time. This eliminates the non-uniqueness of the solution.
- Second, the constraint $\delta\vec{u}_{Ipl} = 0$ of the slip regime is relaxed (Equation 47) where necessary to avoid over-constraining the problem. This may be considered to introduce a new regime S^* ($S \cap P$):

$$I \text{ in slip } S^* : \quad \|\vec{p}_I\| = g_I = \tau_{Ic}\,, \qquad \vec{s}_I \parallel \vec{p}_I, \qquad \delta\vec{u}_{pl} \parallel \vec{p}_I. \tag{49}$$

This regime is an extension of S, if $\tau'_{Ic} < g_I$ and if another regime would lead to $\|\vec{p}_I\| > g_I$.

4.3.6 Extension of the Gauss-Seidel Solvers

Equations 39 to 49 are solved using extended versions of the tangential solvers ConvexGS (Vollebregt, 1995) and SteadyGS (Vollebregt, 2010). These solvers are based on the Gauss-Seidel technique, repeatedly updating the tractions $\|\vec{p}_I\|$ per element $I = 1 \cdots n$ until convergence occurs. A main kernel in these solvers is a subroutine `elmtrc` that solves the problem for one element I, keeping the tractions $\|\vec{p}_J\|$ of all other elements J fixed at their current iterative values.

The behavior in the plastic region appears difficult to resolve due to non-linearity, especially if an initial assumption of plasticity appears to be wrong. This is circumvented by trying the different regimes in a fixed order. First, the adhesion solution is computed and tested against the constraints. If the contact conditions are violated by this solution, the slip solution is formed, together with the amount of plastic deformation needed to get $\tau_{Ic} = g_I$. The slip is adjusted to account for this plastic deformation. If the slip then no longer opposes the tractions, the solution must be found in the plastic regime.

A stable solver was constructed and tested in MATLAB and then implemented in CONTACT for both transient and steady state rolling. Initially, the calculations for the plastic regime were worked out for unidirectional tractions only, restricting the solver to 2D situations. The scope of the work was increased later, extending the solver to 3D configurations.

4.4 Results on Plasticity

Several tests were performed to check that the implementation functions correctly and to explore the effects of plasticity on the results.

The rate of work hardening is made comparable between different cases using the ratio $k_{rel} = k_u/G$. For $k_{rel} \uparrow 1$, $k_\tau \to \infty$. This means that the yield limit τ_c increases rapidly already at the smallest amount of u^*_{pl}. At the other extreme, $k_{rel} \downarrow -1$, results in $k_{rel} \to -\infty$. This means that the material collapses almost instantaneously when the tractions reach the initial yield limit τ_{c0}. A lower limit $\tau_c \geq 0.1\tau_{c0}$ is used to prevent a full collapse.

4.4.1 2D, Little Plasticity at Large k_{rel}

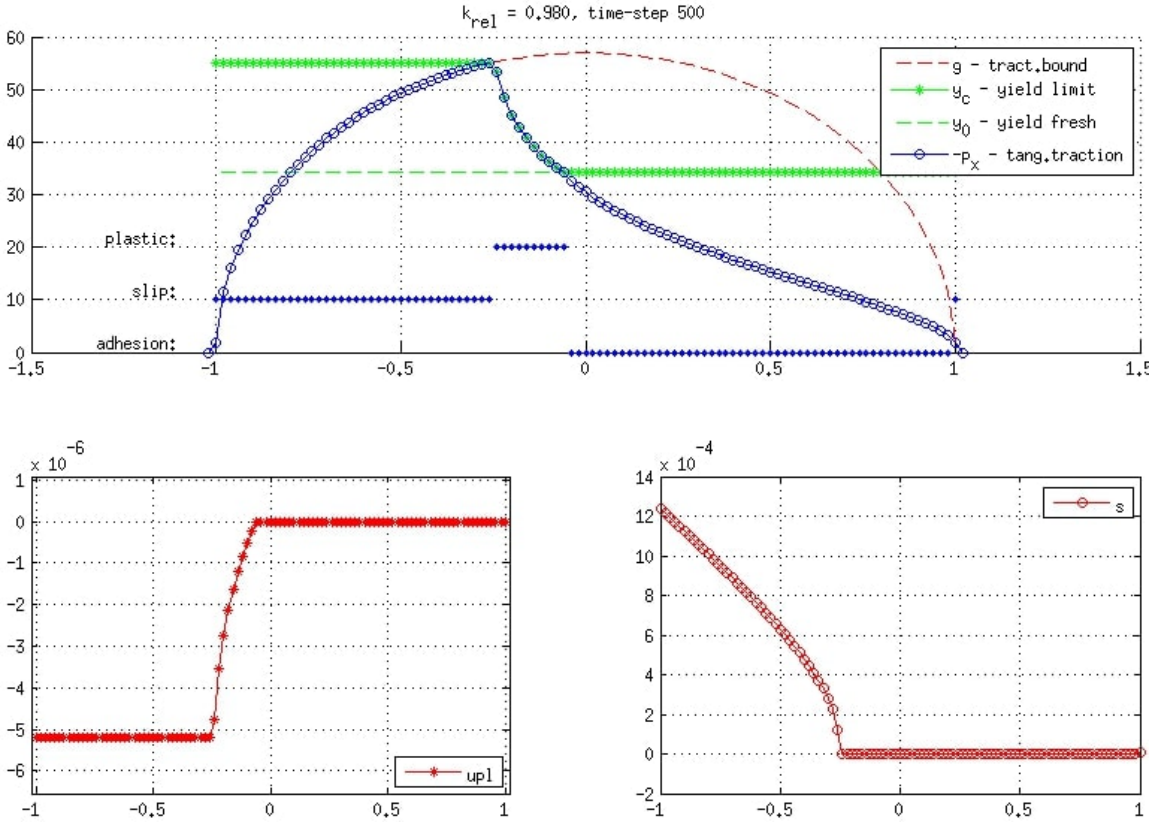

Figure 36. Results for the 2D Carter test case with $k_{rel} = 0.98$, $\delta_x = 0.02$, $\xi = 0.00040$, top: tractions, yield limit and element division, bottom: corresponding plastic deformations u_{pl} and slip s

The first test case considered is for k_{rel} close to 1, such that the plastic yield limit τ_c increases quickly with plastic deformation. This enlarges the amount of elastic deformation that can occur, such that only limited plastic deformation is found. This is illustrated in Figure 36 for a 2D test case of steady rolling with $k_{rel} = 0.98$. The traction profile closely resembles the well-known Carter solution (Figure 2), which is the expected behavior.

4.4.2 2D and 3D Transient Rolling, Converging to Steady State

The second test case uses $k_{rel} = 0.60$, as shown in Figure 37. This figure shows the results obtained by running the transient solver for a long simulation time where the solution settles on a steady state. Results are shown for grids with elements of $\delta_x = 0.02$ (top) and 0.08 mm (bottom). These show largely similar trends and values, increasing confidence in the implementation.

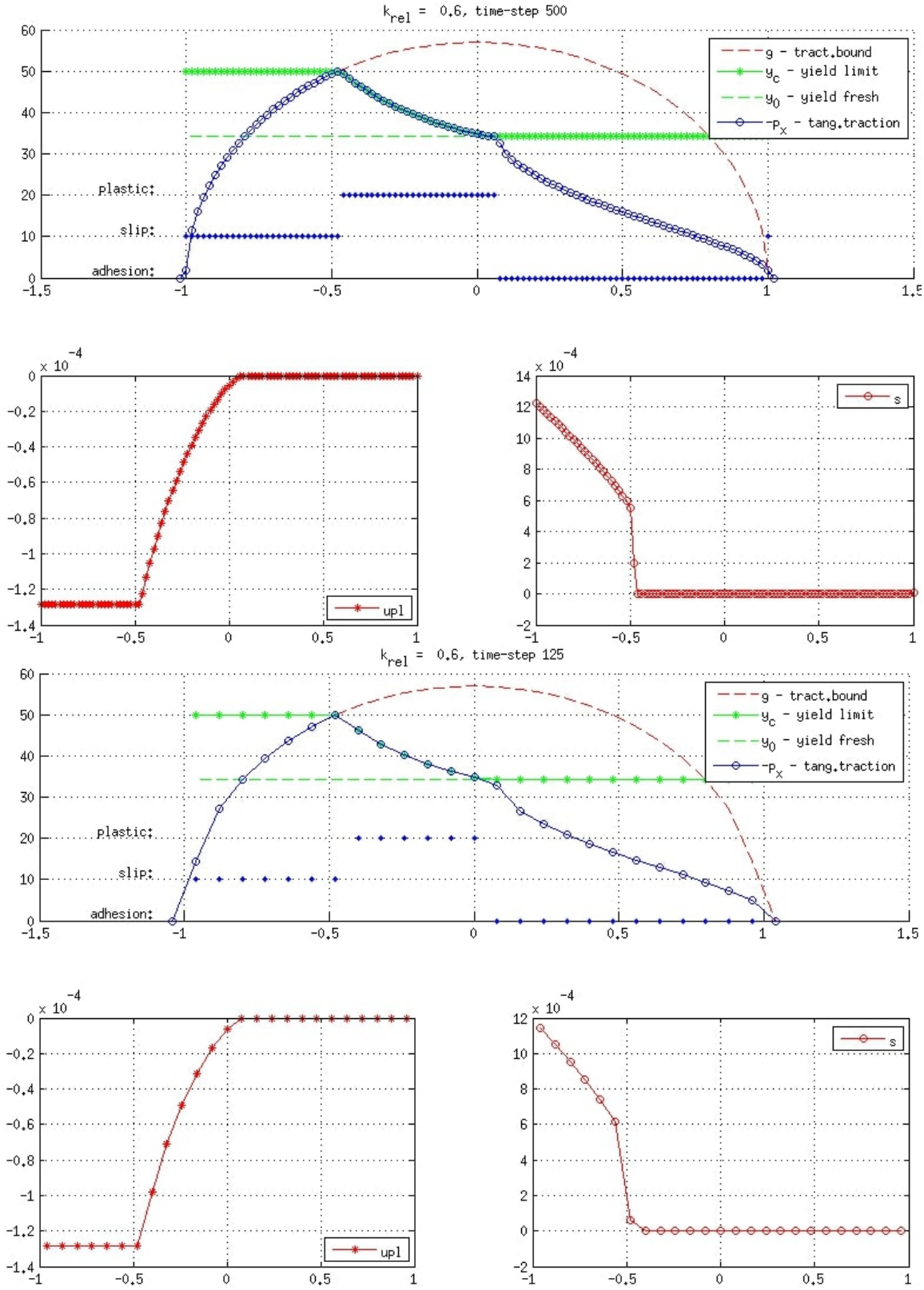

Figure 37. Results for 2D Carter test case with $k_{rel} = 0.6, \xi = 0.00040$, top: $\delta_x = 0.02$, bottom: $\delta_x = 0.08$

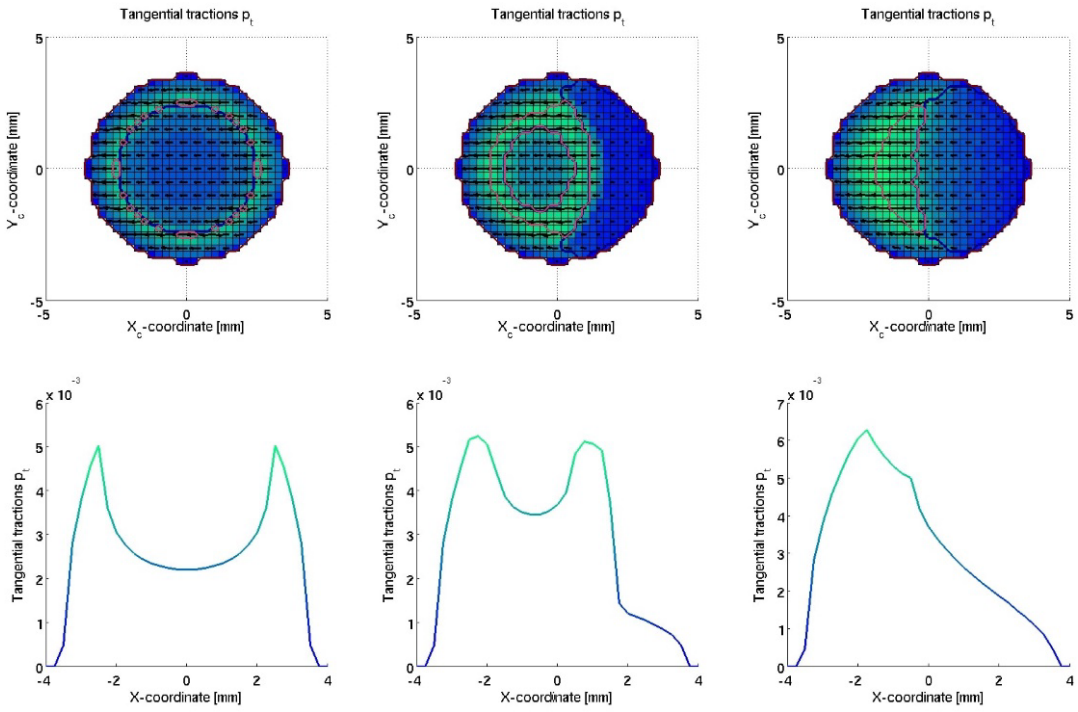

Figure 38. 3D transient solution at timesteps 1, 8, and 56, top: top view on contact area, bottom: cross-section at $y = 0$

Figure 38 presents the time-evolution of the solution for a 3D transient test case, starting with the Cattaneo shift problem, then rolling at constant creepage until the steady state has set in. Time steps 1, 8, and 56 are show in the picture. The solution obtained after 56 time steps is close to the solution of the steady state solver.

4.4.3 Shearing of Interfacial Layers

The next test considers the rheometer experiments reported by Hou and colleagues (1997) and shown in Figure 28. Different powders were placed on an anvil, and were pressed and sheared, measuring the shear stresses as a function of slip distance. Results were presented for magnetite, clay, sand, and molybdenum disulfide (MoS_2), compressed at 900 N/mm^2. The measured rheologies are approximated here by piece-wise linear functions, characterized by the threshold point (u_{c0}, τ_{c0}) where the slope of the curve changes, and by the slope k_u in the plastic regime. The values used are shown in Table 2. The resulting curves are shown in Figure 35, independent of any simulation, while Figure 39 shows the simulation results.

Table 2. Parameter values used in CONTACT to model the strength of interfacial layers as measured by Hou, et al., 1997

Third Body Layer	u_{c0} [mm]	τ_{c0} [N/mm^2]	k_u [N/mm^3]
Magnetite	0.070	560	0.
Clay	0.040	200	400.
Sand	0.050	400	-200.
MoS_2	0.020	20	20.

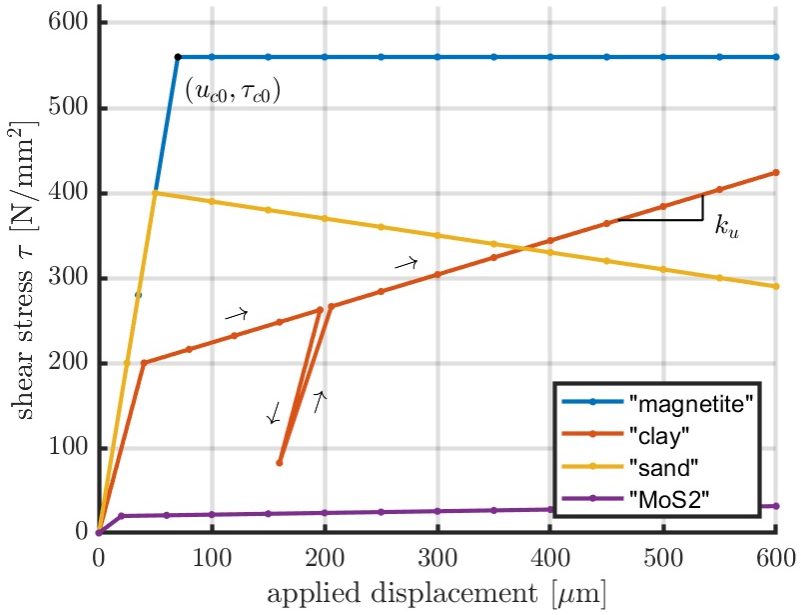

Figure 39. Shear stress curves computed by CONTACT for several compounds, mimicking the results of Hou and colleagues (1997)

The simulations concern a single element in contact with size 1 mm^2, carrying a normal load $F_n = 900$ N. The upper body is shifted to the left with respect to the lower, in 13–17 discrete steps of -0.035 or -0.050 mm. Additional steps are inserted in the "clay" series, using one step to the right, $+0.036$ mm, to show the corresponding behavior. The resulting stresses $\tau = p_x$ are computed by CONTACT as shown in Figure 39.

In CONTACT, the desired slope τ_{c0}/u_{c0} comes about by a combination of elastic deformation in the layer and in the primary bodies. The flexibility of the latter is found using a test without interfacial layers: $F_x = 84.97$ N at a shift of -0.001 mm. For a given layer thickness, the elastic modulus is then obtained as

$$L_{tot} = L^{(1,2)} + L^{(3)} \;\rightarrow\; \frac{h^{(3)}}{G^{(3)}} = \frac{u_{c0}}{\tau_{c0}} - \frac{0.001}{84.97} \;\rightarrow\; G^{(3)} = h^{(3)} \cdot \left(\frac{u_{c0}}{\tau_{c0}} - \frac{0.001}{84.97}\right)^{-1}. \qquad (50)$$

Using the values of Table 2 with a layer $h^{(3)} = 20\ \mu m$ results in $G^{(3)} = 176.6, 106.3, 176.6$ and 20.4 N/mm^2 for the four materials.

One relevant finding from this computation is that the shear moduli found are 500 to 1,000 times lower than for steel (82,000 N/mm^2). This suggests that elasticity may be unsuited to explain the initial portion of the measured curves. An alternative explanation is that the particles in the layer are rearranged over a short distance, compacting the layer with a strong work-hardening characteristic. Other mechanisms may then kick in at higher stresses with a much lower work-hardening characteristic. This mostly fits with Kalker's (1992) description with the acknowledgement that there can be different mechanisms acting at the same time and in different configurations. The precise mechanisms are of lesser concern if the rheology can be captured, describing the shear stress as a function of velocity accommodation, using Equations 36–37 or a similar form.

A consequence of this "compacting view" is that elastic displacements $\vec{u}_{el}^{(3)} = L^{(3)}\vec{p}$ should be replaced by additional plastic deformations. This refinement has not been implemented because the added value seems low (the energy dissipation is small compared to that of the plastic regime) and because the flexibility $L^{(3)}$ simplifies equation solving, whereas plasticity complicates the equations.

4.4.4 2D Comparison to Meierhofer's Results

Another example concerns Meierhofer and colleagues' test case (2014; Table 3). This 2D test case compares Meierhofer's model and the new one in CONTACT. Note that where Meierhofer's model needs a 3BL thickness h, there is no corresponding parameter for the plastic regime in the new model.

Table 3. Parameter values used in comparison to Meierhofer's results

Parameter	Symbol	Value	Unit
Elastic modulus of rigidity	G	77,519.4	MPa
Plastic modulus of rigidity	k_u	3,000	MPa/mm
Rate of increase of yield limit	k_τ	3,121	MPa/mm
Initial yield strength	τ_{c0}	200	MPa
Poisson's ratio	ν	0.29	-
Coefficient of friction	μ	0.5	-
Total normal force	F_n	1,323.6	N/mm

Figure 40 shows the tractions p_x of Meierhofer and CONTACT side by side, at creepages $\xi = 0.3$ and 1.0 percent. The results have generally similar behavior, although the precise values are different. The present model generally finds higher stresses, both in the purely elastic case and the extended case where plasticity is included. This is attributed to a difference in the contact length a, which may have been smaller in this case than in Meierhofer's test case. Additionally, Meierhofer uses a parabolic Hertzian solution while this project's team used the full linearly elastic model for the normal problem.

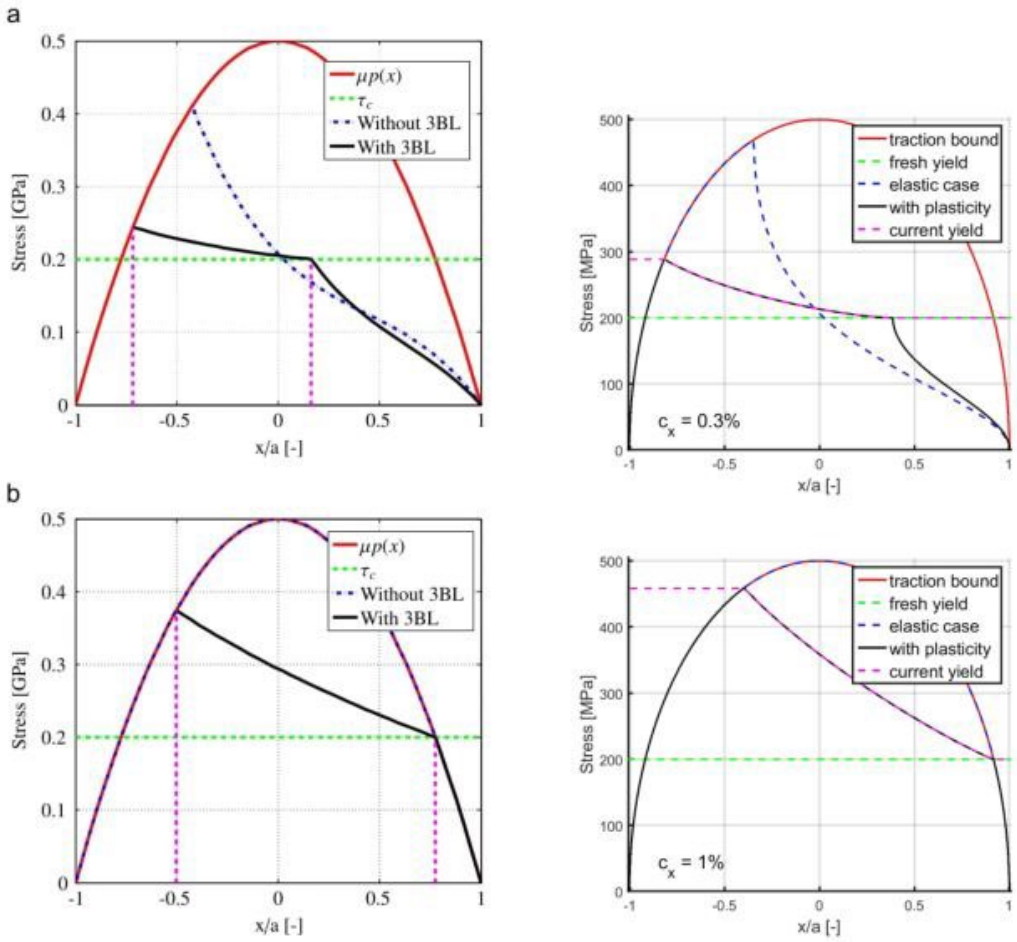

Figure 40. Left: results from Meierhofer, et al. (2014), right: results of the Extended CONTACT model (parameters in Table 3), top: Creep $\xi = 0.3$ percent, bottom: creep $\xi = 1.0$ percent

4.4.5 2D Creep Versus Creep-Force Curves

Local plasticity is primarily considered because of its effect on the coefficient of traction, that is, the shape of the creep versus creep-force curve. The team explored this for the 2D situation used by Meierhofer (Table 3) for a range of values k_{rel} (Figure 41). Three different situations are distinguished in this figure according to the scenarios $k < 0$, $k = 0$ and $k > 0$ (note that k_u, k_τ and k_{rel} have the same sign).

1. If $k_{rel} = 0$, then the plastic yield stress τ_{c0} effectively replaces the traction bound μp_n in the middle region with high pressures. This reduces the tangential force that can be transmitted, such that the traction curve saturates at a lower value than the Coulomb maximum. Note that this maximum value depends on τ_{c0} in relation to the range of μp_n.
2. If $k_{rel} < 0$, then the coefficient of traction is reduced further compared to that of $k_{rel} = 0$, and a negative slope is obtained after attaining a maximum value.
3. If $k_{rel} > 0$, then the coefficient of traction asymptotically rises to the COF μ at large enough creepage. How quickly this saturation occurs depends on the value of k_{rel}, as

well as on the value of τ_{c0} compared to μp_n. The creep-force curve is hardly affected for $k_{rel} > 0.3$ ($\tau_{c0} = 0.4$ max (μp_n)) or $k_{rel} > 0.1$ ($\tau_{c0} = 0.7$ max (μp_n)). Smaller k_{rel} results in a slower transition from the linear to saturated regimes.

The creep-force characteristics for small, positive k_{rel} resemble the experimental values presented by Meierhofer et al. (2014).

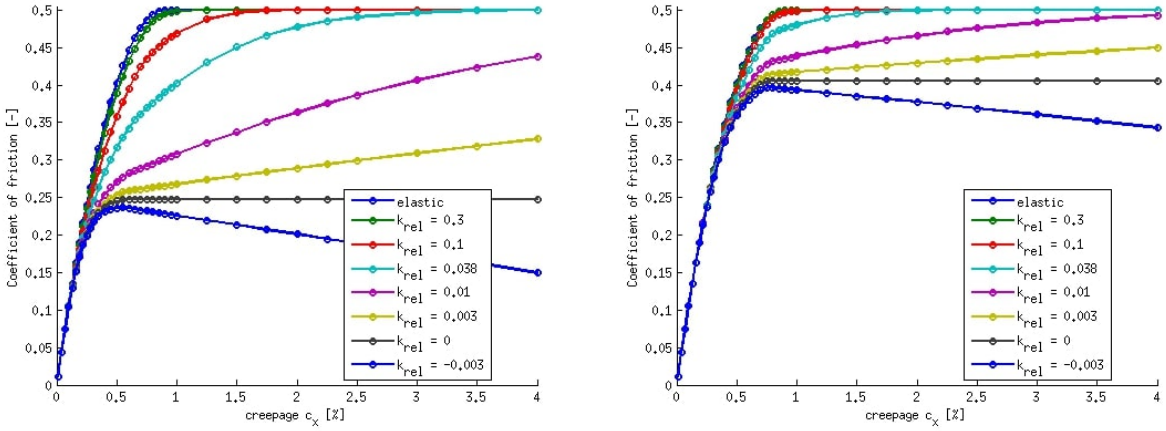

Figure 41. Coefficient of traction as a function of amount of creep (parameters in Table 3), left: $\tau_{c0} = 200$ MPa, right: $\tau_{c0} = 350$ MPa

4.5 Conclusions Regarding Solid Third Body Layers

There is strong evidence of plastic deformation of the wheel and rail materials in the sub-surface layer close to the contacting surfaces. Part of this plasticity is termed "global", related to peak pressures due to non-conforming profiles. Another part, termed "local plasticity", is concerned with the tangential shear stresses. The research team hypothesized that this local plasticity continually increases even after the surfaces have run in, and that it may significantly alter the creep-force behavior.

The CONTACT model was extended to account for this local plasticity or other mechanisms that lead to similar energy dissipation. The team postulated the existence of a tangential yield stress τ_c for this. Plastic deformation $\dot{\vec{u}}_{pl}$ occurs in the direction of the tractions $\vec{p}$ where this yield stress is reached, much like the occurrence of micro-slip $\vec{s}$ where the tangential traction bound $g = \mu p_n$ is reached for Coulomb friction. The tangential yield stress was postulated to change with the amount of accumulated plasticity u_{pl}^*, using the three simplified schemes of Hou and colleagues (1997): $k > 0, k = 0, k < 0$. This is expressed in a model of equalities and constraints in Equations 28 to 38. This model is discretized and then solved rigorously by distinction of the possible regimes.

The new model deviates from Meierhofer and colleagues' model in at least three different ways.

1. The research team allowed for plasticity to occur in the wheel and rail surfaces instead of confining it to the third body layer. The quantity $\vec{u}_{pl}$ shows how much the opposing surfaces are displaced with respect to each other, with no reference to the depth distribution of this in the material.

2. The condition was added that $\dot{\vec{u}}_{pl}$ is in the same direction as the tractions, ensuring that $\vec{u}_{pl}$ remains intact upon relieving the stress, and that energy is lost by plastification. In Meierhofer and colleagues' model, the third body layer acts as a spring with variable stiffness that undoes plastic deformation when the stresses diminish. Energy may still be dissipated in their model, increasing the micro-slip $\vec{s}$ compared to the fully elastic situation. However, this is not guaranteed in situations with mixed creepage. Further, the energy is dissipated at the wrong place, affecting for instance the calculation of surface temperatures.
3. A third difference between the two models concerns the method of discretization. The series of polynomial terms used by Meierhofer et al. is essentially restricted to 2D situations. Using a grid-based discretization, the new model allowed the team to incorporate the effects of local plasticity in 3D situations.

Calculations with the new model show the robustness of the calculation of different regimes, over a wide range of k_{rel}, τ_{c0} and creepages ξ. In 2D, the results of the model are comparable to Meierhofer and colleagues', truncating the tangential tractions $\vec{p}$ in regions with high pressures. Further test cases show the extension to 3D configurations. The model accurately captures the behavior of Hou's experimental setup, including the desired behavior upon unloading and change of the shift direction.

Previous results showed that solid third body layers may explain the reduced slope of creep versus creep-force curves if elastic layers are used with very low elastic modulus (Vollebregt, 2014). The results of Section 4.4.3 show that this premise may indeed be realistic. The initial slopes of Hou's measured curves are far too low for steel-on-steel contacts and could be reproduced using 500–1,000 times lower elastic modulus for the layer than for the primary bodies. The view is postulated that the initial part of the curves is not governed by elastic deformation. The particles that make up the layer could be rearranged, rolling and sliding, slightly displacing, before they get stuck and experience plastic deformation. These actual mechanisms can be treated in the model using a soft elastic layer.

The new results show that local plasticity further effects the creep versus creep-force behavior. A slower transition from the linear to the saturated regimes is obtained, particularly at small values of k_{rel}. These results show good resemblance to twin-disc experiments as presented by Meierhofer and colleagues (2014).

5. Effects of Interfacial Fluids

This section presents the research team's work on interfacial fluids and their effects on friction. Section 5.1 discusses some key findings on the various roles of fluids in wheel-rail interaction. Next, the different forms of lubrication are reviewed, in a general setting, followed by the existing modeling efforts in railways, focused primarily on wet rails and high-speed situations. The state-of-the-art of modeling is discussed in Section 5.3.

The work consists of an extensive literature survey and exploration of the presented models. Based on this, the authors conclude that current modeling is insufficient for the needs of detailed creep-force modeling. One of the main purposes of CONTACT is to compute the distribution of frictional tractions. To do this well in a situation with fluids requires detailed understanding of temperature variations, how they come about and work with viscosity, for instance. This is beyond the scope of the current investigation.

5.1 Different Roles of Fluids in Wheel-Rail Adhesion

Different fluids are found in wheel-rail contact: water, lubricants, oily substances from leaves, and oil contamination; these are studied for different reasons.

5.1.1 Factors Affecting Adhesion

Early works by British Rail Research (Broster, et al., 1974; Beagley, et al., 1975a; 1975b; Beagley & Pritchard, 1975) explored the influence of oil, wear debris, and water on adhesion. Whereas friction levels over 0.6 are attained on clean, dry rails, the COF is reduced to 0.3 on wet rails if no oil is present, and to 0.2 if the oil coverage is increased. Lower values could be found in the presence of solid debris.

Logston and Itami presented extensive creep-force measurements on EMD locomotive "SD45X" (1980). The rail conditions that were studied included dry, wet, and oiled, without and with sanding. The resulting curves show considerable differences in shape for dry and wet conditions, as illustrated in Figure 6. The level of friction reduces in the presence of water. Further, the marked peak found in dry and dry-sanded conditions is also much reduced in wet conditions.

Polach (2005) collected measurement data from locomotives for dry and wet tracks, running at different speeds (16–60 km/h). The measured data generally exhibit the same pattern as shown in Figure 6. They could be fitted well by tuning the parameters in Polach's fast computation approach.

Further works by British Rail Research were reviewed by Fulford:

> McEwen (1999) concludes that the mechanism by which gross water on the rail influences adhesion is still not fully understood but the result is known. Water appears to act as a "weak lubricant" in that it reduces adhesion when it is initially high but not to the same level as an oil-based lubricant. Water is readily pushed aside by passing wheels and does not form a boundary layer like oil due to the molecule size. McEwen's view is [that] water promotes surface oxidation of the steel rail such that exceedingly thin oxide films protect the surface from metal-to-metal contact, thus seeing oxide/oxide friction levels and not steel/steel friction levels (Fulford, 2004).

Oldknow and colleagues (2013) studied the influence of third body layers at the wheel/rail interface on curving forces in actual heavy haul operating conditions. The lateral and vertical forces exerted on the rail were collected for many axles in dry and wet conditions, with and without friction control, using a top of rail friction modifier. In wet conditions, the friction level rose after the first few locomotives and cars passed, to levels that would be expected in dry high-friction cases. This is attributed to "flushing" of the pre-existing third body layer, and its replacement by a layer of iron oxides.

These results show that wheel-rail contact is affected by many factors. A layer is formed in the wheel-rail interface of varying composition. This is captured in the Kalousek bathtub model (Figure 8). The available measurements show what kind of behavior may be expected in different circumstances, (i.e., the shape of the curves) but quantitative predictions are currently not possible.

5.1.2 Loss of Adhesion

Loss of adhesion ("slippery tracks") received considerable attention on its own, because of the induced safety problems (safe braking distance, signals passing at danger) and operational consequences (delays, capacity reduction; Olofsson & Lewis, 2006; Arias-Cuevas, 2010; Trummer, et al., 2017). A possible explanation was put forward in the research by British Rail mentioned above:

> On rails covered with substantial quantities of debris, [...] any "minimally wet" conditions such as mist, dew or slight rain may supply enough water to provide a surface paste of just the viscosity to lubricate the wheel/rail contact and substantially reduce adhesion (Beagley & Pritchard, 1975).

Other research focused on the effects of leaf fall, which creates a tacky layer on the rail surface (e.g., Cann, 2006; Arias-Cuevas, 2010; Zhu, 2011). The two factors appear to co-exist with each other: in Great Britain, autumn leaf fall has been reported for about half of the incidents related to low adhesion (RSSB, 2014). Other cases are attributed to the combined effects of iron oxides and water (Trummer, et al., 2017; Six, et al., 2017). Fulford states:

> Regarding the surface chemistry, McEwen (1999) reports that the leaf-related low adhesion process could also be seen to be similar to the "paste effect" process described for solid debris […]. It states that neither the mechanism of lowering adhesion by particulate solid/water pastes nor that by leaf films can be described in classical terms. In all probability, it is reported that the former shares much with elasto-hydrodynamic lubrication and the latter with the full film hydrodynamic lubrication. However, both of these mechanisms can only be described mathematically assuming defined viscosity properties of the single-phase lubricant. In the cases of pastes or leaf films on the rail, the lubricant is a solid/liquid mixture of varying proportions with very complex non-Newtonian flow characteristics (Fulford, 2004).

5.1.3 The Effects of Water in High-Speed Railways

Rain introduces water as a natural lubricant into the system, reducing the height and changing the shape of creep versus creep-force curve (Polach, 2005). The achievable traction (adhesion) reduces further with increasing train speed (Ohyama, 1991; Polach, 2005). These factors are

important for the design of traction control strategies for modern locomotives, and for high-speed acceleration and braking.

Ohyama presents measured adhesion coefficients on Shinkansen under wet conditions (1991). A considerable reduction is found from $\mu > 0.14$ at low speeds to 0.04 at 260 km/h. Experiments are reported on a full-size twin disk machine, exploring the effects of water, surface roughness, speed, and oil:

> Under water-lubricated conditions, the adhesion coefficient decreased drastically with increasing rolling speed and the effect of surface roughness was remarkable. The phenomena are consistently explained by the contact load being shared by the asperities through a water film (Ohyama, 1991).

Further experiments have been conducted on the influence of water temperature and surface roughness (Chen et al., 2008). The values obtained for the adhesion coefficient are found to be lower at lower water temperature. This is due to the higher viscosity at lower temperature, resulting in an increase of the water film thickness, supporting a bigger portion of the normal load. Moreover, a large scatter is found in the experimental results, which is attributed to variations in the surface state of the materials in rolling contact. In the experimental studies, an opposite effect is found for the roughness orientation, compared to the numerical predictions.[1]

In more recent years, similar experimentation efforts have been carried out at Southwest Jiaotong University (SWJTU), Chengdu, (Wang, et al., 2011), and at the China Academy of Railway Sciences (CARS), Beijing, (Chang, et al., 2018). These results generally confirm the earlier ones: in wet conditions, the available wheel-rail adhesion reduces with increasing speed, especially if relatively smooth surfaces are used. Adhesion reduces more with more water spray, up to a point where the amount of water does not affect adhesion anymore. Relatively mild influences are a further decrease of adhesion at lower water temperatures, and at increased axle loads.

5.1.4 Gage Face Lubrication

Rapid wear may arise in curves due to flange contact, with large micro-slip occurring due to a high contact angle and large spin creepage. This wear may then be reduced by flange lubrication. Different benefit factors have been reported, from 3–9 times according to (Olofsson & Lewis, 2006), to 5–10, or 10–20 times according to (Magel, 2017).

> Fuel savings of approximately 30% (compared to dry conditions) have been reported for measurements taken on test tracks. Other studies carried out in the field have shown improvements of a similar order of magnitude (Olofsson & Lewis, 2006).

Different kinds of lubricants may be used (Olofsson & Lewis, 2006):

> …low friction modifiers can be solid or liquid (greases), the main difference between the two being the thickness of the film they form in the wheel/rail contact (solid lubricants will give a film of $10 - 30\ \mu m$ and grease lubricants less than $5\ \mu m$ (Zakharov, et al., 2001).

[1] This apparent disagreement may be due to different definitions of the orientation parameter γ, by which the experiments would be in line with the numerical simulation.

5.1.5 RCF Crack Initiation and Propagation

Another motivation to study fluids could be its influence on RCF damage.

> In laboratory investigations of RCF it has proved virtually impossible to produce extensive cracking in the absence of a fluid [...]. Way (1935) was the first worker to observe this and comment on it. He suggested that the role of the fluid involved penetrating the crack and pressurizing the crack tip to cause propagation. Although alternative explanations have been offered [...], most of the recent research [...] supports his original idea (Clayton, 1996).

These different configurations and aims complicate the development of an extension of CONTACT for fluids in wheel-rail contact. What can be done, in a reasonable time, with good confidence in the results?

5.2 Modeling Approaches Used for Fluids in Wheel-Rail Contacts

Several modeling approaches have been put forward over time to account for the presence of fluids in wheel-rail contacts. A distinction is made between more empirical/phenomenological approaches versus more physics-based models. Before these are further explored, the authors review the main findings on lubrication from the general tribology field.

5.2.1 Tribological Understanding of Lubrication

Lubrication has been used to reduce friction since ancient history. Egyptians used animal-fat as lubricant for wheel bearings in chariots (Dowson, 1998; Bhushan, 2000). Da Vinci introduced the notion of a “coefficient of friction” as the ratio between friction force and normal load. Petrov, Tower, and Reynolds developed understanding of lubrication at the end of the nineteenth century, uncovering the principles of hydrodynamic lubrication (Petrov, 1883; Tower, 1883; Reynolds, 1886).

Different Lubrication Regimes

Sliding contacts may occur in different lubrication regimes as shown in Figure 14, distinguished by the amount of interfacial fluid present.

1. Boundary lubrication (BL): In the absence of sufficient fluid lubrication, friction is dominated by solid contact at the asperities. In this regime, the friction force depends linearly on the load carried. The COF depends on the materials that are contacting each other. Values of 0.6–0.7 may be found for clean steel-on-steel contacts, while oil coverage of just a few molecular layers may cause a reduction to 0.15 (Beagley, et al., 1975a).
2. Hydrodynamic lubrication (HD): In the HD regime, a continuous film of liquid is present between the two sliding contacts, such that no solid contact occurs. Extremely low coefficients of friction can be achieved by this mechanism. Higher friction is generated at increased sliding speeds because of increased viscous drag.
3. EHL: EHL is a subset of HD lubrication, where the elastic deformation of the solids plays a significant role. This occurs when the film is thin compared to the surfaces' roughness, with asperities touching in isolated areas.

4. Mixed lubrication: Mixed lubrication occurs in the transition between EHL and BL. The load is supported by solid contact at the asperities, and by a discontinuous fluid film.

These regimes are illustrated further in Figure 42.

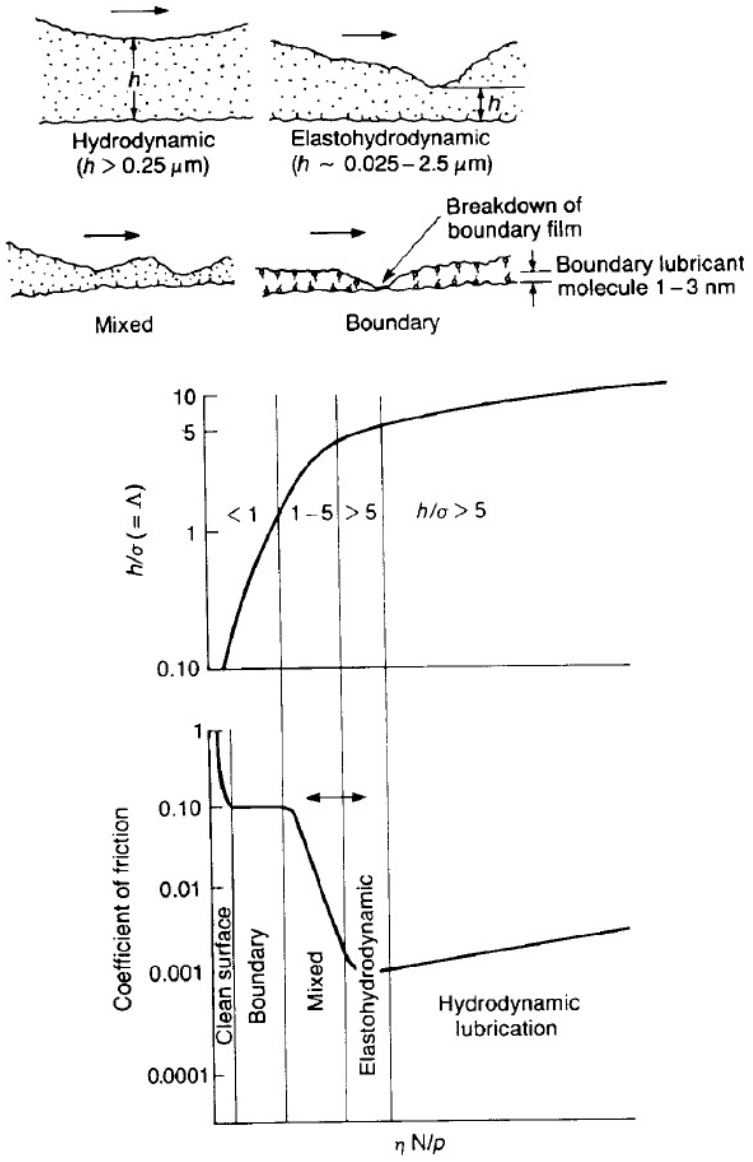

Figure 42. Illustration of different lubrication regimes and their relation to the Stribeck curve (Bhushan, 2000)

The Stribeck Curve

Film thickness and drag are governed by the amount of fluid trapped between the surfaces, in a balance between feeding (velocity) and draining (pressure and low viscosity). New fluid enters the contact zone as the contact moves forward. This fluid is squeezed out by the buildup of pressure. The pressure needed to squeeze the liquid depends on its resistance, governed by the viscosity of the liquid.

These general patterns lead to the so-called Stribeck curve (Stribeck, 1902; Figure 42): high, constant friction in the boundary lubricated regime, reducing in the mixed lubrication regime, a minimum value at a thin film, and rising friction at increasing film thickness.

Elasto-Hydrodynamic Lubrication

In full hydrodynamic lubrication, fluid pressures are distributed over relatively large areas, and exhibit gradual variation. This changes as the geometry becomes more complicated, with smaller fluid film thickness. A classic example is presented in Figure 43, showing the pressure build-up and the resulting solid surface deformation. The pressure drops quickly on the right side, at the outlet of the fluid. This leads to a decrease of elastic deformations, decreasing the height of the gap available to the fluid. This is accompanied by an increase of fluid velocity. A remarkable spike is found in the pressures, to accelerate the fluid by the right amount.

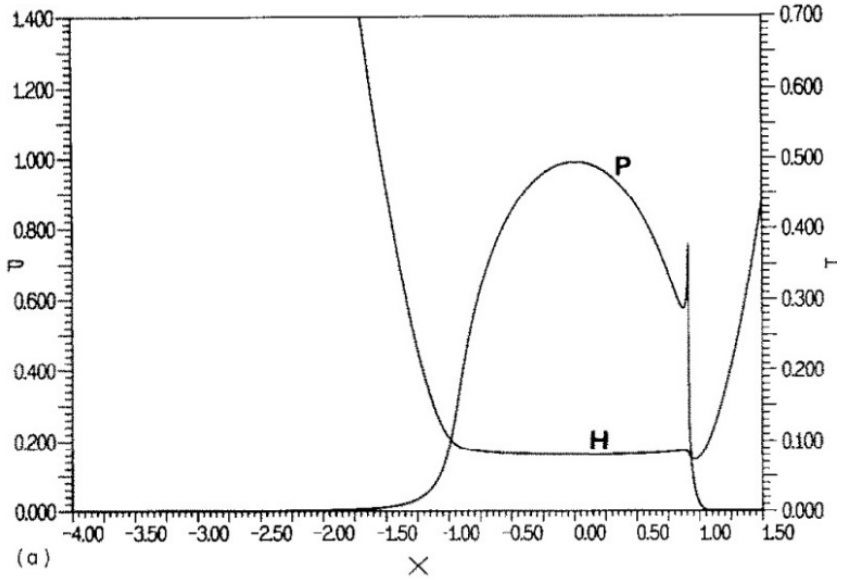

Figure 43. Dimensionless pressure *P* and film thickness *H* as a function of *x* with a pressure spike at the outlet of the fluid (Venner & Bos, 1994)

Fluid Rheology

The viscosity of many fluids depends strongly on pressure and temperature (Hamrock, et al., 2004). Barus (1893) presented an initial approximation, limited to medium pressures. Roelands (1966) presented an extensive survey. The relationship between stresses and shear rate deviates from the linear (Newtonian) behavior, as described by Eyring (1938). Johnson and Tevaarwerk (1977) presented a simple constitutive equation, covering a wide range of circumstances.

Effects of Surface Roughness

There is abundant evidence for the importance of surface roughness in the presence of lubrication (See Ohyama, 1991; Chen, et al., 2016; Chang, et al., 2018 for results pertaining to railways). However, this roughness only plays a role when the separation between the surfaces is small compared to the asperities.

The ratio h/σ is an important parameter showing the effects of surface roughness. For $h/\sigma \gg 3$, the roughness effects are not important, and smooth film theory is sufficiently accurate. The roughness effects become important as $h/\sigma \downarrow 3$. As h/σ is decreased further, asperities start interacting with each other and contacts form (Patir & Cheng, 1978).

Here, h is the nominal fluid film thickness, defined as the distance between the mean levels of the two surfaces, and σ^2 is the variance of the combined surface roughness.

5.2.2 Phenomenological Modeling

Fast modeling approaches have been posed to capture the main effects of lubrication, without adequately considering how these effects happen. A main example is the Polach model (Polach, 2005), which allows for adjusting the form of creep-force curves with five heuristic parameters, k_A, k_S, μ_0, A, B. These parameters affect the initial slope at low creepage, the maximum friction level, the decline at high creepage, and the transitions between these different regimes. The range of possible values is shown for creep-force measurements on different locomotives. These are obtained by fitting the model to experimental results; no explanation has yet been put forward on how the parameters come about.

Similar capabilities are provided by Modified FASTSIM (Spiryagin, et al., 2013) and Extended CONTACT (Vollebregt, 2014): extensions are provided with respect to Kalker's original approaches (Kalker, 1982; 1990), by which the creep-force characteristic may be tuned to reflect experimental data.

Another proponent of this class is the WILAC model for low adhesion (Trummer, et al., 2017). This model is based on experimental adhesion characteristics for different rates of water flow. The corresponding parameters for Polach's model (2005) are fitted to each case using linear regression. Creep forces for a real scenario are then predicted using blending of different fitted conditions.

The benefit of these empirical approaches is their fast computation (Polach model, Modified FASTSIM), and the flexibility to match experimental data. This is particularly relevant for configurations where the input parameters are variable (i.e., the amount of debris and contamination), the physics are not well understood (viscosity-pressure relation), and the details of the process (stresses) are of little concern.

5.2.3 Physics-Based Modeling Approaches

Current physics-based modeling of fluids in railways focuses mostly on the effects of water in high-speed railways.

RTRI, Japan

In 1991, Ohyama used a range of modeling approaches to capture the experimental data. The fluid film thickness was assessed using numerical (2D EHL) analysis and found to be small compared to the surface roughness; therefore, mixed lubrication is assumed. A load-sharing concept was adopted from Johnson and colleagues (1972): the total load P is carried partly at the asperities, with the remainder carried by the fluid.

We are concerned with how the division of the total pressure p into fluid pressure p_f and asperity pressure p_a is governed by the properties of the surfaces and the conditions of lubrication (Johnson, et al., 1972).

The traction force Q is split accordingly, $Q = \mu_a P_a + \mu_f P_f$, with P_a, P_f the loads borne by asperities and water, and μ_a, μ_f the friction coefficients on both parts. The latter contribution is considered negligible compared to the former, because $\mu_f \ll \mu_a$. That is, friction is accounted for at the metallic asperity contacts only. The normal load P_a was estimated using Greenwood and Williamson's theory for rough surfaces (1966, see Section 2.1). The output of the model was the available level of adhesion $\mu = \mu_a P_a / P$.

Chen et al. extended Ohyama's numerical model to include surface roughness and viscosity effects (Chen, et al., 1998; Chen, et al., 2002), and to 3D situations (Chen, et al., 2005). The resulting model was based on the modified Reynolds equation, using flow factors according to Patir and Cheng (1978), elastic deformation in normal direction using the half space approach, and on the mean asperity contact pressure equation established by Ren and Lee (1994). Equations were solved with a multi-level technique according to Venner and Lubrecht (2000). The simulation results indicate that the standard deviation of the roughness height and the roughness orientation have significant influence on the level of adhesion.

The model was refined further with the boundary friction coefficient for metallic contacts and assessing the ratio of real to nominal contact area at different loads (Chen, et al., 2011). The authors suggest that further work may be needed: "The adhesion coefficients obtained by the improved approach have a tendency to roughly agree with the field test results of Japanese Shinkansen vehicle (Series 200)" (Chen, et al., 2011).

Graz, Austria

Tomberger and colleagues (Tomberger, 2009; Tomberger, et al., 2011) presented an integrated modeling approach for rolling contact. Instead of providing the COF as an input value, local values were estimated based on interfacial fluids, surface roughness, and temperature.

The model assumed boundary and mixed lubrication. The nominal pressure distribution was fixed before the computation, using common approaches for dry contacts (Hertz, CONTACT, or FEM). This corresponds to an assumption of negligible variation of fluid film thickness $h \approx h_0$ according to Grubin's approximate treatment (Grubin, 1949; Dowson & Higginson, 1966). Rough surfaces were characterized using a Gaussian height distribution, which was used to find the metallic surface fraction at each separation height d, the metallic volume in a cell height l_c, and the cross-sectional areas A_x, A_y between adjacent cells. The fluid mass flow rate was computed analogously to the 3D method (Chen, et al., 2005), based on the modified Reynolds equation.

Fluid pressures p_f were deducted from the nominal pressures $\bar{p}$ to find the pressures p_a at the metallic contacts. These pressures were input to the available friction. The COF μ_a was adjusted with the surface temperature. Iteration was used to find the local slip velocities and associated heat input, the corresponding surface temperatures, local coefficients of friction, and the tangential traction distribution. The tangential elasticity was approximated using the simplified theory (Kalker, 1973), as used in FASTSIM (Kalker, 1982). This Tomberger model was

combined with the modeling of elasto-plastic third-body layers into the Extended Creep Force model (Meierhofer, 2015; Six, et al., 2015).

Chengdu, China

In more recent years, similar modeling efforts have been carried out at SWJTU (Wang, et al., 2011b; Wu, et al., 2013; Wu, et al., 2014; Wu, et al., 2016). A 3D numerical model was constructed using partial EHL theory, assuming mixed lubrication, using an improved multi-grid scheme for the solution (Wu, et al., 2013). A preliminary study was conducted on mixed oil and water lubrication, using 2D numerical simulation (Wu, et al., 2014).

The effects of temperature were assessed by Wu and colleagues (2016), using an extended form of the modified Reynolds equation considering thermal effects (Yang & Wen, 1990), using Roelands' equation for the dependency of viscosity on pressure and temperature (Roelands, 1966), and using the ZMC statistical model for asperity contact with plastic deformation (Zhao, et al., 2000). Tangential contact was not considered in these models, i.e., the models computed the available adhesion rather than the actual creep forces. Heat sources were confined to effects of compression and viscous dissipation in the fluid. Temperature had a significant influence on the results, increasing the adhesion coefficient due to the decrease of the film thickness.

5.3 Discussion

The discussion of the physics-based models in Section 5.2.3 shows that many factors are involved in the modeling of creepage and creep forces in wet conditions. These are summarized in Table 4.

Table 4. Components in the physics-based models of Section 5.2.3 and modeling choices used for each of them

Model component	Alternative choices		
Surface height	Gaussian distribution	Anisotropic	
Asperity load	Greenwood-Williamson	ZMC, elasto-plastic	Lee & Ren
Asperity friction	Constant μ_a or $k\sigma_y$	Dep. on temperature	
Nominal pressures	Grubin approach	EHL computation	
Fluid temperature	Constant/input	Variable/computed	
Fluid viscosity	Constant η	Dep. on temperature	Roeland equation
Fluid mass flow	Modified Reynolds eq.		
Asperity drag	Cross-sectional area	Patir & Cheng	
Bulk elasticity	Simplified theory	Linear elasticity	

In mixed lubrication, creep forces are understood to emerge from the following interacting processes:

- Tangential tractions arise chiefly at metallic contacts $\|\tau_a\| \leq \mu_a p_a$. This postulates a traction bound that may depend on BL and/or surface temperature.
- Local sliding may occur at the asperities, generating considerable heat input. This raises the temperature of the asperities and surrounding fluid.

- The viscosity of water is little affected over a wide range of pressures and reduces quickly as the temperature increases.
- The bulk elastic deformation is dominated by the overall, undeformed geometry. Nominal pressures mostly follow the Hertzian distribution.
- The load borne by the asperities arises in a balance with the fluid pressure p_f: reducing p_f reduces the cell height, causing the asperities to take over the corresponding load.
- Fluid pressures arise in response to squeezing of the fluid: the available cell volume, cross-sectional area, and viscous drag.

The challenge for model-building is to ignore the effects of lesser concern, in view of simplifications and uncertainties, and reach the simplest possible model for the effort.

- The Tomberger model ignores the effect of fluid pressures on overall elastic deformation, such that the nominal pressures can be solved independently from the tangential contact solution.
- The Tomberger model ignores the effect of temperature on fluid viscosity, such that the fluid pressures can be solved independently of the tangential contact solution.
- The Tomberger model uses simplified theory, ignoring the interactions of bulk elasticity at different surface positions, such that tangential stresses can be solved using the FASTSIM approach.
- The RTRI and SWJTU models ignore tangential contact and the corresponding heat input due to friction and micro-sliding.
- The solution procedures used in RTRI and SWJTU models are much more involved than those of the Tomberger model, related to the additional interactions of pressure and temperature calculations.

The research team concludes that the Tomberger model is the only physics-based model published to date for the calculation of the tangential tractions in wheel-rail contact that accounts for the effects of mixed lubrication. In its present form, the model seems to be applicable mainly for water-lubricated contacts in which relatively little frictional heating occurs. The temperatures computed by the model are a rough approximation, affected by the use of the FASTSIM approach for tangential contact and by the lack of feed-back between temperature and the build-up of fluid pressures.

A main purpose of CONTACT is to compute the distribution of tangential tractions for various contact conditions. A main goal of the current work is to account for friction modifiers. The Tomberger model does not fit either of these goals well. The distribution of tangential tractions differs substantially between CONTACT and FASTSIM, and these differences are enlarged by the feedback between tractions, micro-slip, frictional heat input, temperatures, fluid viscosity, and fluid pressures. Next, the simulation of fluids other than water requires understanding the rheology of the fluid: the variation of fluid viscosity with temperature and pressure.

5.4 Conclusions Regarding Fluids

This chapter discussed the roles of fluids in wheel-rail contacts and the corresponding modeling efforts. Different fluids (water, lubricants, oily substances from leaves, oil contamination) are

studied for different reasons. Early works concentrated on the general shapes of creep versus creep-force curves in various circumstances. Much work has been done on understanding and remediating loss of adhesion. Gauge face lubrication has mainly been studied practically, and high-speed train adhesion on wet rails is studied with both experimental and numerical means.

Existing creep-force models are divided roughly in two broad classes: fast, phenomenological approaches, versus detailed, physics-based modeling. Quick heuristic procedures have been published for the computation of creep forces in wet and low adhesion conditions, viz. Polach's model, Modified FASTSIM, and the WILAC model. These models are fitted to the desired outcomes using heuristic input parameters, providing the capability to include these effects in multi-body simulation. Current physics-based models are still somewhat restricted. Japanese and Chinese modeling efforts have focused on the maximum available adhesion instead of the actual creep forces, thereby obviating the need for tangential contact computation. On the other hand, the Austrian models included tangential contact, but left the detailed influence of contact temperatures out of account.

After careful study of the Tomberger model, the authors conclude that its extension and implementation in CONTACT is out of reach for the current work. They estimate that complete feedback mechanisms between fluid and temperature are needed to deliver trustworthy tangential tractions, which is a main purpose of CONTACT. Further, more insight is needed in the rheology and composition of other fluids and mixtures beyond water, how they behave under heat input and pressure. These aspects are left for further study.

6. Validation with Measurements

Here the authors describe the efforts undertaken to validate creep force models using measurements obtained from NRC Canada's wheel, bearing, and brake test facility (WBB). These data were measured in the summer of 2015 and provided to VORtech by Rob Caldwell (NRC) in September 2017.

6.1 Overview of NRC's Test Rig and Data Provided

An overview of the WBB is shown in Figure 44. The schematic at the top right shows the whole system, consisting of a rigid frame (grey, blue), the rollers (green), the wheelset (black) and the "reaction table" (red), to which the wheelset is attached. The image on the left shows the rollers at the bottom, and the wheelset and reaction table are in the upper half. Vertical and lateral actuators push the wheelset into the desired position and measure the forces required. The image on the right shows the other side, including the wheelset and longitudinal actuators. The set-up is illustrated further in Figure 45.

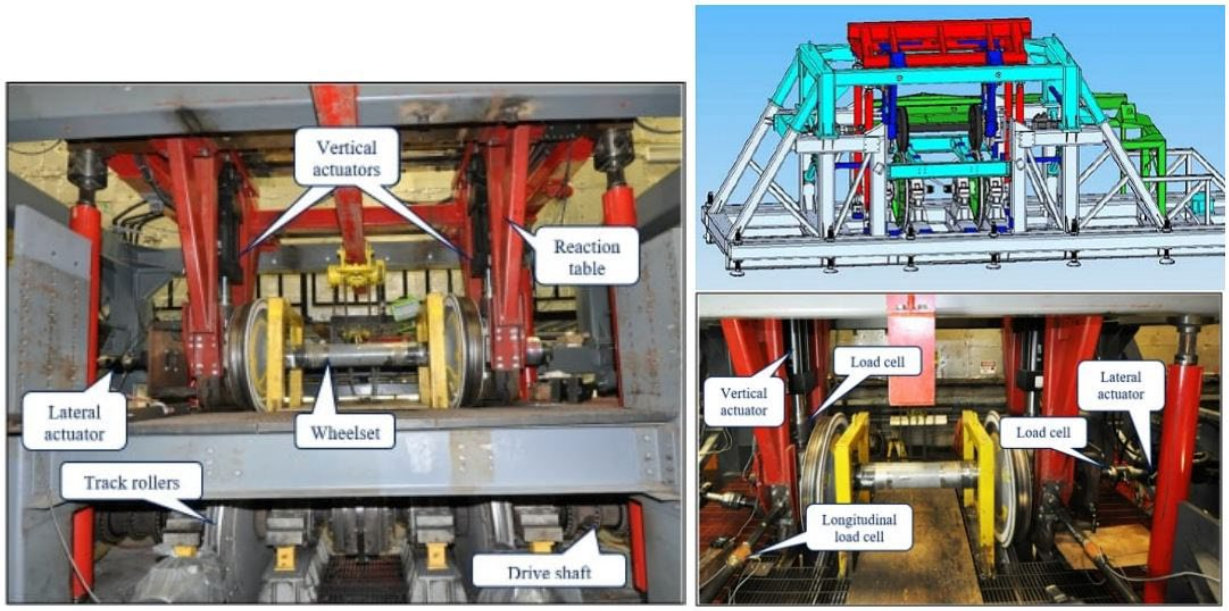

Figure 44. Overview of WBB (NRC Canada, personal communication, 2015)

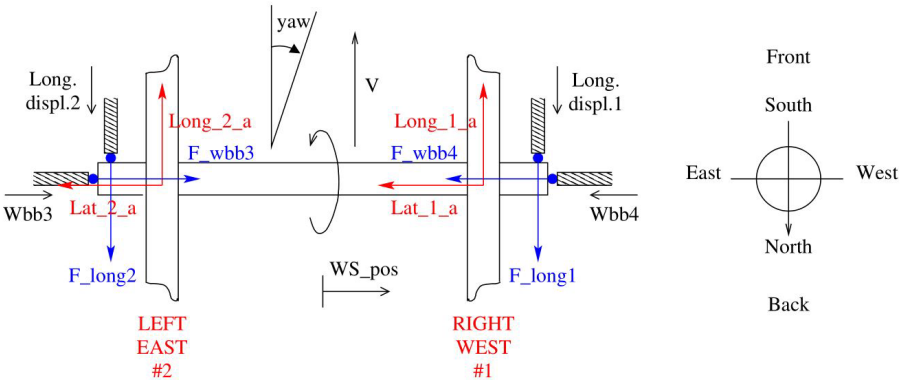

Figure 45. Top view: orientation of the wheelset and the forces acting *on it*

6.1.1 Orientation of the Wheelset

The wheelset position is controlled using six actuators (Figure 45: hatched black rectangles) with corresponding force measurements (load cells, blue circles).

- The blue arrows in Figure 45 indicate the positive forces exerted on the wheelset. For instance, the load cells measure positive for compression such that a positive force in Wbb3 corresponds to a force pushing the wheelset to the west side.
- Wbb1 (west) and Wbb2 (east) are not shown in Figure 45. These push the wheelset down by exerting a vertical force of up to about 153 kN on each side (34,500 lb).
- Actuators Long.displ.1 and Long.displ.2 control the yaw motion of the wheelset. The values reported are the displacements u_{long1}, u_{long2} and the forces F_{long1}, F_{long2} on the wheelset, both positive in north direction.
- Positive yaw is associated with clockwise rotation in a top view, corresponding to a right-hand Cartesian coordinate system with positive x-axis pointing in rolling direction (south), y pointing to the right (west) and z pointing downwards. This corresponds to the coordinate conventions that are used in CONTACT.
- A positive yaw angle is achieved by pushing the wheelset back at the west side ($u_{long1} > 0$) and pulling forward at the east side ($u_{long2} < 0$). The forces exerted on the wheelset are then $F_{long1} > 0$, $F_{long2} < 0$.
- Wbb3 (east) and Wbb4 (west) are lateral actuators. Positive F_{wbb3} and F_{wbb4} mean that the wheelset is pushed sideways as shown in the figure.

An instrumented wheelset is used that measures the contact forces exerted *on* the wheel. The sign conventions are illustrated in red in Figure 45, and illustrated further in Figure 46. This figure shows that the contact position reported by the wheelset is directed opposite to the wheelset overall position "WS_Pos" in Figure 45.

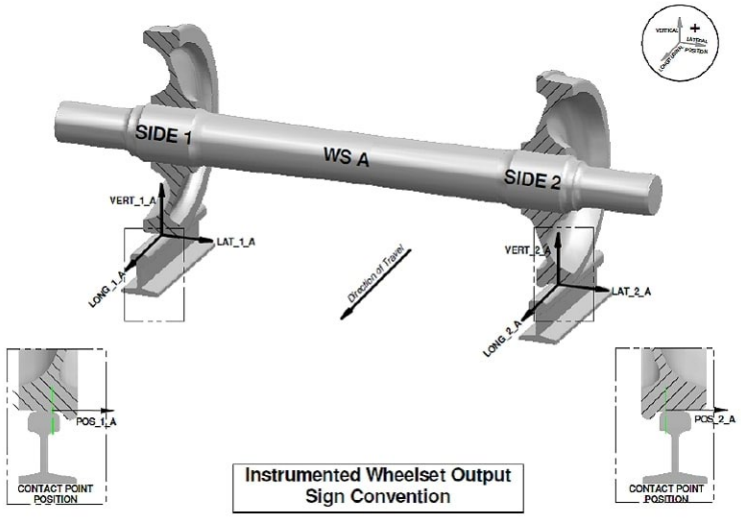

Figure 46. Front view of the instrumented wheelset: wheel #1 is installed at the west side of the WBB (NRC Canada, personal communication, 2015)

The IWS uses a right-handed coordinate system with positive z-direction pointing upwards, contrary to CONTACT. To avoid confusion, the authors use CONTACT's convention throughout. If lateral forces are plotted or discussed, positive values are to the right/east side; similarly, longitudinal forces are positive when directed in positive x-direction. Therefore, $-F_{long1}$, $-F_{long2}$, $-F_{lat1}$, $-F_{lat2}$, $-F_{wbb4}$ are used, with positive orientation in CONTACT's coordinate system; similarly the negative of the contact positions reported by the IWS are taken.

6.1.2 Overview of Scenarios

Data were provided for a total of 38 test runs conducted in July and August 2015. The test runs are divided into four types: dry, wet, TOR, and lube (Figure 47). For each type, measurements are given with rolling velocities $V = 2, 10$, and 30 mph (0.9, 4.5, and 13.4 m/s), and for loadings of $F_z = 34{,}500, 13{,}750$, and 8,750 lb (154, 61 and 39 kN). One measurement is missing: the dry run with 30 mph, 34,500 lb. The wet runs at the highest loading are repeated two times. Each run contains 5–8 minutes of data in 45 channels, sampled with a frequency of 200 Hz.

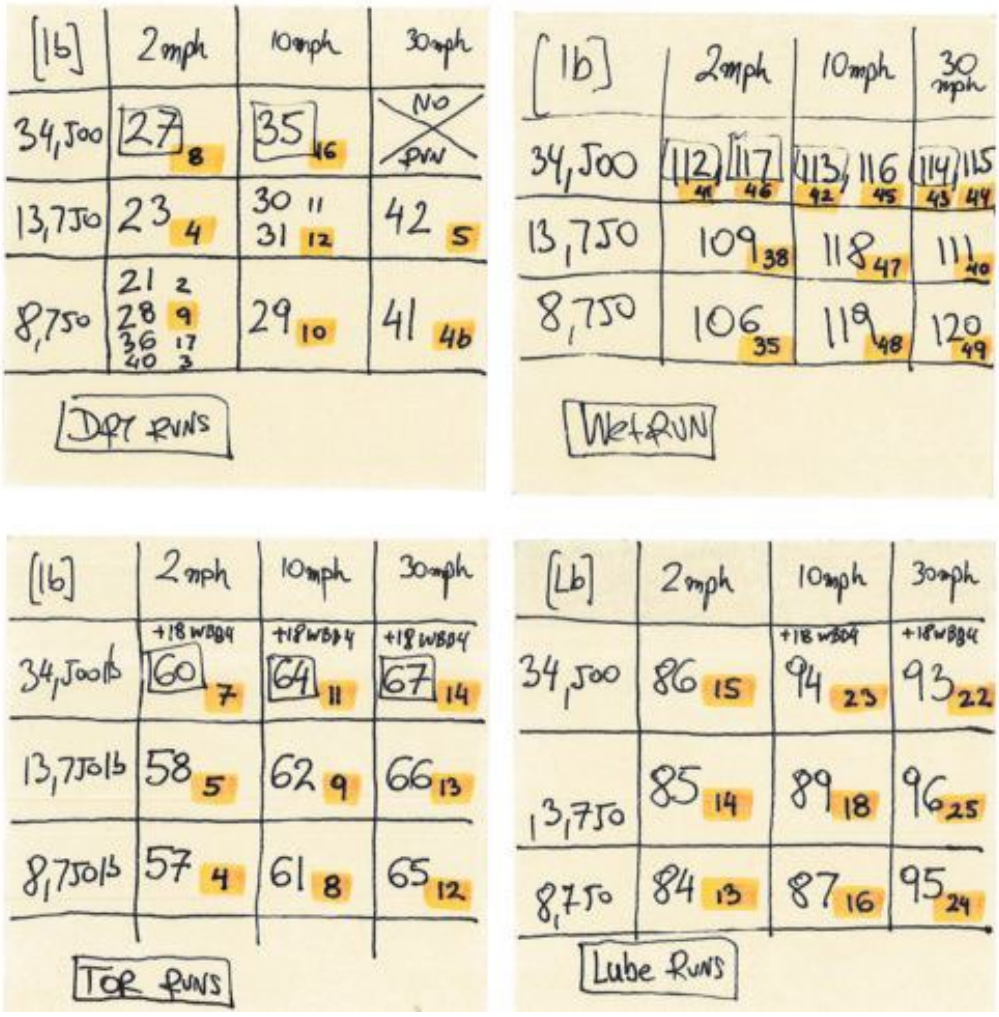

Figure 47. Run numbers for the NRC measurement data, considering the four scenarios at different speeds and vertical force (NRC Canada, personal communication, 2017)

6.1.3 Raw Data for a Run with TOR at 10 mph and 13,750 lbs Load

Figure 48 and Figure 49 show the basic results for one scenario: with TOR, running at 10 mph with vertical load 13,750 lbs.

During each run, the wheelset was constrained laterally by actuators Wbb3 and Wbb4. An initial position was sought with small longitudinal forces, i.e., with equal rolling radii at left and right sides. This put the wheelset in a centered position. During the test, the actuator Wbb3 maintained its position, providing lateral force as required (Figure 48 c). The actuator Wbb4 was set to follow the wheelset with zero force, or with a fixed lateral force in some of the cases at the highest vertical load.

The longitudinal actuators Long.displ.1 and Long.displ.2 were used to force the wheelset into a skewed position. The angle of attack varied gradually, as shown in Figure 48 (a and b), in the range of $[-18,18]$ mrad. The vertical actuators were set to hold the force at the prescribed load on each side (Figure 48 d). This required only slight displacements in the actuators.

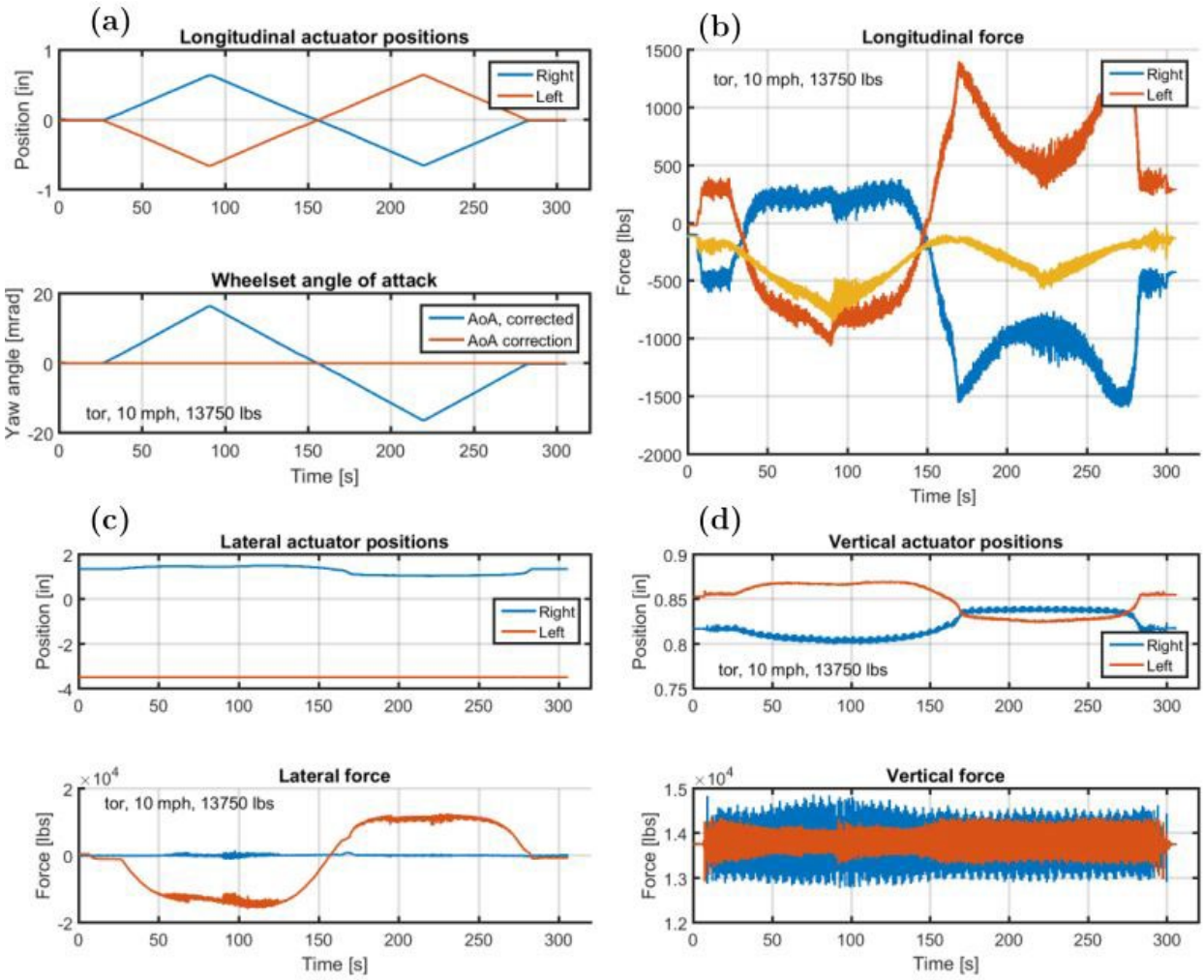

Figure 48. Basic results for run "tor, 10 mph, 13,750 lbs": positions set by the actuators, and corresponding reaction forces (continued in Figure 49)

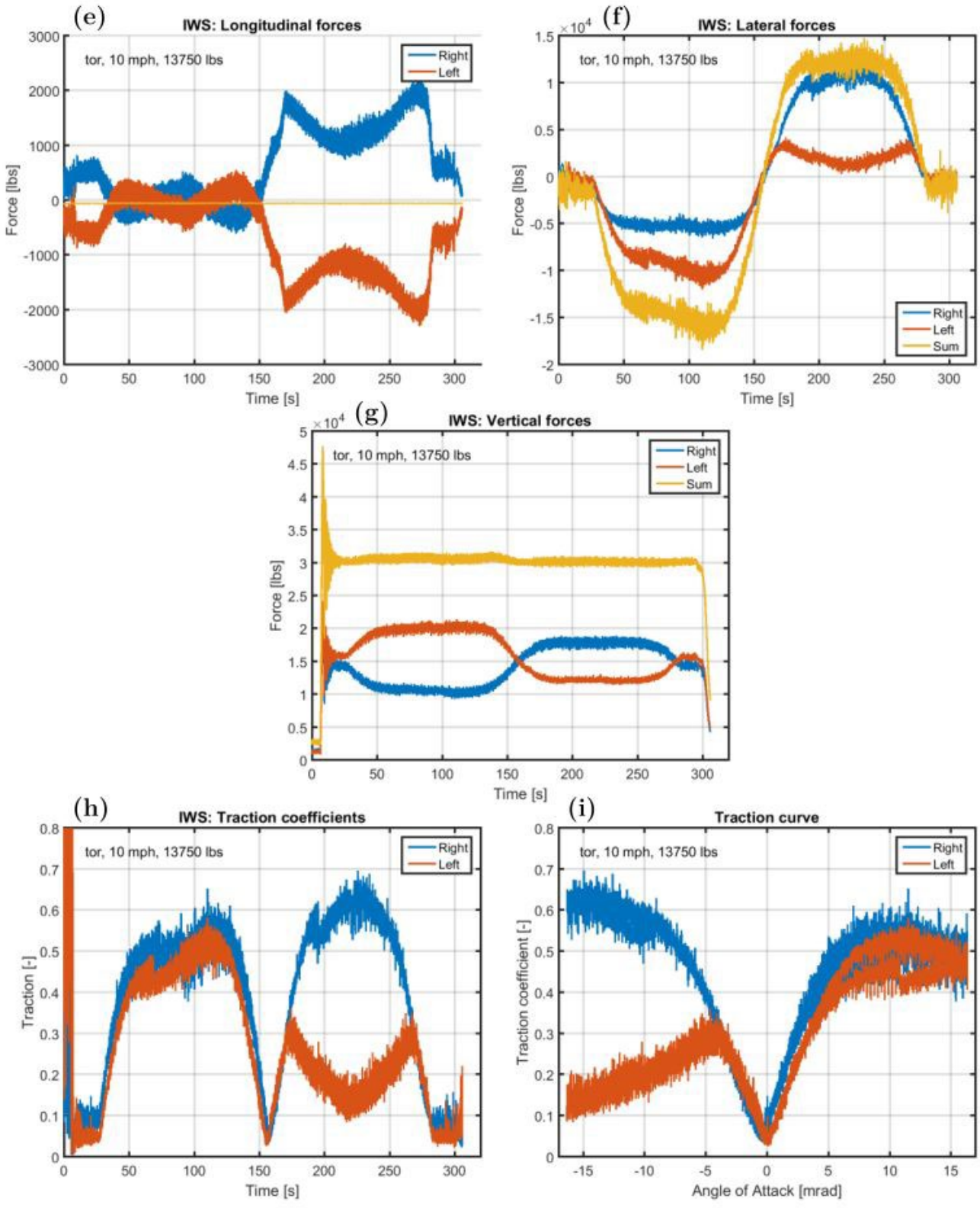

Figure 49. Basic results for run "tor, 10 mph, 13,750 lbs": forces measured by the instrumented wheelset, and corresponding traction coefficients L/V (continued from Figure 48)

The resulting contact forces are measured by the wheelset as shown in Figure 49.

- As the wheelset is rotating freely, the longitudinal forces obtained sum up to zero (Figure 49 e). Small values are found in the first half of the run, bigger values occur at a negative angle of attack (AoA).
- The lateral forces are five times bigger than the longitudinal forces (f). In the first phase, steering to the right ($\psi > 0$), the left wheel shows bigger values. In the second phase, this is reversed.
- The wheelset experiences considerable load shifting between the wheels from the angle of attack changing (g). This compensates for the moments exerted by the lateral contact forces and lateral actuators. At positive ψ, the wheelset steers to the right, and is pushed to the left by the lateral actuators. These act at the axle height, such that the left wheel takes a bigger F_z. This is reversed in the second phase.

  The pattern is asymmetric between the two phases, with F_z increasing more for the left wheel than for the right.
- Traction coefficients are computed using the IWS longitudinal and lateral forces, divided by the vertical force (h). This assumes that the contact angle is small, such that T/N may be approximated as L/V. Values > 0.6 are reached for the right wheel. In the second phase, the values for the left wheel are considerably lower.
- Finally, traction curves are created by plotting the traction coefficients versus the attack angle (i). This shows mostly expected results for the right wheel and for the left at positive AoA, while the pattern for the left wheel at $\psi < 0$ is clearly distinct and unexpected.

6.1.4 Traction Curves for Different Runs

The time series are smoothed using low-pass filtering with a cut-off frequency $f_{low} = 0.15$ (2 mph) or 0.30 Hz (10, 30 mph). The resulting traction curves for the left wheel are shown in Figure 50.

Ideally, the traction coefficients should only depend on the angle of attack. The traction coefficients observed deviate from this in four respects (Figure 51):

1. A (near) zero force is expected at zero angle of attack.
2. The same forces are expected for angle of attack increasing and decreasing.
3. The same forces are expected for positive and negative angle of attack (AoA).
4. The same forces are expected for the left wheel at positive AoA as for the right wheel at negative AoA, and vice versa.

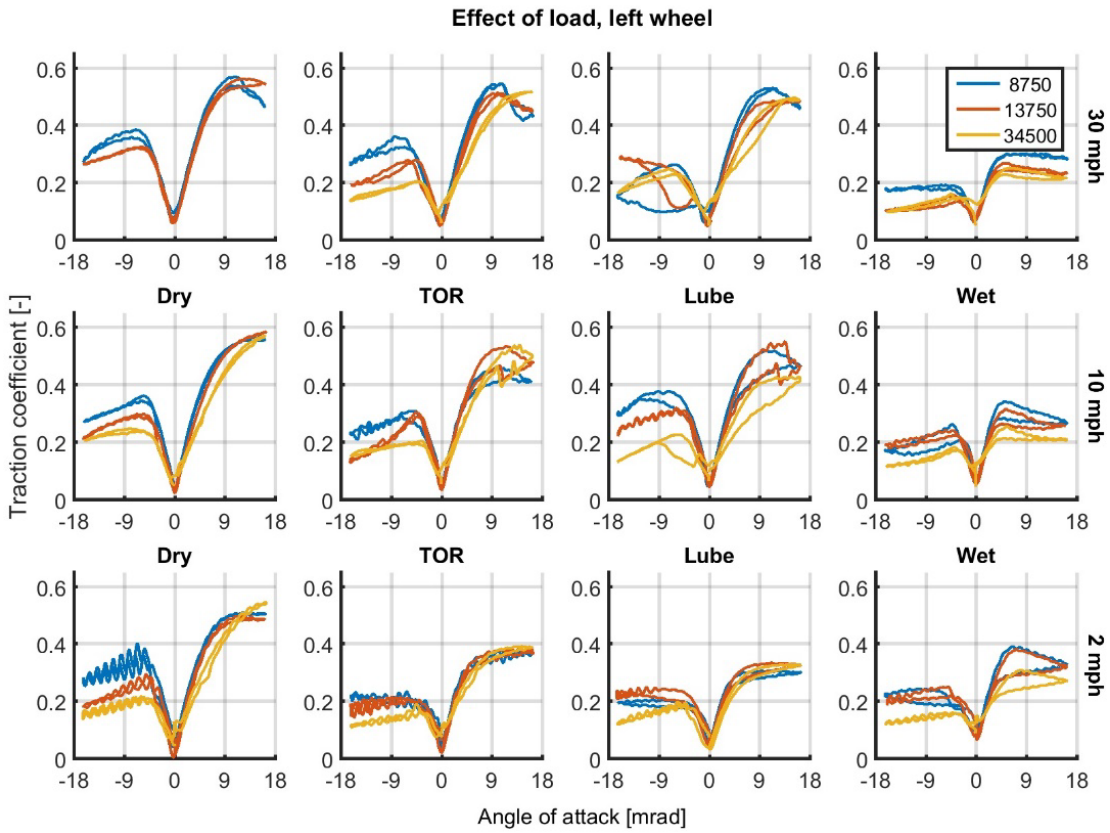

Figure 50. Overview of traction curves obtained on the WBB for different scenarios (dry, TOR, lube, and wet) at different speeds and vertical force

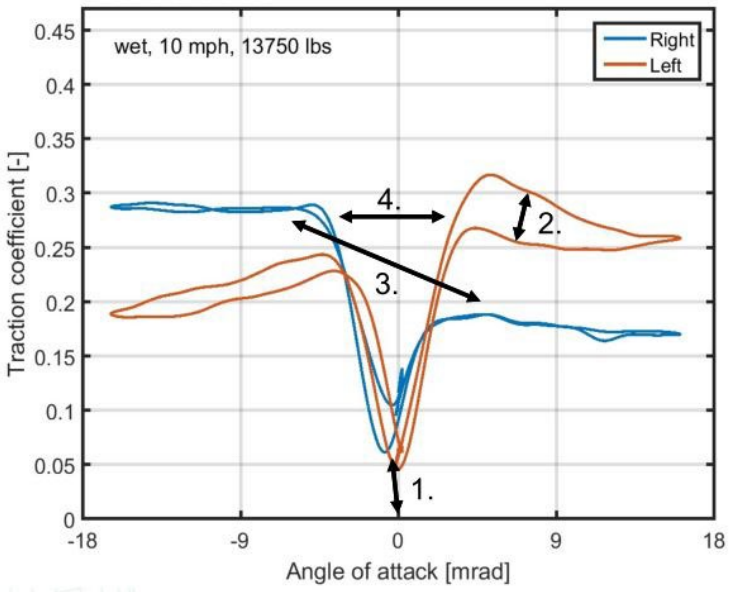

Figure 51. Traction curves obtained for left and right wheels for the wet run at 10 mph and 13,750 lbs vertical load, showing four marked deviations from the expected patterns

6.2 Setting up Balance Equations

The research team used the CONTACT library in MATLAB to simulate a complete measurement run. This requires procedures to identify suitable input parameters.

- The rolling velocity $V = \omega_{rol} r_{rol}$ is given. The pitch velocity ω_{ws} is tuned such that no net moment is exerted on the wheelset in the rolling direction ($M_{y(ws)}$).
- The vertical force is defined by the experiment: $2 \cdot 13{,}750 + 2{,}500$ lbs (two actuators, plus the mass of the wheelset itself). This is distributed over the two wheels as needed to get balanced moments, using the roll angle ϕ_{ws}.
- Lateral forces are introduced by lateral creepage and spin creepage due to the contact angle. These are compensated by lateral forces exerted by the lateral actuators at the height of the wheelset axle. This gives a roll moment about the track center, which is compensated by redistributing the vertical forces over the wheels.
- In the actual measurement, the angle of attack is increased in small increments. This changes the lateral forces and vertical load transfer, affecting the longitudinal forces and pitch velocity.

Each case was characterized by four inputs: the total load $F_{z,tot}$, speed ω_{rol}, lateral position y_{ws}, and attack angle ψ_{ws}. In a steady state, the wheelset has three degrees of freedom: velocity ω_{ws}, vertical position z_{ws}, and roll angle ϕ_{ws}. These unknowns are governed by three balance equations:

$$\text{Angular velocity:} \quad F_{x,lft}^{(2)}\, r_{lft} + F_{x,rgt}^{(2)}\, r_{rgt} = 0 \tag{51}$$

$$\text{Vertical force:} \quad F_{z,lft}^{(1)} + F_{z,rgt}^{(1)} = F_{z,tot} \tag{52}$$

$$\text{Rotation about } x\text{-axis:} \quad \left(F_{z,lft}^{(1)} - F_{z,rgt}^{(1)}\right)\frac{L}{2} - \left(F_{y,lft}^{(2)}\, r_{lft} + F_{y,rgt}^{(2)}\, r_{rgt}\right) = 0 \tag{53}$$

Here, L is the lateral distance between the contact positions ($\approx$ nominal width of the wheelset, distance between tape center lines), r_{lft}, r_{rgt} the rolling radii at the contact positions ($\approx r_{nom}$, the nominal wheel radius).

The forces $F_x^{(2)}, F_y^{(2)}$ used act *on* the wheel set. The forces F_x were measured in wheelset coordinates F_y and F_z and used in the track system.

The team replaced forces $F^{(2)}$ *on* the wheel set by forces $-F^{(1)}$ *on* the rollers. The forces are interpreted as intermediate variables that are non-linear functions of three input variables and six parameters:

$$F_{z,lft}^{(1)} = F_{z,lft}^{(1)}\left(z_{ws}, \phi_{ws}, \omega_{ws}\,;\, L_{ws}, r_{nom}, F_{z,tot}, \omega_{rol}, y_{ws}, \psi_{ws}\right). \tag{54}$$

The balance equations are functions f_i in these non-linear functions F_j:

$$f_1(z_{ws}, \phi_{ws}, \omega_{ws}) = \frac{1}{1000} \cdot \left(F_{x,lft}^{(1)}\, r_{lft} + F_{x,rgt}^{(1)}\, r_{rgt}\right) = 0 \tag{55}$$

$$f_2(z_{ws}, \phi_{ws}, \omega_{ws}) = F_{z,lft}^{(1)} + F_{z,rgt}^{(1)} - F_{z,tot} = 0 \tag{56}$$

$$f_3(z_{ws}, \phi_{ws}, \omega_{ws}) = \frac{1}{1000} \cdot \left((F^{(1)}_{z,lft} - F^{(1)}_{z,rgt}) + F^{(1)}_{y,lft}\, r_{lft} + F^{(1)}_{y,rgt}\, r_{rgt} \right) = 0 \qquad (57)$$

This allows the expression of the Jacobian of $\vec{f}$ in terms of the sensitivities of the contact forces.

$$\vec{f} = \vec{f}_{ref} + \boldsymbol{C} \cdot \boldsymbol{F}\,, \qquad (58)$$

$$\vec{f}_{ref} = \begin{bmatrix} 0 \\ -F_{z,tot} \\ 0 \end{bmatrix}, \qquad (59)$$

$$\boldsymbol{F} = \begin{bmatrix} F^{(1)}_{x,lft} & F^{(1)}_{y,lft} & F^{(1)}_{z,lft} & F^{(1)}_{x,rgt} & F^{(1)}_{y,rgt} & F^{(1)}_{z,rgt} \end{bmatrix}^T, \qquad (60)$$

$$\boldsymbol{C} = \begin{bmatrix} \bar{r}_{lft} & 0 & 0 & \bar{r}_{rgt} & 0 & 0 \\ 0 & 0 & 1 & 0 & 0 & 1 \\ 0 & \bar{r}_{lft} & \bar{L}/2 & 0 & \bar{r}_{rgt} & -\bar{L}/2 \end{bmatrix}, \qquad (61)$$

$$\boldsymbol{J}_f = \begin{bmatrix} \frac{\partial f_1}{\partial z_{ws}} & \frac{\partial f_1}{\partial \phi_{ws}} & \frac{\partial f_1}{\partial \omega_{ws}} \\ \frac{\partial f_2}{\partial z_{ws}} & \frac{\partial f_2}{\partial \phi_{ws}} & \frac{\partial f_2}{\partial \omega_{ws}} \\ \frac{\partial f_3}{\partial z_{ws}} & \frac{\partial f_3}{\partial \phi_{ws}} & \frac{\partial f_3}{\partial \omega_{ws}} \end{bmatrix} = \boldsymbol{C} \cdot \boldsymbol{J}_F\,, \qquad (62)$$

$$\boldsymbol{J}_F = \begin{bmatrix} \partial F^{(1)}_{x,lft}/\partial z_{ws} & \partial F^{(1)}_{x,lft}/\partial \phi_{ws} & \partial F^{(1)}_{x,lft}/\partial \omega_{ws} \\ \partial F^{(1)}_{y,lft}/\partial z_{ws} & \partial F^{(1)}_{y,lft}/\partial \phi_{ws} & \partial F^{(1)}_{y,lft}/\partial \omega_{ws} \\ \partial F^{(1)}_{z,lft}/\partial z_{ws} & \partial F^{(1)}_{z,lft}/\partial \phi_{ws} & \partial F^{(1)}_{z,lft}/\partial \omega_{ws} \\ \partial F^{(1)}_{x,rgt}/\partial z_{ws} & \partial F^{(1)}_{x,rgt}/\partial \phi_{ws} & \partial F^{(1)}_{x,rgt}/\partial \omega_{ws} \\ \partial F^{(1)}_{y,rgt}/\partial z_{ws} & \partial F^{(1)}_{y,rgt}/\partial \phi_{ws} & \partial F^{(1)}_{y,rgt}/\partial \omega_{ws} \\ \partial F^{(1)}_{z,rgt}/\partial z_{ws} & \partial F^{(1)}_{z,rgt}/\partial \phi_{ws} & \partial F^{(1)}_{z,rgt}/\partial \omega_{ws} \end{bmatrix}. \qquad (63)$$

The lengths $\bar{r} = r/1000$ and $\bar{L} = L/1000$ are scaled for easier interpretation of printed values, making the components of $\vec{f}$ the same order of magnitude. Note that C is not truly constant but depends on the contact positions via $\bar{r}$. The team assumed there was only one contact patch; in case of multiple patches, they use averaged values.

Two contact problems are defined for left and right wheels, using CONTACT's Module 1 for wheel/rail contact, with steady rolling, prescribed position z_{ws}, ϕ_{ws}, and velocity ω_{ws} (N = 0, F = 0). The material parameters are $G = 82{,}000, \nu = 0.28$. The research team first used Coulomb friction, with μ to be calibrated. Initial estimates for z_{ws} and ϕ_{ws} were sought using frictionless problems with prescribed $F_z = F_{z,tot}/2$.

Broyden's algorithm was used to solve Equations 55 to 57. A simple alternative is to use the Gauss-Seidel approach: first change z_{ws} to get the correct total force, change ϕ_{ws} to correct the distribution, change ω_{ws} to find free rolling, and then return to z_{ws} in order to correct for the changes in F_z due to ϕ_{ws} and ω_{ws}.

6.3 Detailed Analysis of One Scenario

6.3.1 Uncertainty on the Wheelset Lateral Position

One of the smoothest runs was selected for further investigation: dry, 10 mph, 13,750 lb. The dimensions of the wheels, wheelset, roller, etc. were set in an input-file to CONTACT. Profiles were measured between different types of measurements, pre-dry, post-dry, post-TOR, etc. These showed a little wear at the tread of the wheels. After alignment and smoothing, a facet appeared on the left roller at $1:30$ inclination, while the tread of the wheel is at $1:20$.

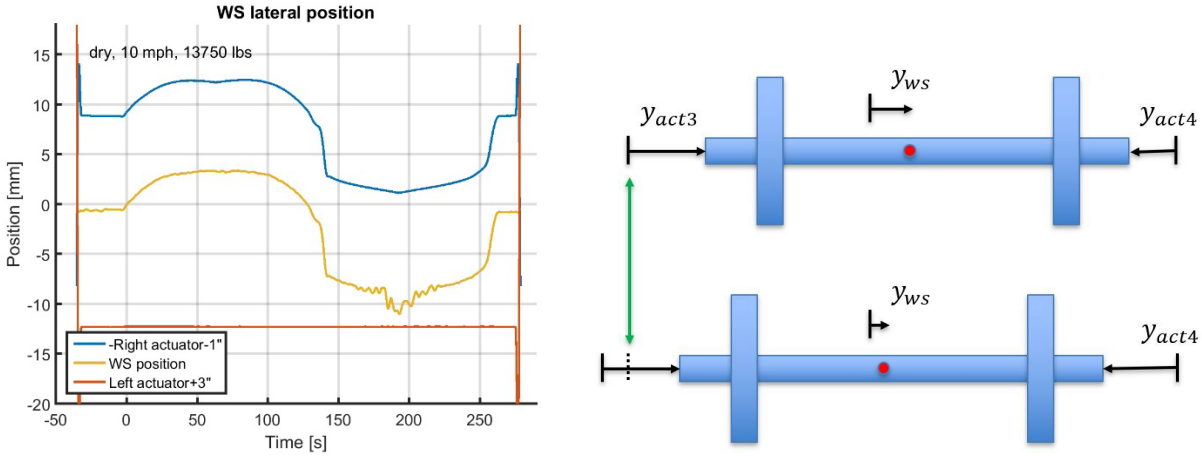

Figure 52. Left: measurements on the wheelset lateral displacement showing displacements of 10–15 mm, right: possible effects of flexibility in the WBB frame

There was considerable uncertainty about the lateral wheelset position during the test. This was measured using an ultra-sonic position sensor facing the back of one wheel, showing displacements of 10–15 mm during the run (Figure 52, left), while < 0.5 mm was expected from the yaw angle. Likewise, the position of the right actuator should vary no more than 0.5 mm, while changes of 10–15 mm were reported. These results are explained by flexibility in the WBB frame (Figure 52, right), which allowed the total distance of actuators plus wheelset to change over time.

The right actuator detected the widening of the frame; the left actuator was held at a fixed position with respect to the frame. This occurred in a consistent fashion in different test runs, as shown in Figure 53. The flexibility appeared to respond to the lateral force, with different rates at different force levels. This shows that the wheelset does not remain centered during the test but moves to one side. This partially explains the asymmetries in the measured traction curves.

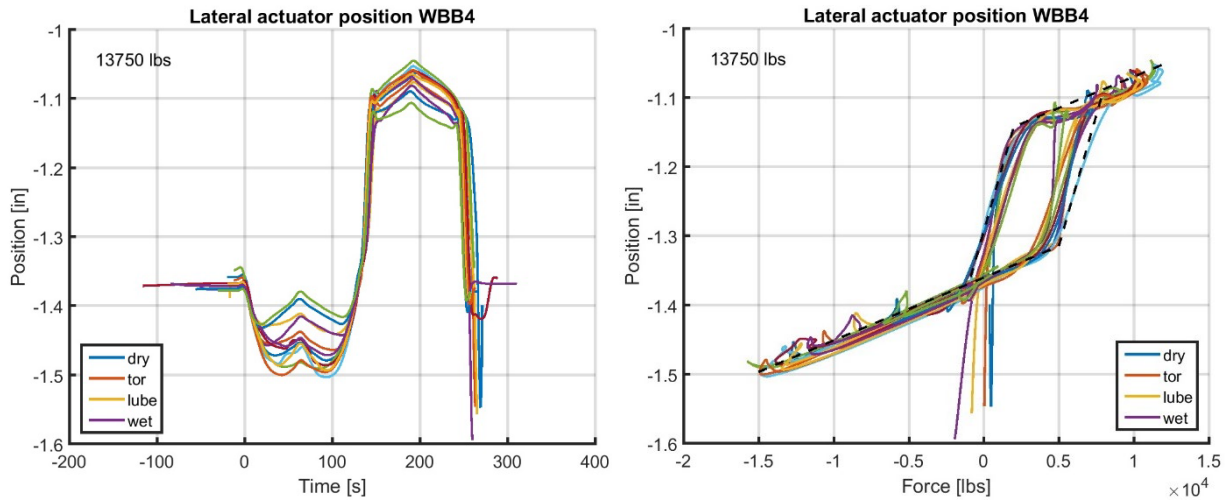

Figure 53. Flexibility in the WBB frame, left: actuator position versus time, right: actuator position versus sum of lateral forces

6.3.2 Effects of a Second CONTACT Patch

A small test was conducted with CONTACT to explore the effects of the lateral position. This focused on the left wheel and roller with vertical force held fixed at $F_z = 50$ kN. The wheelset was steered to the left at yaw angles $\psi_{ws} = -14$ to -18 mrad, and shifted to the left by -5 to -8 mm. A second contact patch arose in this range of lateral positions (Figure 54, left), carrying more of the load if the wheelset was shifted further.

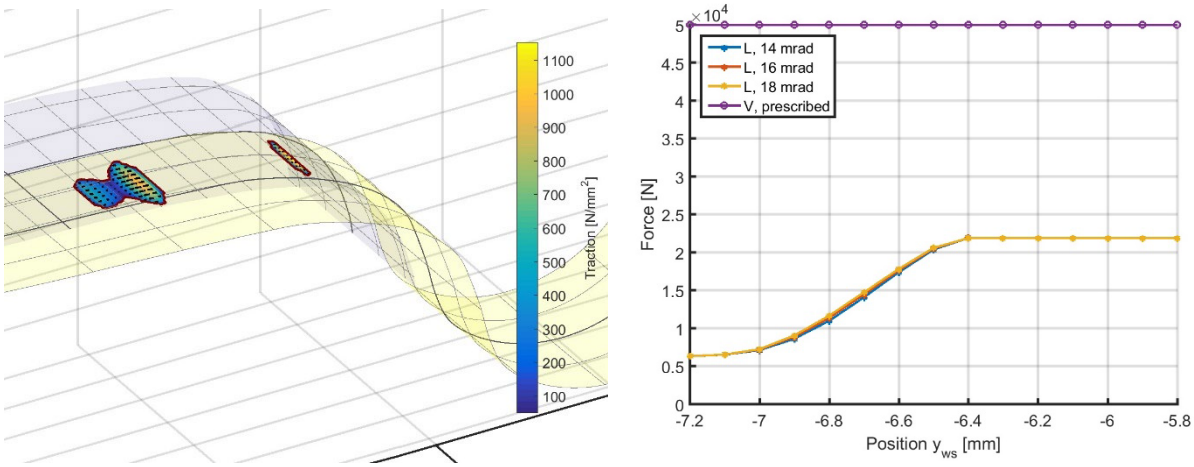

Figure 54. Results for a theoretical test in which a second contact patch arises, showing *L*-force decreasing with increasing lateral displacement

In the configurations considered, tangential forces on the wheel are negative, carrying part of the vertical load. Assuming full sliding, $T = \mu N$,

$$\begin{bmatrix} L \\ V \end{bmatrix} = \begin{bmatrix} \cos(\delta) & -\sin(\delta) \\ \sin(\delta) & \cos(\delta) \end{bmatrix} \cdot \begin{bmatrix} T \\ N \end{bmatrix}, \qquad \frac{L}{V} = \frac{\mu\cos(\delta) - \sin(\delta)}{\mu\sin(\delta) + \cos(\delta)} \tag{64}$$

The primary CONTACT patch has a contact angle of $\delta_1 = 2.9°$, while the second patch has $\delta_2 = 19°$. At $\mu = 0.5$ this gives a four-fold reduction of L/V, from 0.44 to 0.115, as confirmed in Figure 54, right.

This phenomenon explains the lower traction coefficients found at the left wheel at negative AoA values of Figure 49 and Figure 50.

6.3.3 Calibration of the Input Data

The uncertainty of the lateral wheelset position relative to the rollers was resolved by manual calibration. Further uncertainties in the input were also considered:

- The COF
- The thickness and strength of the interfacial layer
- The precise profiles, inclination 1: 20 or 1: 30
- The precise gauge, resulting from flexibilities in the structure

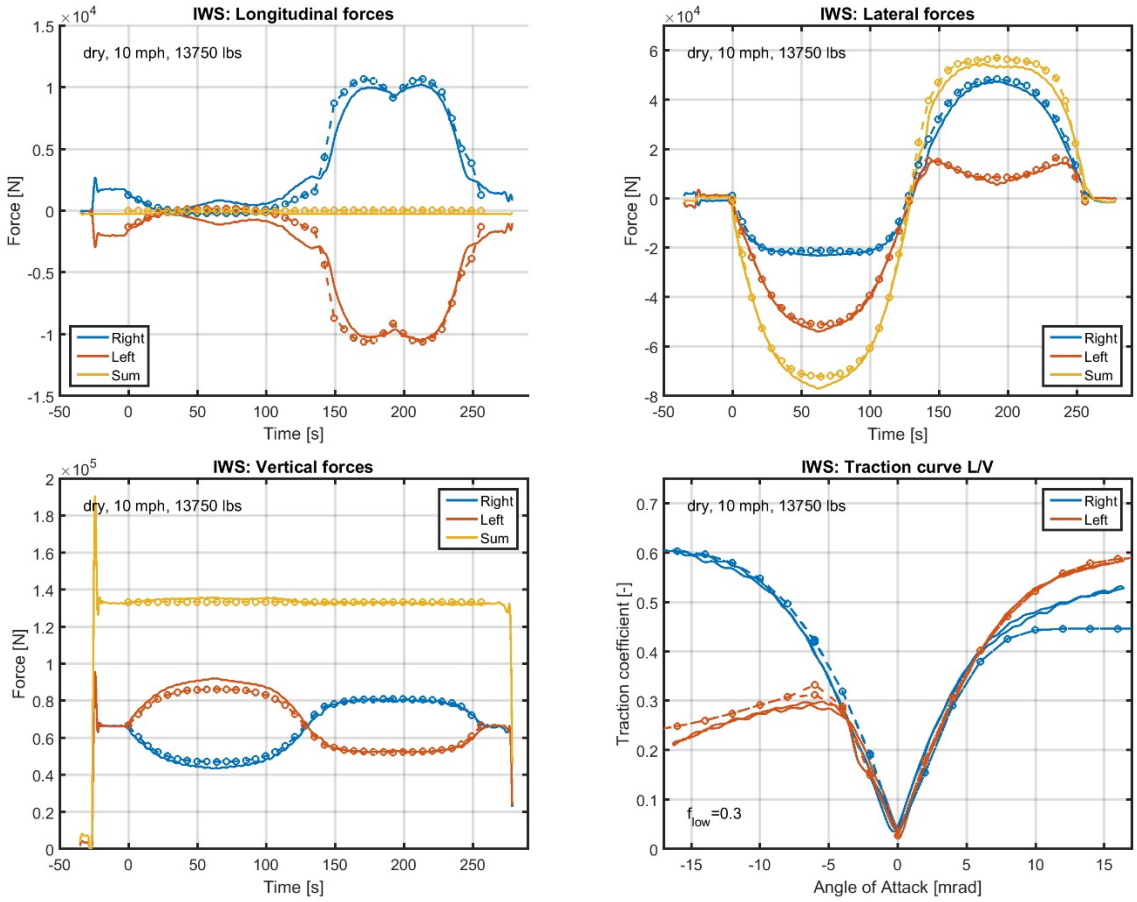

Figure 55. Measured and computed forces for the scenario "dry, 10 mph, 13,750 lbs" after calibration

After calibration of the input variables, the simulation results capture the main features of the measurement data as shown in Figure 55:

1. Load transfer between the left and right wheels
2. Rolling radius difference: longitudinal creepage and creep force
3. Lowering of lateral force at the left wheel

Three of the asymmetries of Figure 51 were reproduced in the simulation results:

1. Non-zero L/V at zero AoA
3. Different L/V for positive and negative AoA
4. Different L/V for left and right wheels

These are due to offsets in the lateral wheelset position, plotting L/V instead of T/N, and asymmetries in the wheel and roller profiles between left and right wheels. The last asymmetry, different L/V for AoA increasing or decreasing, could not yet be reproduced.

6.4 Conclusion Regarding NRC's Measurements

This section described the measurements provided by NRC Canada for dry, wet, lubricated, and TOR conditions. These measurements concern a full-scale instrumented wheelset placed on top of two rollers in a centered position, then yawed to produce lateral creepage, measuring the creep forces.

Analysis of the measurement data exposed deviations from the intended setup. Displacements of 10–15 mm were found between the different arms of the WBB structure, attributed to flexibilities incurred from the loads on the structure. This flexibility introduced considerable uncertainty on the lateral wheelset position with respect to the rollers, which is a primary input to the wheel-rail contact situation.

After calibration of the uncertain inputs for a single run, a reasonable correspondence was achieved between measurements and simulation. However, the calibration was labor-intensive as no algorithm has yet been found for its automation. Further, the match remains somewhat incomplete, particularly concerning the role of AoA increasing or decreasing. In the present form, the measurement data are not well fit for the validation of detailed contact models. Improvements could be sought in the measurement collection, completing the data, or in automated algorithms for the calibration, for the reconstruction of missing pieces of information.

7. Integration in VTI Software

One of the difficulties in detailed contact modeling lies in the interaction of wheel-rail contact forces with the surrounding system. For instance, the attitude of a wheelset in a curve arises as a result of the contact forces, yet the computation of the forces requests that an attitude is prescribed beforehand. This difficulty may be resolved by including detailed models in VTI software, bringing the models closer to the practitioners in the field. This is facilitated in the current project by provisional integration of the library version of CONTACT in multi-body simulation. Pre-existing versions of CONTACT in GENSYS and Universal Mechanism have been extended, and new prototypes have been realized for CONTACT in NUCARS and SIMULIA Simpack. Finally, a preliminary study was conducted on the integration of CONTACT in VAMPIRE, but this was stopped when it seemed that the VAMPIRE software would not be developed further. Here, the authors quickly describe the outcomes of these works.

7.1 The CONTACT Library Version

The computational part of CONTACT can be interfaced with other programs and directed from the CONTACT library, illustrated schematically in Figure 56. The library is a dll (Windows) or shared object file (Linux) that provides a well-defined interface. This interface is interoperable between Fortran and C/C++ and can further be accessed from MATLAB and Python.

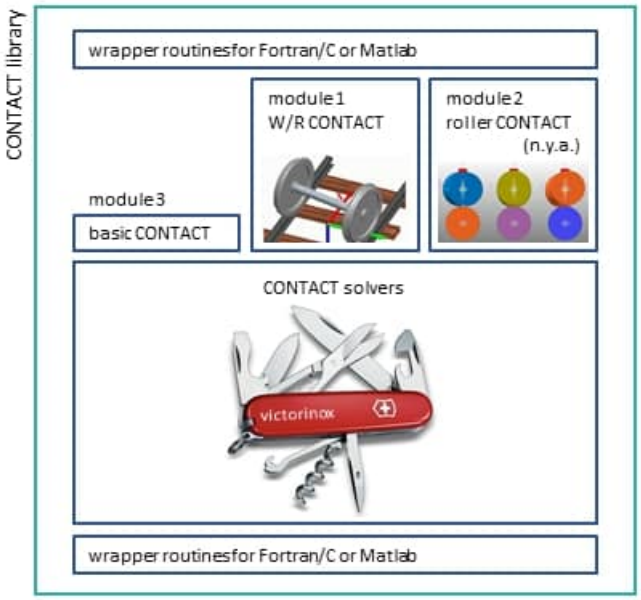

Figure 56. Software architecture for the CONTACT library (Vollebregt, 2019a)

CONTACT is built using different "modules" (sub-programs) that use a shared computational core. These modules are targeted to different use-cases, requiring different analyses to arrive at the basic contact problem. Module 1 is targeted at wheel-rail contact analysis. It starts from a wheelset at a given track location, using generic wheel and rail profiles, locates the contact points, solves the contact patches, and then converts the results to the global coordinate frame (Vollebregt, 2022). Module 3 is the driver for generic Hertzian and non-Hertzian contact problems. This provides more flexibility to the user but places the burden of the contact location on the user, requiring them to prepare the basic inputs in the appropriate form.

The library is set up to compute the evolution of multiple contact problems which can be grouped in different ways. Most data are configured and stored separately for each contact problem, which is solved independently, using its own internal data and possibly its own previous state. Memory requirements and computing time are proportional to the number of stored contact problems and the desired grid resolution. Parallel computing is supported, allowing multiple contact problems for different wheels to be solved at the same time.

As an example of the interface routines, we consider the method to configure a wheel or a rail profile. In MATLAB, this method is defined as follows:

```
%-------------------------------------------------------------------------------------------------
% function [ ] = cntc_setprofileinputfname(ire, fname, iparam, rparam)
%
% set a wheel or rail profile filename for a wheel-rail contact problem (version 19.2)
%
%  fname          - string: name of profile file
%  iparam         - integer configuration parameters
%                     1: itype     0 = rail, 1 = wheel profile, -1 = taken from file extension
%                     2: iside     0 = left, 1 = right, 2 = both wheels or rails
%                     3: mirrory   0 = no mirroring, 1 = mirror y coordinate values
%  rparam         - real configuration parameters
%                     1: sclfac    scaling factor for conversion to [mm], e.g. 1e3 for data
%                                  given in [m]
%                                  default (sclfac<=0): using the active unit convention
%                     2: smooth    smoothing parameter for spline representation, >=0,
%                                  0=no smoothing
%-------------------------------------------------------------------------------------------------
```

Additional parameters are needed in Fortran or C, to communicate the lengths of arrays used:

```
!-------------------------------------------------------------------------------------------------
subroutine cntc_setProfileInputFname(ire, c_fname, len_fname, nints, iparam, nreals, rparam)
   use, intrinsic        :: iso_c_binding, only: c_char
   integer,                intent(in) :: ire          ! result element ID
   character(kind=c_char), intent(in) :: c_fname(*)   ! C-string: name of profile file
   integer,                intent(in) :: len_fname    ! length of filename
   integer,                intent(in) :: nints, nreals
   integer,                intent(in) :: iparam(nints)
   real(kind=8),           intent(in) :: rparam(nreals)
end subroutine cntc_setProfileInputFname
!-------------------------------------------------------------------------------------------------
```

In Fortran, the use of this routine looks as follows:

```
      ! set rail profile for left and right sides

      f_fname   = 'profiles/MBench_UIC60_v3.prr'
      c_fname   =     trim(f_fname)  // C_NULL_CHAR
      len_fname = len(trim(f_fname))
```

```
itype   = -1      ! using filename extension, prr == Simpack format
iside   =  2      ! left and right rails
mirrory =  0      ! no mirroring
sclfac  = 1d0     ! already in [mm], no scaling
smooth  = 0d0     ! no smoothing
iparam  = (/ itype, iside, mirrory /)
rparam  = (/ sclfac, smooth /)

call cntc_setProfileInputFname(iwhe, c_fname, len_fname, 3, iparam, 2, rparam)
```

A complete description of the CONTACT library is provided in the user guide (Vollebregt, 2019a). The interface is specified in detail in the MATLAB wrapper functions (`matlab_intfc`) and in the Fortran interface file `contact_addon.ifc`.

7.2 Integration of CONTACT in Universal Mechanism

The Universal Mechanism software (UM; www.universalmechanism.com) has been under development at Bryansk State Technical University (Russia) since the end of the 1980s. UM is a general-purpose MBS software, and the simulation of rail vehicle dynamics is one of the main directions for the program's practical usage. Typical railway models are shown in Figure 57.

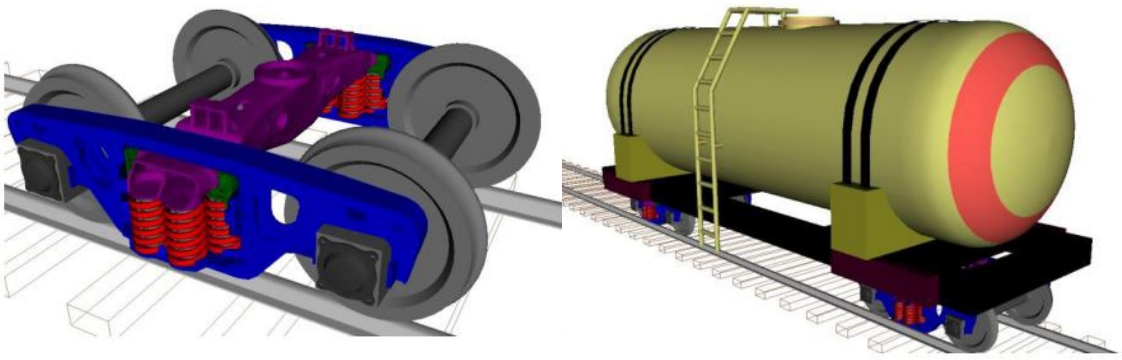

Figure 57. Typical models of railway vehicles created in UM (Rodikov & Vollebregt, 2018)

The UM software provides a wide range of techniques and tools for rail vehicle and train dynamic simulation. This requires accurate simulation of wheel/rail contact forces. Algorithms implemented in UM include the Hertz contact theory, the FASTSIM algorithm, the model by Piotrowski and Kik (2008) and the interface to the CONTACT library by Kalker and Vollebregt. This latter interface was made in cooperation with VORtech CMCC.

The CONTACT add-on for UM is the version of CONTACT that is integrated seamlessly into Universal Mechanism. This provides the option to simulate vehicle dynamics using CONTACT's detailed algorithms, including the full non-Hertzian geometry (instead of relying on Hertzian theory or the Kik-Piotrowski algorithm) and using full linear elasticity instead of FASTSIM simplified theory. The CONTACT add-on is included in the dynamic integration loop. It completely replaces the simplified algorithms.

The first version of the CONTACT add-on to UM was established in 2016, using Module 3 for basic contacts, with geometric analyses programmed at the side of UM. A new interface was

established during the current project, using Module 1 with CONTACT's geometry processing routines for wheel-rail contact processing. The new version was tested using a model of an AC4 rail vehicle and a moving track model as discussed by Rodikov and Vollebregt (2018). One representative outcome of this is shown in Figure 58.

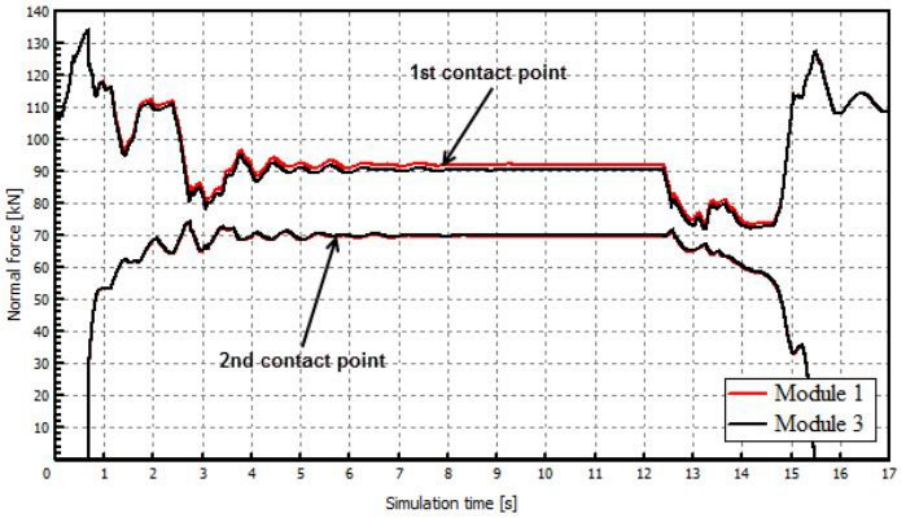

Figure 58. The normal forces computed using the CONTACT add-on in UM, at first and second contact points, left wheel of the first wheelset (Rodikov & Vollebregt, 2018)

Table 5. Results of performance measurements for CONTACT in UM for different scenarios (Lei Qiang, personal communication, 2019)

	Wheelset (6 dof) tangent, no irreg. 10 s, 20 km/h	Vehicle (50 dof) curve, irreg. 20 s, 300 km/h	Train (400 dof) curve, irreg. 20 s, 300 km/h	Train-bridge (548) tangent, irreg. 5 s, 300 km/h
Total CPU-times (s)				
Hertz + FASTSIM	0.67	17.36	360.9	764.5
Kik-Piotrowski	3.67	25.97	475.0	824.1
CONTACT	72.88	383.0	4265.	2048.
Relative times compared to Hertz + FASTSIM (-)				
Kik-Piotrowski	5.5	1.5	1.3	1.1
CONTACT	108.6	22.1	11.8	2.7

Lei Qiang of Tongsuan Technology Co., Ltd. conducted further performance testing using four different scenarios with and without track irregularities. The total computing times were determined for three different methods as shown in Table 5. The total computing times ratios were found to be 2.7 to 109 for CONTACT compared to Hertz + FASTSIM and 2.5 to 20 compared to Kik-Piotrowski. These results show that the relative performance of CONTACT is improved by increasing the number of degrees of freedom in the system.

7.3 Integration of CONTACT in GENSYS

GENSYS (`www.gensys.se`) is a software tool for modeling vehicles running on rails, under development by Ingemar Persson of AB DEsolver since 1992. Contacts were established in 2015, upon which a first coupling called `creep_contact_1` was realized in GENSYS. This is based on CONTACT's Module 3 for basic contacts, relying on GENSYS' contact geometry and

creep calculations. This coupling and others were used for locomotive studies (Spiryagin, et al., 2017). A second coupling, `creep_contact_6`, has been created in the context of the current work, based on Module 1 for wheel/rail contacts.

Table 6. Test cases used to evaluate the couplings `creep_contact_1` and `creep_contact_6` in GENSYS (I. Persson, 2019)

Test name	Wheel profile	Type of creepage	Comments
axl_110	Cylindric	No creepage	Pure rolling
axl_111	Cylindric	Pure longitudinal	Pitch angle velocity increasing linearly
axl_112	Cylindric	Pure lateral creepage	Angle of attack increases linearly
axl_113	Cylindric	Pure spin creepage	Wheelset rotates in yaw around right wheel
axl_120	Conical	Pure spin creepage	Pure rolling
axl_121	Conical	Longitudinal & spin creepage	Pitch angle velocity increases linearly
axl_122	Conical	Lateral & spin creepage	Angle of attack increases linearly

The new version was tested in detail using seven straightforward test-cases, with flat and conical wheels on a circular rail and fully prescribed motion (Table 6). This allows the contact positions and creepages to be computed by hand to validate the numerical computations. Detailed results of the tests are reported by I. Persson (2019) and a representative example is shown in Figure 59.

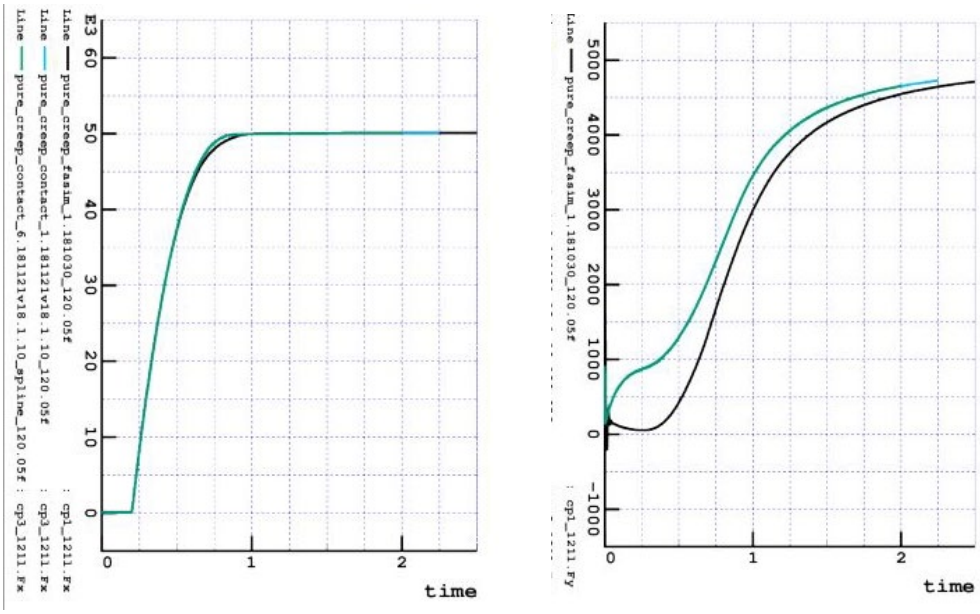

Figure 59. Longitudinal (left) and lateral forces (right) computed for axl_121 with conical wheel profiles, wheelset spinning, and longitudinal and spin creepage (I. Persson, 2019)

The results of the two new couplings are checked in two different ways. The first comparison considers the creep forces calculated by `creep_contact_1` and those obtained from FASTSIM. Reasonable agreement is reached in all scenarios.

1. This shows that all unit and sign conventions are used correctly.
2. The remaining differences are due to the different theories used. These are found mainly in the presence of spin creepage.

The second comparison considers `creep_contact_1` and `creep_contact_6`. Geometric analysis was done by GENSYS in the former; in the latter, CONTACT does the same. Excellent agreement is reached, validating CONTACT's new contact geometry and creep calculations.

7.4 Integration of CONTACT in NUCARS

The NUCARS program is software for vehicle-track dynamic interaction, under development since 1986. NUCARS provides different options for contact modeling, including fully nonlinear contact calculations based on Kalker's USETAB program (Kalker, 1996).

The team developed a prototype version of NUCARS including the CONTACT library (Shu, 2018). This works by loading the library into NUCARS, setting up control flags and model parameters. At each integration step, the program updates the wheel/rail contact point locations and creepages, calculating contact ellipses using standard NUCARS methods and calling CONTACT (Module 3) for the creep force calculation.

The results were checked using a four-axle freight car (Figure 60) with AAR1B wheel and AREMA 136 rail profiles, in a 10 degree curve ($R = 175$ m) with perturbations (Figure 61), running at 15 mph (24 km/h) over 700 ft (213 m) distance. Good correspondence was found between CONTACT and USETAB, as illustrated by the L/V ratios shown in Figure 62. Differences may have been caused by the grid discretization used; fine resolution (0.2 mm) was used in the CONTACT dll.

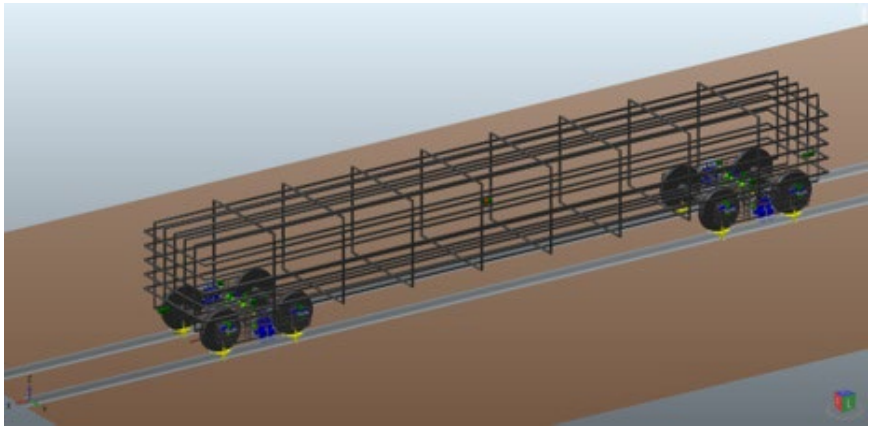

Figure 60. Four-axle freight car modelled in NUCARS (Shu, 2018, p. 5)

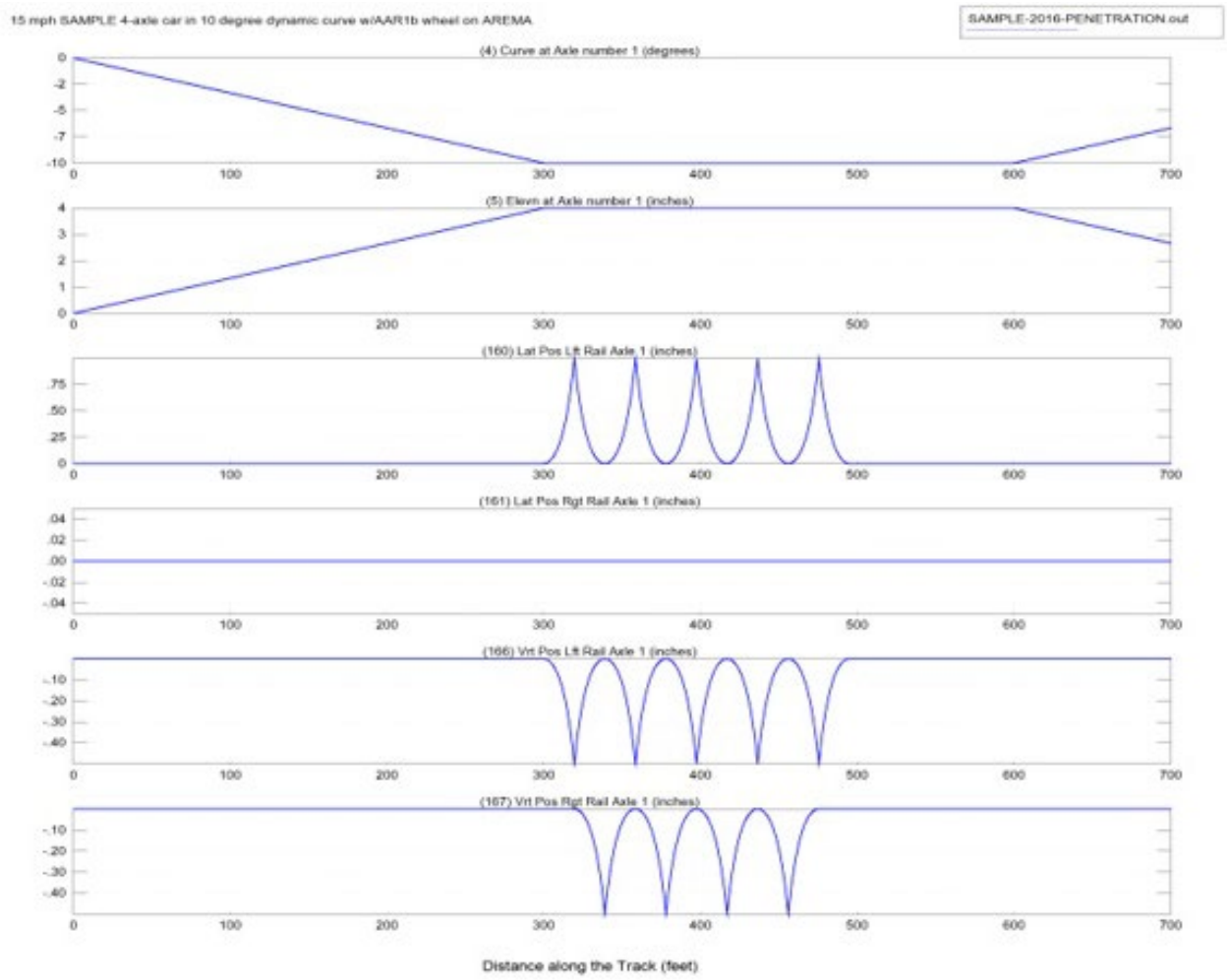

Figure 61. Dynamic curving geometry used in the NUCARS test model, top to bottom: curvature (deg), elevation, left/right rails lateral, and left/right rails vertical deviation (Shu, 2018)

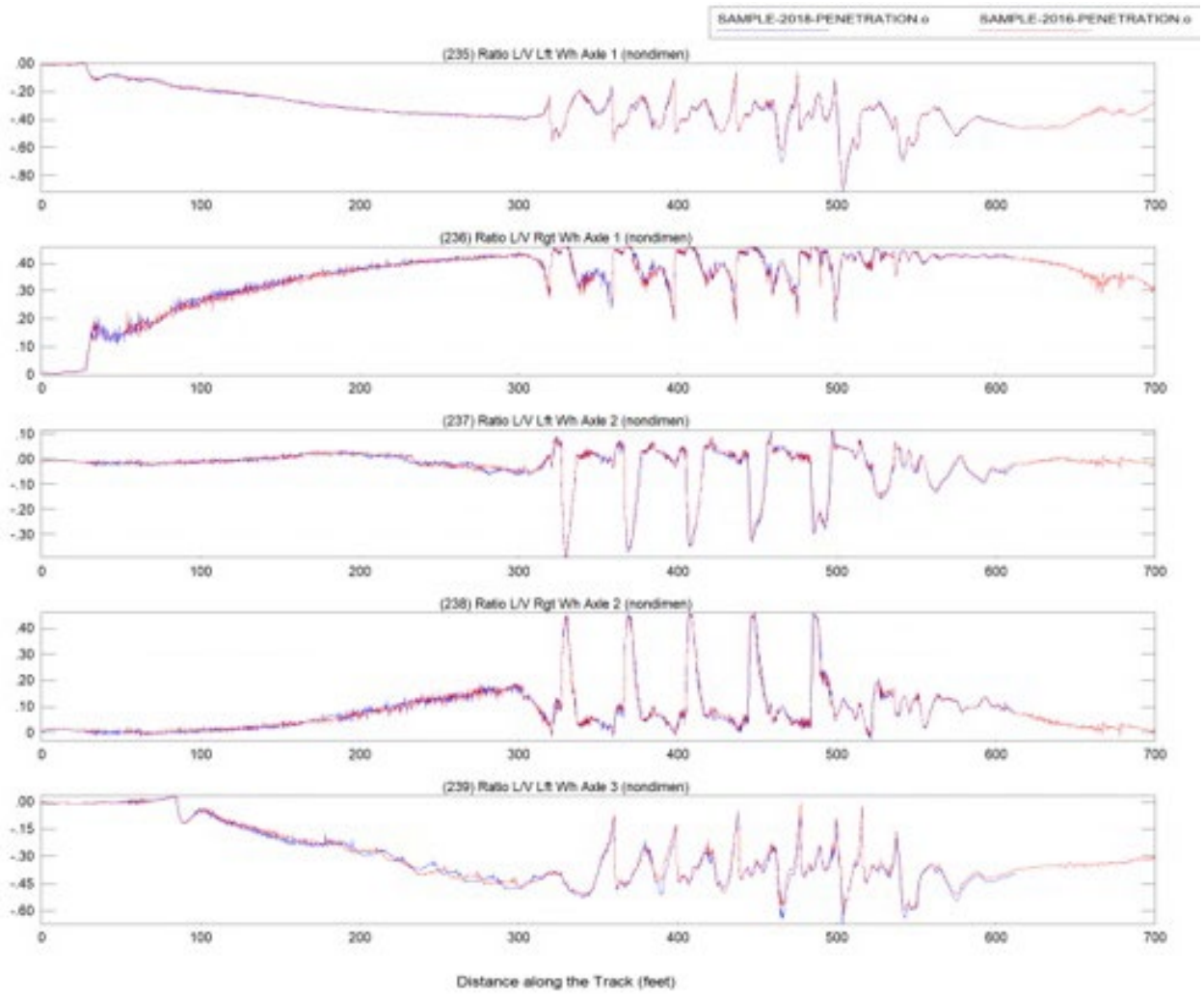

Figure 62. Comparison of L/V ratios on left/right wheels on three axles between NUCARS using USETAB and using the CONTACT dll (Shu, 2018)

This work demonstrated that the CONTACT library can be linked and used online in NUCARS simulations. It provides an alternate method for calculating wheel/rail creep forces suited for a wider range of contact conditions. As previously stated, the geometrical analysis is based on the pre-existing NUCARS methods. CONTACT's wheel/rail geometrical contact module (Module 1) was preliminarily evaluated, but needs further study to explain the differences to NUCARS' own algorithms found in some configurations.

7.5 Integration of CONTACT in SIMULIA Simpack

The SIMULIA Simpack multi-body software was previously developed and distributed by SIMPACK AG, a small company based in Gilching, Germany. It was acquired by the multinational company Dassault Systèmes (3DS) in 2014 and the software was integrated into the SIMULIA brand and the 3DExperience Platform.

The history of VORtech with Simpack began in 2010, when the authors started developing the Kalker CONTACT add-on for Simpack Rail, providing a product with which users can inspect the detailed contact calculations *after* the dynamic simulation of a rail vehicle has completed

(Vollebregt, et al., 2011). This was used to study wear and rolling contact fatigue (among other issues) arising from track deviations (Vollebregt & Steenbergen, 2016). The current development considers an *online* integration of CONTACT and Simpack, in which the contact forces computed by CONTACT feed back into and directly affect the dynamic simulation (Vollebregt, 2019b). This is realized based on Simpack's facilities of user-routines, using standard force elements. Extensions that support integration of rail-wheel contacts as user routines are being developed at 3DS.

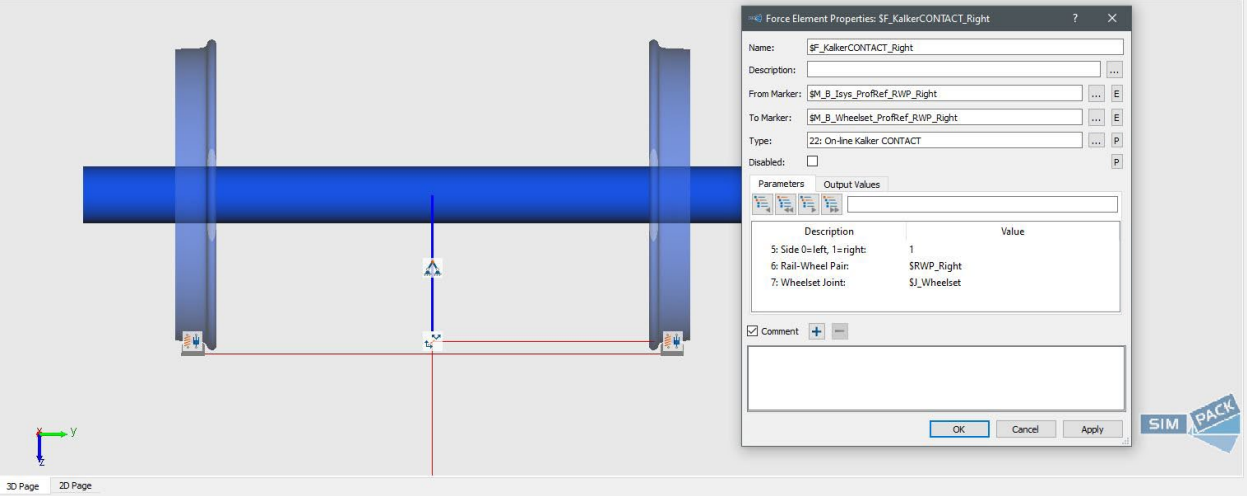

Figure 63. Dialog for configuration of the user subroutine for online use of the CONTACT library in SIMULIA Simpack

SIMULIA Simpack provides extensive capabilities for user routine programming to define, for instance, custom excitations, joints, constraints, force elements, roads, tires, result elements, as discussed in Section C.8 of the Simpack Help Assistant (v2020.1). These user routines are treated in the same way as the internal library elements. The main restrictions are that every type of user element is met with certain demands on its working, and on the internal data that may be queried.

A Simpack user routine `uforce22.f` requires that three subroutines be defined, which must be suitable for several different tasks, such as identifying the name of the element and the names and types of parameters, repeatedly computing the actual force values, and cleaning up after a simulation is done. From this, Simpack automatically creates a dialog that presents the routine to the user. Initially, this uses the basic inputs obtained from Simpack's rail-wheel pair, shown in Figure 63. Additional parameters may be added for information on the friction law and the behavior of interfacial layers. Output channels are defined in an equally flexible way and may then be inspected in the Simpack postprocessor.

The prototype was tested using a model of a wheelset that was gradually displaced to the right, as defined in the Manchester contact benchmark (Shackleton & Iwnicki, 2006; 2008). Three variants were defined for right and left wheels, without and with yaw angle. In each case, a simulation using the user routine was compared to the original results of Simpack, using the equivalent elastic method for the normal contact and FASTSIM as the tangential method (Vollebregt, 2019b).

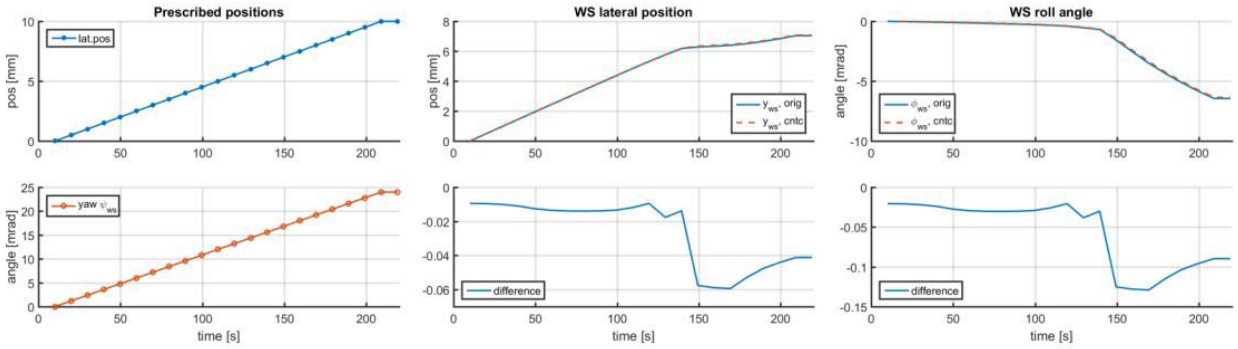

Figure 64. Comparison of Simpack runs for the right wheel with yaw, using Simpack's internal algorithms ("orig") and the CONTACT user routine ("cntc"), showing inputs and resulting positions (Vollebregt, 2019b)

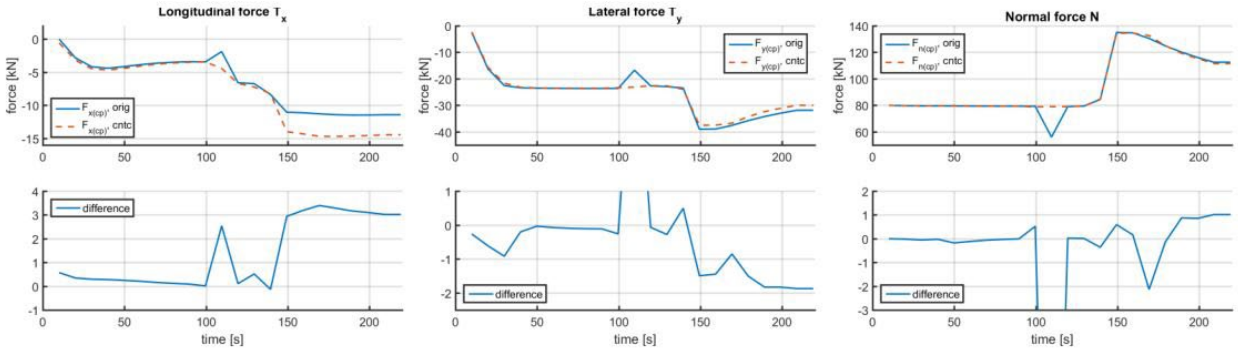

Figure 65. Comparison of Simpack runs for the right wheel with yaw, using Simpack's internal algorithms ("orig") and the CONTACT user routine ("cntc"), showing contact forces (Vollebregt, 2019b)

Figure 64 and Figure 65 give a sample of the results for the final test case: right wheel including yaw. These show that the prototype function is generally acceptable, but relevant differences are found at different positions.

- The differences at $t = 110$ s are due to detecting one contact patch in CONTACT, and two patches in Simpack.
- The differences in longitudinal force T_x are due mostly to the use of different coordinate conventions. Further study is needed to convert data to and from Simpack in an appropriate way.
- The differences in lateral force T_y may result from differences between CONTACT and FASTSIM, related to the larger contact angles and spin creepage towards the end of the simulation.

A further source of differences resides in the locations at which the contact forces are computed and how they are shifted. Initially, the contact forces delivered by CONTACT were put at the wheel profile marker with no compensation for the shift of location. The results improved considerably by using a quick ad-hoc approach, accounting for the moments involved. Further improvements are expected from refinement of this ad-hoc approach.

7.6 Conclusions Regarding Integration

This section described the CONTACT library version and its successful online integration in simulation packages for VTI, viz. Universal Mechanism, GENSYS, NUCARS, and SIMULIA Simpack. Integration works by developing a suitable wrapper routine in the VTI package for calling the library functions: loading the library, setting up control flags and model parameters, and at each integration step updating wheel/rail positions and computing the contact forces.

Two integration methods have been used by the different vendors, using CONTACT's basic interface for generic contacts (Module 3), or also using CONTACT’s wheel/rail geometry analysis (Module 1). The former is implemented more easily, using the package's own formats and coordinate conventions, while the latter offers more extended algorithms for geometric analysis and creep calculation.

Results obtained from evaluations with Universal Mechanism and GENSYS give good confidence in the functioning of CONTACT's wheel/rail processing algorithms. Results obtained with Simpack show how this depends on where forces are located and what coordinate systems are used. In such cases, additional testing is needed to identify the conditions where the results are significantly different and to distinguish mismatches in the interface from inherent and expected differences between the algorithms that are compared.

8. Conclusion

Measured wheel/rail contact forces deviate in several respects from existing theories on frictional contact mechanics. Creep force curves exhibit a lower initial slope than predicted by Kalker's original theories, a slower transition is found from the linear to saturated regimes, and there is a reduction of traction forces with increasing creepage, after attaining a maximum value. Further, dependencies are found on the rolling speed and maximum pressure. These effects are introduced in ad hoc ways in the main creep-force algorithms used in vehicle track interaction software by scaling the creepages (PERCENT_KALKER approach) or introducing fitting parameters (Polach's method, Modified FASTSIM, Extended CONTACT), to be adjusted to the circumstances of each specific case.

Many factors have been considered for explaining the deviations of measured values from theoretical modeling results: presence of sand, clay, iron oxides (wear debris), leaves, grease (solid interfacial layers), fluids like water or oil, surface films (i.e., BL), surface roughness, heat generation, and vibration of the contacting surfaces. Partial models have been formulated for the investigation of these effects, such as the influence of water on the level of adhesion, the influence of temperature and fluids on creep forces, or the influence of solid third body layers on creep forces. However, no integrated model exists that is based on elasticity theory, is generic in the range of situations considered, and can be integrated in VTI software.

This report explored the state of the art of modeling frictional phenomena in wheel-rail contacts and contributed to the modeling of interfacial layers and contact temperatures. These extensions are tied to the deviations of the creep force characteristic as follows:

- With respect to the initial slope, Extended CONTACT presented an explanation based on an elastic interfacial layer with a possible background in surface roughness. This explanation is questioned because unrealistically soft material or thick layers have to be assumed to get the measured slope reduction. Here, the authors presented a different view that fits with the measurements of Hou and colleagues' rheological model of solid layer in rolling contact (1997). In this view, the initial portion of measured curves originates mostly from rearranging and compacting the layer. This may be described by plastic deformation with a strong work-hardening characteristic, up to a level where this molding no longer works and is overtaken by a process with little or no work-hardening.
- Regarding the transition from linear to saturated regimes, the authors adopt the view of Meierhofer and colleagues (2014) that this may be explained by plastic deformation in the third body layer. A new formulation is presented for this, extending Kalker's theories with near-surface tangential plastic deformation, with work-hardening ($k_\tau > 0$), elastic-perfectly plastic ($k_\tau = 0$), or work-softening characteristics ($k_\tau < 0$). This sub-model reproduces the observed patterns in measured creep curves at small positive values for the work-hardening parameter k_τ. This physical phenomenon may also play a role in the dependence of creep forces on contact pressure and in the falling friction phenomenon when $k_\tau < 0$.
- In respect to the falling part of creep force curves, the authors implemented the temperature model presented by Ertz & Knothe (2002) in CONTACT and made the COF dependent on temperature cf. (Tomberger, et al., 2011). This achieves the desired reduction of creep forces if friction is halved over a temperature increase of about $400°C$.

In a broad range, this agrees with the reduction of elasticity parameters as measured by Jöller (1992), supporting the idea that temperature is a main cause of falling friction in dry contact situations.

Further work should be done on these aspects to generalize the sub-model for temperature to transient contacts and for the plasticity sub-model to non-linear work-hardening characteristics. Additional experiments should then be performed to validate the main tendencies predicted by these modeling aspects and to establish ranges for the sub-models' parameters. These experiments should be carefully designed with an eye on their subsequent numerical simulation to provide the information needed to run the model.

The authors explored the existing models for the roles of fluids in wheel-rail contacts and identified the desired aspects of a robust detailed modeling approach. They estimate that this includes the feedback between temperature and fluid viscosity, which is disregarded in the most advanced models currently used for wheel-rail contact forces. Future work is needed to develop a full model for situations with fluids, using an EHL approach considering this interaction. Additional insight is also desired on the rheology and composition of other fluids and mixtures than water that are found in wheel-rail contact situations.

9. References

Arias-Cuevas, O. (2010). *Low adhesion in the wheel-rail contact.* Doctoral dissertation, Delft University of Technology.

Ban, T. (2004). A study on the coefficient of friction between rail gauge corner and wheel flange focusing on wheel machining. *Proceedings of the International Wheelset Congress*.

Barus, C. (1893). Isothermals, isopiestics, and isometrics relative to viscosity. *American Journal of Science, 45*, 87–96.

Beagley, T. M. & Pritchard, C. (1975). Wheel/rail adhesion - the overriding influence of water. *Wear, 35*, 299–313.

Beagley, T. M., McEwen, I. J. & Pritchard, C. (1975a). Wheel/rail adhesion - boundary lubrication by oily fluids. *Wear, 31*, 77–88.

Beagley, T. M., McEwen, I. J. & Pritchard, C. (1975b). Wheel/rail adhesion - the influence of railhead debris. *Wear, 33*, 141–152.

Ben-Zion, Y. (1990). The response of two half spaces to point dislocations at the material interface. *Geophysical Journal International, 101*, 507–528.

Berthier, Y. (1990). Experimental evidence for friction and wear modeling. *Wear, 139*, 77–92.

Beyer, F., Hauer, F. & Willner, K. (2015). Development of a constitutive friction law based on the frictional interaction of rough surfaces. *Tribology in Industry, 37*, 400–412.

Bhushan, B. (2000). Tribology: Friction, Wear and Lubrication. In R. C. Dorf (Ed.), *The Engineering Handbook*. CRC Press.

Blok, H. (1937). Theoretical study of temperature rise at surfaces of actual contact under oiliness lubricating conditions. *General Discussion on Lubrication, 2*, 222–235. Institution of Mechanical Engineers.

Blok, H. (1963). The flash temperature concept. *Wear, 6*, 483–494.

Bowden, F. P. & Rowe, G. W. (1956). The adhesion of clean metals. *Proceedings of the Royal Society of London, Series A, 233*, 429–442.

Bowden, F. P. & Young, J. E. (1951). Friction of clean metals and the influence of adsorbed films. *Proceedings of the Royal Society of London, Series A, 208*, 311–325.

Brickle, B. V. (1973). *The steady state forces and moments on a railway wheelset including flange contact conditions.* Doctoral dissertation, Loughborough University of Technology.

Broster, M., Pritchard, C. & Smith, D. A. (1974). Wheel/rail adhesion: Its relation to rail contamination on British railways. *Wear, 29*, 309–321.

Bucher, F., Theiler, A. & Knothe, K. (2002). Normal and tangential contact problems of surfaces with measured roughness. *Wear, 253*, 204–218.

Cann, P. M. (2006). The “leaves on the line” problem: A study of film formation and lubricity under simulated railtrack conditions. *Tribology Letters, 24*, 151–158.

Carslaw, H. S. & Jaeger, J. C. (1959). *Conduction of heat in solids.* Oxford University Press.

Carter, F. W. (1926). On the action of a locomotive driving wheel. *Proceedings of the Royal Society of London, A112*, 151–157.

Chaikittiratana, A., Koetniyom, S. & Lakkam, S. (2012). Static/kinetic friction behaviour of a clutch facing material: Effects of temperature and pressure. *World Academy of Science, Engineering and Technology, 6*(6), 1048–1051.

Chang, C., Chen, B., Cai, Y. & Wang, J. (2018). An experimental study of high speed wheel-rail adhesion characteristics in wet condition on full scale roller rig. In Z. L. Nunez (Ed.), *Proceedings of the 11th International Conference on Contact Mechanics and Wear of Rail/Wheel Systems* (pp. 115–122). Delft University of Technology.

Chen, H., Ban, T., Ishida, M. & Nakahara, T. (2002). Adhesion between rail/wheel under water lubricated contact. *Wear, 253*, 75–81.

Chen, H., Ban, T., Ishida, M. & Nakahara, T. (2008). Experimental investigation of influential factors on adhesion between wheel and rail under wet conditions. *Wear, 265*, 1504–1511.

Chen, H., Ishida, M. & Nakahara, T. (2005). Analysis of adhesion under wet conditions for three-dimensional contact considering surface roughness. *Wear, 258*, 1209–1216.

Chen, H., Ishida, M., Namura, A., Baek, K. S., Nakahara, T., Leban, B. & Pau, M. (2011). Estimation of wheel/rail adhesion coefficient under wet conditions with measured boundary friction coefficient and real contact area. *Wear, 271*, 32–39.

Chen, H., Namura, A., Ishida, M. & Nakahara, T. (2016). Influence of axle load on wheel/rail adhesion under wet conditions in consideration of running speed and surface roughness. *Wear, 366-367*, 303–309.

Chen, H., Yohsimura, A. & Ohyama, T. (1998). Numerical analysis for the influence of water film on adhesion between rail and wheel. *Proceedings of the Institution of Mechanical Engineers, Part J: Journal of Engineering Tribology, 212*, 359–368.

Chiu, Y. P. (1978). On the stress field and surface deformation in a half space with a cuboidal zone in which initial strains are uniform. *Journal of Applied Mechanics, 45*, 302–306.

Ciavarella, M., Greenwood, J. A. & Paggi, M. (2008). Inclusion of "interaction" in the Greenwood and Williamson contact theory. *Wear, 265*, 729–734.

Clayton, P. (1996). Tribological aspects of wheel-rail contact: A review of recent experimental research. *Wear, 191*, 170–183.

Descartes, S., Desrayaud, C., Niccolini, E. & Berthier, Y. (2005). Presence and role of the third body in a wheel-rail contact. *Wear, 258*, 1081–1090.

Dowson, D. (1998). *History of Tribology, 2nd Edition.* Professional Engineering Publishing.

Dowson, D. & Higginson, G. R. (1966). *Elasto-hydrodynamic lubrication: The fundamentals of roller and gear lubrication.* Pergamon Press.

Ertz, M. & Knothe, K. (2002). A comparison of analytical and numerical methods for the calculation of temperatures in wheel/rail contact. *Wear, 253*, 498–508.

Eyring, H. (1938). Viscosity, plasticity, and diffusion as examples of absolute reaction rates. The *Journal of Chemical Physics, 4*, 283–291.

Fischer, F. D., Daves, W. & Werner, E. A. (2003). On the temperature in the wheel-rail rolling contact. *Fatigue and Fracture of Engineering Materials and Structures, 26*, 999–1006.

Fries, R., Urban, C., Wilson, N. & Witte, M. (2011). Modeling of friction modifier and lubricant characteristics for rail vehicle simulations. *Proceedings of the 22nd International Symposium on Dynamics of Vehicles on Roads and Tracks*.

Fromm, H. (1927). Berechnung des Schlupfes beim Rollen deformierbarer Scheiben. *Zeitschrift für angewandte Mathematik und Mechanik, 7*, 27–58.

Fulford, C. R. (2004). *Review of Low Adhesion Research*. Technical Report CRF04002 (Reference T354). Rail Safety and Standards Board, United Kingdom.

Giménez, J. G., Alonso, A. & Gómez, E. (2005). Introduction of a friction coefficient dependent on the slip in the FASTSIM algorithm. *Vehicle System Dynamics, 43*, 233–244.

Godet, M. (1984). Third body approach: A mechanical view of wear. *Wear, 149*, 325–340.

Godet, M., Play, D. & Berthe, D. (1984). An attempt to provide a uniform theory of tribology through load-carrying capacity, transport and continuum mechanics. *Journal of Lubrication Technology, 102*, 153–164.

Greenwood, J. A. & Williamson, J. B. (1966). Contact of nominally flat surfaces. *Proceedings of the Royal Society of London, A295*, 300–319.

Grubin, A. N. (1949). *Fundamentals of the Hydrodynamic Theory of Lubrication of Heavily Loaded Cylindrical Surfaces.* Central Scientific Research Institute for Technology and Mechanical Engineering, Moscow.

Haines, D. J. (1964). Contact stresses in flat elliptical contact surfaces which support radial and shearing forces during rolling. *Proceedings of the Institution of Mechanical Engineers, 179*, 154–168.

Haines, D. J. & Ollerton, E. (1963). Contact stress distributions on elliptical contact surfaces subjected to radial and tangential forces. *Proceedings of the Institution of Mechanical Engineers, 177*, 95–114.

Halling, J. & Al-Qishtaini, M. A. (1967). An experimental study of some of the factors affecting the contact conditions and the slip between a rolling ball and its track. *Proceedings of the Institution of Mechanical Engineers, 182*, 757–768.

Halling, J. & Brothers, B. G. (1966). The effect of surface finish on the creep and wear of a rolling ball subjected to normal and tangential surface tractions. *Wear, 9*, 199–208.

Hamrock, B. J., Schmid, S. R. & Jacobson, B. O. (2004). *Fundamentals of Fluid Film Lubrication, 2nd Edition.* CRC Press.

Hauer, F. (2014). *Die elasto-plastische Einglättung rauer Oberflächen und ihr Einfluss auf die Reibung in der Umformtechnik.* Doctoral dissertation, Friedrich Alexander Universität Erlangen-Nürnberg.

Hobbs, A. E. (1967). *A survey of creep.* Technical report. British Rail Department, DYN 52.

Hou, K., Kalousek, J. & Magel, E. (1997). Rheological model of solid layer in rolling contact. *Wear, 211*, 134–140.

Hou, K., Kalousek, J., Lamba, H. & Scott, R. (2000). Thermal effect on adhesion in wheel/rail contact. *Proceedings of the 5th International Conference on Contact Mechanics and Wear of Rail/Wheel Systems*, pp. 239–244.

Illingworth, R. (1973). *The mechanism of railway vehicle excitation by track irregularities.* Doctoral dissertation, University of Oxford.

Jaeger, J. C. (1942). Moving sources of heat and the temperature at sliding contacts. *Proceedings of the Royal Society of New South Wales*, *76*, 203–224.

Johnson, K. L. (1958a). The effect of spin upon the rolling motion of an elastic sphere upon a plane. *Journal of Applied Mechanics, 25*, 332–338.

Johnson, K. L. (1958b). The effect of a tangential contact force upon the rolling motion of an elastic sphere upon a plane. *Journal of Applied Mechanics, 25*, 339–346.

Johnson, K. L. (1985). *Contact Mechanics.* Cambridge University Press.

Johnson, K. L. & Tevaarwerk, J. L. (1977). Shear behaviour of elasohydrodynamic oil films. *Proceedings of the Royal Society London A: Mathematical, Physical and Engineering Sciences, 356*, 215–236.

Johnson, K. L., Greenwood, J. A. & Poon, S. Y. (1972). A simple theory of asperity contact in elastohydrodynamic lubrication. *Wear, 19*, 91–108.

Jöller. (1992). *Temperatureinfluss auf die mechanischen Eigenschaften von Schienenwerkstoffen.* Internal Report TF-9/92, voestalpine Stahl Donawitz GmbH.

Kalker, J. J. (1967). *On the rolling contact of two elastic bodies in the presence of dry friction.* Doctoral dissertation, Delft University of Technology.

Kalker, J. J. (1973). Simplified theory of rolling contact. *Delft Progress Report Series C1, 1*, 1–10.

Kalker, J. J. (1978). Über die Mechanik des Kontaktes zwischen Rad und Schiene. *ZEV-Glas. Ann., 102*, 214–218.

Kalker, J. J. (1979). The computation of three-dimensional rolling contact with dry friction. *International Journal for Numerical Methods in Engineering, 14*, 1293–1307.

Kalker, J. J. (1982). A fast algorithm for the simplified theory of rolling contact. *Vehicle System Dynamics, 11*, 1–13.

Kalker, J. J. (1990). *Three-dimensional elastic bodies in rolling contact.* Kluwer Academic Publishers.

Kalker, J. J. (1992). Modification of the two-body contact conditions to account for the third body. In D. Dowson, C. Taylor, T. Childs, M. Godet & G. Dalmaz (Eds.), *Wear Particles: From the Cradle to the Grave; Proceedings of the 18th Leeds-Lyon Symposium on Tribology*, pp. 183–189.

Kalker, J. J. (1996). Book of tables for the Hertzian creep-force law. In I. Zobory (Ed.), *Proceedings of the 2nd Mini Conference on Contact mechanics and Wear of Wheel/Rail systems* (pp. 11–20). Technical University of Budapest.

Kalker, J. J., Dekking, F. M. & Vollebregt, E. A. H. (1997). Simulation of rough, elastic contacts. *Journal of Applied Mechanics, 64*, 361–368.

Kalousek, J., Hou, K., Magel, E. & Chiddick, K. (1996). The benefits of friction management - a third body approach. *Proceedings of the World Congress on Rail Research Conference 1996*, pp. 461–468.

Kapoor, A., Franklin, F. J., Wong, S. K., & Ishida, M. (2002). Surface roughess and plastic flow in rail wheel contact. *Wear, 253*, 257–268.

Knothe, K. (2008). History of wheel/rail contact mechanics: From Redtenbacher to Kalker. *Vehicle System Dynamics, 46*, 9–26.

Knothe, K. & Liebelt, S. (1995). Determination of temperatures for sliding contact with applications for wheel-rail systems. *Wear, 189*, 91–99.

Knothe, K. & Theiler, A. (1996). Normal and tangential contact problem with rough surfaces. In I. Zobory (Ed.), *Proceedings of the 2nd mini conference on contact mechanics and wear of wheel/rail system,* pp. 34–43. Technical University of Budapest, Hungary.

Leroux, J., Fulleringer, B. & Nélias, D. (2010). Contact analysis in presence of spherical inhomogeneities within a half-space. *International Journal of Solids and Structures, 47*, 3034–3049.

Lim, S. C. & Ashby, M. F. (1987). Overview no. 55, wear-mechanism maps. *Acta Metallurgica, 35*, 1–24.

Lim, S. C., Ashby, M. F. & Brunton, J. H. (1989). The effects of sliding conditions on the dry friction of metals. *Acta Metallurgica, 37*, 767–772.

Logston, C. F. & Itami, G. S. (1980). Locomotive friction-creep studies. *ASME Journal of Engineering for Industry, 102*, 275–281.

Magel, E. E. (2017, 9). *A survey of wheel/rail friction.* Technical report DOT/FRA/ORD-17/21, Federal Railroad Administration.

Majumdar, A. & Bhushan, B. (1991). Fractal model of elastic-plastic contact between rough surfaces. *American Society of Mechanical Engineers Journal of Tribology, 113*, 1–11.

McEwen, I. J. (1999). *Rail contamination and its influence on wheel/rail adhesion.* Technical memo TM-MSU-408, British Rail Scientifics.

Meierhofer, A. (2015). *A new wheel-rail creep force model based on elasto-plastic third body layers.* Doctoral dissertation, Graz University of Technology.

Meierhofer, A., Hardwick, C., Lewis, R., Six, K. & Dietmaier, P. (2014). Third body layer—experimental results and a model describing its influence on the traction coefficient. *Wear, 314*, 148–154.

Meymand, S., Keylin, A. & Ahmadian, M. (2016). A survey of wheel-rail contact models for rail vehicles. *Vehicle System Dynamics, 58*(3), 368–428.

Molinari, A., Estrin, Y. & Mercier, S. (1999). Dependence of the coefficient of friction on sliding conditions in the high velocity range. *Journal of Tribology, 121*, 35–41.

Monk-Steel, A. D., Thompson, D. J., Beer, F. G. & Janssens, M. H. (2006). An investigation into the influence of longitudinal creepage on railway squeal noise due to lateral creepage. *Journal of Sound and Vibration, 293*, 766–776.

Mosaddegh, P., Ziegert, J., Iqbal, W. & Tohme, Y. (2011). Apparatus for high temperature friction measurement. *Precision Engineering, 35*, 473–783.

Müser, M. H., Dapp, W. B., Bugnicourt, R., Sainsot, P., Lesaffre, N., Lubrecht, T. A., Persson, B., Harris, K. L., Bennett, A., Schulze, K., Rodhe, S., Ifju, P., Sawyer, W., Angelini, T., Hossein Ashtari, E., Kadkhodaei, S., Jiunn-Jong, W., Vorlafer, G., Vernes, A., . . . Greenwood, J. A. (2017). Meeting the contact-mechanics challenge. *Tribology Letters, 65*, 118.

Nayak, P. R., Hariharan, S., Stern, R., Abilock, R., March, P. A. & Gupta, P. K. (1970). *Friction and creep in rolling contact.* Technical report FRA-RT-71-64, Federal Railroad Administration.

Neubert, S., Porat, A., Hentschke, C. & Jacobs, G. (2013). Mixed friction model for rough contacts at high pressure. *Proceedings of the Institution of Mechanical Engineers, Part J: Journal of Engineering Tribology, 227*, 496–509.

Niccolini, E. & Berthier, Y. (2005). Wheel-rail adhesion: Laboratory study of "natural" third body role on locomotive wheels and rails. *Wear, 258*, 1172–1178.

Ohyama, T. (1991). Tribological studies on adhesion phenomena between wheel and rail at high speeds. *Wear, 144*, 263–275.

Oldknow, K., Eadie, D. T. & Stock, R. (2013). The influence of precipitation and friction control agents on forces at the wheel/rail interface in heavy haul railways. *Proceedings of the Institution of Mechanical Engineers, Part F: Journal of Rail and Rapid Transit, 227*, 86–93.

Olofsson, U. & Lewis, R. (2006). Tribology of the wheel-rail contact. In S. Iwnicki, *Handbook of Railway Vehicle Dynamics* (pp. 121–142). CRC Press.

Patir, N. & Cheng, H. S. (1978). An average flow model for determining effects of three-dimensional roughness on partial hydrodynamic lubrication. *Journal of Lubrication Technology, 100*, 12–17.

Pearson, S. R., Shipway, P. H., Abere, J. O. & Hewitt, R. A. (2013). The effect of temperature on wear and friction of a high strength steel in fretting. *Wear, 303*, 622–631.

Périard, F. J. (1998). *Wheel-rail noise generation: Curve squealing by trams.* Doctoral dissertation, Delft University of Technology.

Persson, B. N. (2001). Theory of rubber friction and contact mechanics. *Journal of Chemical Physics, 115*, 3840–3861.

Persson, B. N. & Scaraggi, M. (2014). Theory of adhesion: Role of surface roughness. *Journal of Chemical Physics, 141*, 124–701.

Persson, I. (2019). *Test and compare results obtained with CONTACT v18.1.* Technical report R1812.1, DEsolver, Sweden.

Petrov, N. P. (1883). Friction in Machines and the Effect of the Lubricant. *Inzhenerno Zhurnal St. Petersburg, 1*, 71–140.

Piotrowski, J. (2010). Kalker's algorithm Fastsim solves tangential contact problems with slip-dependent friction and friction anisotropy. *Vehicle System Dynamics, 48*, 869–889.

Piotrowski, J. & Kik, W. (2008). A simplified model of wheel/rail contact mechanics for non-Hertzian problems and its application in rail vehicle dynamics simulations. *Vehicle System Dynamics, 46*, 27–48.

Polach, O. (2005). Creep forces in simulations of traction vehicles running on adhesion limit. *Wear, 258*, 992–1000.

Polach, O., Berg, M. & Iwnicki, S. D. (2006). Chapter 12: Simulation. In S. Iwnicki, *Handbook of Railway Vehicle Dynamics,* pp. 359–421. CRC Press.

Popov, V. L. (2010). *Contact mechanics and friction: Physical principles and applications.* Springer-Verlag.

Poritsky, H. (1950). Stresses and deflections of cylindrical bodies in contact with application to contact of gears and of locomotive wheels. *Journal of Applied Mechanics, 17*, 191–201.

Pullen, J. & Williamson, J. B. (1972). On the plastic contact of rough surfaces. *Proceedings of the Royal Society London A: Mathematical, Physical and Engineering Sciences, 327*, 159–173.

Putelat, T., Dawes, J. H. & Willis, J. R. (2011). On the microphysical foundations of rate-and-state friction laws. *Journal of the Mechanics and Physics of Solids, 59*, 1062–1075.

Rabinowicz, E. (1995). *Friction and wear of materials, 2nd ed.* John Wiley and Sons.

Rabinowicz, E., & Imai, M. (1963). *Friction and wear at elevated temperatures.* Tech. rep. WADC-TR-59-603, Surface Laboratory, Massachusetts Institute of Technology.

Ren, N. & Lee, S. C. (1994). The effects of surface roughness and topography on the contact behavior of elastic bodies. *Journal of Tribology 116*, 12–17.

Reynolds, O. (1876). On rolling friction. *Philosophical Transactions of the Royal Society of London, 166*, 155–174.

Reynolds, O. (1886). On the theory of lubrication and its application to Mr. Beauchamp Tower's experiments. *Philosophical Transactions of the Royal Society of London, 177*, 157–234.

Rice, J. R. (2006). Heating and weakening of faults during earthquake slip. *Journal of Geophysical Research, 111*, B05311.

Rodikov, A. & Vollebregt, E. (2018). *Integration and testing of the CONTACT library in UM.* Technical report FRA-TR-006, Computational Mechanics, Ltd.

Roelands, C. J. (1966). *Correlation aspects of the viscosity - temperature - pressure relationship of lubricated oils.* Doctoral dissertation, Delft University of Technology.

RSSB. (2014). *T0142: Investigation into the effect of moisture on rail adhesion.* Technical report, Rail Safety and Standards Board, United Kingdom.

Sawley, K. J. (2007). Calculation of temperatures in a sliding wheel/rail system and implications for wheel steel development. *Proceedings of the Institution of Mechanical Engineers, Part F: Journal of Rail and Rapid Transit, 221*, 455–464.

Sebès, M., Chevalier, L., Ayasse, J. B. & Chollet, H. (2012). A fast simplified wheel-rail contact model consistent with perfectly plastic materials. *Vehicle System Dynamics, 50*, 1453–1471.

Shackleton, P. & Iwnicki, S. D. (2006). *Wheel-rail contact benchmark, version 3.0.* Rail Technology Unit, Manchester Metropolitan University.

Shackleton, P. & Iwnicki, S. D. (2008). Comparison of wheel-rail contact codes for railway vehicle simulation: an introduction to the Manchester Contact Benchmark and initial results. *Vehicle System Dynamics, 46*, 129–149.

Shu, X. (2018, 7). *CONTACT Library Integration into NUCARS.* Technical report, TTCI, Pueblo.

Singh, A. K. & Singh, T. N. (2016). Stability of the rate, state and temperature dependent friction model and its applications. *Geophysical Journal International, 205*, 636–647.

Six, K., Meierhofer, A., Müller, G. & Dietmaier, P. (2015). Physical processes in wheel-rail contact and its implications on vehicle-track interaction. *Vehicle System Dynamics, 53*, 635–650.

Six, K., Meierhofer, A., Trummer, G., Bernsteiner, C., Marte, C., Müller, G., Luber, B., Dietmaier, P. & Rosenberger, M. (2016a). Plasticity in wheel-rail contact and its implications on vehicle-track interaction. *Proceedings of the Institution of Mechanical Engineers, Part F: Journal of Rail and Rapid Transit, 231*, 558–569.

Six, K., Meierhofer, A., Trummer, G., Marte, C., Müller, G., Luber, B., Dietmaier, P. & Rosenberger, M. (2016b). Classification and consideration of plasticity phenomena in wheel-rail contact modeling. *International Journal of Railway Technology, 5*, 55–77.

Six, K., Trummer, G., Buckley-Johnstone, L. & Lewis, R. (2017). Impact of low amounts of water in combination with wear debris/iron oxides on wheel-rail adhesion. In M. S. McSweeney (Ed.), *Proceedings of the 25th International Symposium on Dynamics of Vehicles on Roads and Tracks*, pp. 557–562. International Association for Vehicle System Dynamics.

Spiryagin, M., Lee, K., Yoo, H., Kashura, O. & Popov, S. (2010). Numerical calculation of temperature in the wheel-rail flange contact and implications for lubricant choice. *Wear*, 287–293.

Spiryagin, M., Persson, I., Vollebregt, E. & Cole, C. (2017). Comparison of simplified and complete contact modelling approaches in simulations of high adhesion locomotives. In M. S. McSweeney (Ed.), *Proceedings of the 25th International Symposium on Dynamics of Vehicles on Roads and Tracks*, pp. 613–620. International Association for Vehicle System Dynamics.

Spiryagin, M., Polach, O. & Cole, C. (2013). Creep force modelling for rail traction vehicles based on the Fastsim algorithm. *Vehicle System Dynamics, 51*, 1765–1783.

Stott, F. H. (2002). High-temperature sliding wear of metals. *Tribology International, 35*, 489–495.

Stribeck, R. (1902). Die wesentlichen Eigenschaften der Gleit- und Rollenlager. *VDI-Zeitschrift, 46*, 1341–1348, 1432–1438, 1463–1470.

Tomberger, C. (2009). *Der Rad-Schiene Kraftschluss unter Berücksichtigung von Temperatur, fluiden Zwischenschichten und mikroskopischer Oberflächenrauheit.* Doctoral dissertation, Technischen Universität Graz.

Tomberger, C., Dietmaier, P., Sextro, W. & Six, K. (2011). Friction in wheel-rail contact: A model comprising interfacial fluids, surface roughness and temperature. *Wear, 271*, 2–12.

Tower, B. (1883). First report on friction experiments. *Proceedings of the Institution of Mechanical Engineers, 34*(1), 632–659.

Trummer, G., Buckley-Johnstone, L. E., Voltr, P., Meierhofer, A., Lewis, R. & Six, K. (2017). Wheel-rail creep force model for predicting water induced low adhesion phenomena. *Tribology International, 109*, 409–415.

Vakis, A. I., Yastrebov, V. A., Scheibert, J., Nicola, L., Dini, D., Minfray, C., Almgvist, A., Paggi, M., Lee, S., Limbert, G., Molinari, J. F., Anciaux, G., Aghababaei, R., Echeverri Restrepo, S., Papangelo, A., Cammarata, A., Nicolini, P., Putignano, C., Carbone, G., . . . Ciavarella, M. (2018). Modeling and simulation in tribology across scales: An overview. *Tribology International, 125*, 169–199.

Velkavrh, I., Ausserer, F., Klien, S., Voyer, J., Ristow, A., Brenner, J., Forêt, P. & Diem, A. (2016). The influence of temperature on friction and wear of unlubricated steel/steel contacts in different gaseous atmospheres. *Tribology International, 98*, 155–171.

Venner, C. H. & Bos, J. (1994). Effects of lubricant compressibility on the film thickness in EHL line and circular contacts. *Wear* (173), 151–165.

Venner, C. H. & Lubrecht, A. A. (2000). *Multilevel methods in lubrication.* Tribology Series n37. Elsevier.

Vollebregt, E. A. H. (1995). A Gauss-Seidel type solver for special convex programs, with application to frictional contact mechanics. *Journal of Optimization Theory and Applications*, 47–67.

Vollebregt, E. A. H. (2009). Refinement of Kalker's rolling contact model. In A. Bracciali (Ed.), *Proceedings of the 8th International Conference on Contact Mechanics and Wear of Rail/Wheel Systems*, pp. 149–156.

Vollebregt, E. A. H. (2010). Improving the speed and accuracy of the frictional rolling contact model "CONTACT". In B. T. Romero (Ed.), *Proceedings of the 10th International Conference on Computational Structures Technology.* Civil-Comp Press.

Vollebregt, E. A. H. (2014). Numerical modeling of measured railway creep versus creep-force curves with CONTACT. *Wear, 314*, 87–95.

Vollebregt, E. A. H. (2015). FASTSIM with falling friction and friction memory. In Nielsen, J. C. O., Anderson, D., Gautier, P. E., Iida, M., Nelson, J. T., Thompson, D., Tielkes, T., Towers, D. A. & P. Vos (Eds.), *Noise and Vibration Mitigation for Rail Transportation*

Systems; Proceedings of the 11th International Workshop on Railway Noise, 126, pp. 425–432. Springer.

Vollebregt, E. A. H. (2016). *Project proposal for BAA-2016: FRA-TR-006; Advanced modelling of wheel-rail friction phenomena.* EV/M16.030. VORtech.

Vollebregt, E. A. H. (2019a). *User guide for CONTACT, Rolling and sliding contact with friction.* Technical report TR09-03 (v19.1). VORtech.

Vollebregt, E. A. H. (2019b). *Report on the integration of CONTACT in SIMULIA Simpack.* EV/M19.032. VORtech.

Vollebregt, E. A. H. (2022). Detailed wheel/rail geometry processing using the planar contact approach. *Vehicle System Dynamics, 60*(4), 1253–1291.

Vollebregt, E. A. H. & Schuttelaars, H. M. (2012). Quasi-static analysis of 2-dimensional rolling contact with slip-velocity dependent friction. *Journal of Sound and Vibration, 331*, 2141–2155.

Vollebregt, E. A. H. & Steenbergen, M. J. (2016). A methodology for assessing track irregularities with respect to rail damage. *International Journal of Railway Technology, 4*, 85–105.

Vollebregt, E. A. H., Weidemann, C. & Kienberger, A. (2011). Use of "CONTACT" in multi-body vehicle dynamics and profile wear simulation: Initial results. In S. Iwnicki (Ed.), *Proceedings of the 22nd International Symposium on Dynamics of Vehicles on Roads and Tracks.* International Association for Vehicle System Dynamics.

Voltr, P. & and Lata, M. (2015). Transient wheel-rail adhesion characteristics under the cleaning effect of sliding. *Vehicle System Dynamics, 53*, 605–618.

Wang, W. J., Shen, P., Song, J. H., Guo, J., Liu, Q. Y. & Jin, X. S. (2011a). Experimental study on adhesion behavior of wheel/rail under dry and water conditions. *Wear, 271*, 2699–2705.

Wang, W. J., Zhang, H. F., H.Y.Wang, Liu, Q. Y. & Zhu, M. H. (2011b). Study on the adhesion behavior of wheel/rail under oil, water and sanding conditions. *Wear, 271*, 2693–2698.

Way, S. (1935). Pitting due to rolling contact. *Journal of Applied Mechanics, 57*, A49–A58.

Willner, K. & Hauer, F. (2012). Plastic deformation of rough surfaces. *Proceedings in Applied Mathematics and Mechanics, 12*, 207–208.

Wu, B., Wen, Z., Wang, H. & Jin, X. S. (2013). Analysis of wheel/rail adhesion under oil contamination with surface roughness. *Proceedings of the Institution of Mechanical Engineers, Part J: Journal of Engineering Tribology, 227*, 1306–1315.

Wu, B., Wen, Z., Wang, H. & Jin, X. S. (2014). Numerical analysis on wheel/rail adhesion under mixed contamination of oil and water with surface roughness. *Wear, 314*, 140–147.

Wu, B., Wen, Z., Wu, T. & Jin, X. S. (2016). Analysis on thermal effect on high-speed wheel/rail adhesion under interfacial contamination using a three-dimensional model with surface roughness. *Wear, 366–367*, 95–104.

Wu, H. & Wilson, N. (2006). Railway vehicle derailment and prevention. In S. Iwnicki, *Handbook of Railway Vehicle Dynamics,* pp. 209–237. CRC Press.

Yang, P. & Wen, S. (1990). A generalized Reynolds equation for non-Newtonian thermal elastohydrodynamic lubrication. *Journal of Tribology, 112*, 631–637.

Zakharov, S. M., Harris, W. J., Lundgren, J., Tournay, H. & Ebersöhn, W. (2001). *Guidelines to best practices for heavy haul railway operations: Wheel and rail interface issues.* International Heavy Haul Association.

Zhao, Y., Maietta, D. M. & Chang, L. (2000). An asperity microcontact model incorporating the transition from elastic deformation to fully plastic flow. *Journal of Tribology, 122*, 86–93.

Zhou, K., Chen, W. W., Keer, L. M., Ai, X., Sawamiphakdi, K., Glaws, P. & Wang, Q. J. (2011). Multiple 3D inhomogeneous inclusions in a half space under contact loading. *Mechanics of Materials, 43*, 444–457.

Zhu, Y. (2011). *Adhesion in the wheel/rail contact under contaminate conditions.* Licentiate thesis, Royal Institute of Technology.

Zhu, Y., Olofsson, U. & Söderberg, A. (2013). Adhesion modeling in the wheel-rail contact under dry and lubricated conditions using measured 3D surfaces. *Tribology International, 61*, 1–10.

Abbreviations and Acronyms

ACRONYMS	EXPLANATION
AoA	Angle of attack
BL	Boundary lubrication
COF	Coefficient of friction
EHL	Elasto-hydrodynamic lubrication
GW	Greenwood-Williamson
HD	Hydrodynamic lubrication
L/V	Lateral/vertical
NRC	National Research Council (Canada)
RCF	Rolling Contact Fatigue
VTI	Vehicle-track interaction (simulation software)
WBB	Wheel, Bearing, and Brake Test Facility (NRC Canada)